Spring 5-16-2020

Control and Locomotion of Inertially and Magnetically Actuated Multi-Scale Robotic Systems

Ehab Al Khatib
ealkhatib@smu.edu

CONTROL AND LOCOMOTION OF INERTIALLY AND MAGNETICALLY ACTUATED MULTI-SCALE ROBOTIC SYSTEMS

Approved by:

Dr. Yildirim Hurmuzlu
Professor

Dr. MinJun Kim
Professor

Dr. Edmond Richer
Associate Professor

Dr. Ali Beskok
Professor

Dr. Joe Zoghzoghy
Industry

CONTROL AND LOCOMOTION OF INERTIALLY AND MAGNETICALLY ACTUATED MULTI-SCALE ROBOTIC SYSTEMS

A Dissertation Presented to the Graduate Faculty of the

Lyle School of Engineering

Southern Methodist University

in

Partial Fulfillment of the Requirements

for the degree of

Doctor of Philosophy

with a

Major in Mechanical Engineering

by

Ehab Al Khatib

B.S., Mechanical Engineering, Jordan University of Science and Technology, Jordan
M.S., Mechatronics Engineering, American University of Sharjah, UAE

May 16, 2020

ACKNOWLEDGMENTS

I would like to express my deepest respect, gratitude, and appreciation to my academic advisor Dr. Yildirim Hurmuzlu. I am very grateful for your encouragement, guidance, and motivation. You've been a mentor, an academic advisor, and a father. With your help, you've made this work possible. Thank you for making me a better person, student, and researcher.

I would especially like to thank Dr. MinJun Kim for his contribution, and for granting me access to his biological, actuation, sensing, and transport laboratory (BAST Lab), where the experiments for the magnetically actuated robots were conducted.

I would also like to thank my professors on my supervisory committee, Dr. Edmond Richer, Dr. Ali Beskok, and Dr. Joe Zoghzoghy, for their valuable advice and comments, which have significantly helped me to improve my work.

This material is partially supported by the National Science Foundation under Grant (CMMI 1623324), for which I am grateful. Also, I appreciate the financial support I received from the Department of Mechanical Engineering at Southern Methodist University (SMU). I would like to express the greatest respect, love, appreciation, and gratitude to my mother and father, Zakieh and Ismail Al Khatib. Thank you for dedicating your lives for your family, and thank you for making me who I am today. Words can't express my gratitude for everything you've done. I hope I made you proud of me. I want to thank my sister Alaa, and my brothers Mahdy, Mohammed, Majdy, Mohannad, and Ahmad, for their unconditional love and support. I want to thank my soulmate Farah for her continuous support, care, and love throughout my graduate school career.

Finally, I would like to express my appreciation and love for all of my friends, who supported me throughout my journey. I want to thank my friends and labmates: Dr. Khalid Alluhydan, Pouria Razzaghi, Moahd Alghuson, Ahmad Gad, Assaad El Helou, Youssef Jaber, Abdullah Jabr, Ehab Sabi, Elie Salameh, Shide Bakhtiari, and Adam Cox.

Al Khatib, Ehab B.S., Mechanical Engineering, Jordan University of Science and Technology, Jordan
M.S., Mechatronics Engineering, American University of Sharjah, UAE

Control and Locomotion of Inertially and Magnetically Actuated Multi-Scale Robotic Systems

Advisor: Dr. Yildirim Hurmuzlu
Doctor of Philosophy degree conferred May 16, 2020
Dissertation completed April 28, 2020

In this research, two actuation systems were introduced, inertial and magnetic actuation. In the inertial actuation, the robot used the transfer of momentum to navigate, and this momentum could be generated by spinning masses and wheels. Recent studies in our System Laboratory proved that a wide range of inertially actuated locomotion systems could be generated. This can be achieved by using a family tree approach, starting from a very simple system, and progressively evolving it to more complex ones. The motion diversity of these robots inspired us to extend their locomotion from a macro scale to millimeter and micro scales. This dissertation was devoted to studying the control and locomotion of inertially and magnetically actuated multi-scale robotic systems. Three different robotic scales were presented: macro robot, millirobot, and microrobot. The work was significant because it showed that the agility and maneuverability of motion modes generated by inertial actuation could also be generated by magnetic actuation for smaller-scale robotic systems.

We first introduced the wheeled baton robot, which is an inertially-actuated car-like robot. The main advantage of this robot was that it could function in a simple wheeled vehicle mode as well as many other dynamic modes. Inertial actuation enabled the robot to perform high mobility maneuvers and in-air acrobatics. A mathematical model was developed, and different modes of motion of the system were identified, and the equations of motion were derived. Then, a modal transition flow diagram was presented based on the actuation torques. We designed a nonlinear tracking controller to regulate the control variables to implement the described modes of motion. Finally, we designed and built an

experimental prototype to verify the existence of the locomotion modes. We demonstrated experimentally that a simple car-like robot could generate several locomotion modes.

An external magnetic field can be used in remotely controlling magnetic millirobots and microrobots, making them promising candidates for biomedical and engineering applications, including cell manipulation and therapy. This work presented a low-cost millirobot that was simple in design, easy to fabricate, highly scalable, and can be used as modular sub-units within complex structures for large-scale manipulation. Individual millirobots were highly agile and capable of performing a variety of locomotive tasks such as pivot walking, tapping, and tumbling. A comparative study was presented to demonstrate the advantages and disadvantages of each locomotion mode. Our experimental data showed that the pivot walking was the fastest and the most stable of the motion modes examined. Further, we focused on the pivot walking mode, and a mathematical model of the system was developed, and the kinematic model was derived. We proposed two controllers to regulate the gait of the pivot walker. The first one was a proportional-geometric controller. The second controller was based on a gradient descent optimization technique. These control algorithms enabled the robot to generate stable gait while tracking a desired trajectory. Using simulations, the robustness of proposed controllers was established for different sweep angles. The two controllers exhibited excellent performance. Finally, to extend the functionality of our millirobots, we presented two systems utilizing multiple millirobots combined: a stag beetle and a carbot. Using a powerful electromagnetic coil system, we conducted extensive experiments to establish feasibility and practical utility of the magnetically actuated millirobot.

Following the successful magnetically actuated millirobot, we extended this research to a micro-scale. We presented a teleoperation scheme to control magnetically actuated microrobots. The system was developed to allow human operators to control the motion for magnetically actuated microrobots and feel their interactions with the environment. A haptic interface constituted the core of the teleoperation system. It was used to provide the operator with force feedback to control the microrobots. In particular, virtual interaction forces were computed and transmitted to the human operators to guide them in performing

path following tasks. The operating field of the microrobots was haptically rendered to avoid contacts with obstacles. Finally, a basic set of experimental trials were conducted, demonstrating that the average path tracking error was reduced by **67**% when haptic feedback was used.

TABLE OF CONTENTS

LIST OF FIGURES

LIST OF TABLES

Chapter 1

Magnetically Actuated Simple Millirobots for Complex Navigation and Modular Assembly

1.1. Introduction

Untethered robots, miniaturized to the millimeter scale, have a promising future in biomedical and engineering applications due to their design simplicity, scalability, diverse locomotive techniques, and control flexibility during different manipulative tasks. Over the last few decades, advances in research at the millimeter and smaller length scales have brought great interest in the development of untethered locomotive devices [52]. In millirobots, untethered components have dimensions as small as 1 mm and macroscale forces, such as bulk inertia forces, dominate their mechanics [151]. Therefore, the design and implementation of different locomotive techniques for millibots are important for their success in real world applications.

Over the last few decades, several research projects have been carried out at meso or smaller length scales to achieve bio-inspired locomotive techniques such as crawling [67, 120, 137], running [69], walking through slip-stick motion [118, 119], helical screw propulsion [110, 112, 133, 135], swimming [25, 36, 118], rolling [70, 84, 165], snake-like motion [93], and tumbling [18, 85, 131]. However, many of these robots have limitations in fabrication, control, and miniaturization to access confined regions, as their motion modes have been dependent on the complex structure and frictional forces of surrounding external surfaces. Pivot walking, tapping, galloping, dragging, hopping, and bouncing are some surface locomotion modes that have been achieved at the macro-scale in several investigations [57, 87, 89, 140, 159, 161, 163, 184, 185]. However, those have been impulsive or inertially actuated macro-scale robots and limited in scalability, power, and control using complex on-board circuitry.

The development of a magnetic stereotaxis system [116], to explore untethered actuation, advanced the principles of millirobot actuation. Since then, magnetic actuation has been a viable wireless control method over small-scale robots [35, 37, 92]. Mahoney *et al.* [110, 112] investigated different magnetic control techniques to actuate an untethered magnetic tool; while their investigation could develop different global and local magnetic control methods, their robot was limited to the locomotion of rolling or helical screw propulsion. Kim *et al.* [93] developed a snake-like motion mechanism using a three-axis Helmholtz coil system. Their robot could mimic three types of snake locomotion through manipulation of the external magnetic field, which showed future promise in achieving unique locomotion modes through magnetic field manipulation. Petruska and Abbott [133] constructed and used an omnidirectional electromagnet to drive a helical capsule-endoscope mockup through a transparent lumen. Popek *et al.* [135] could propel a screw-type magnetic capsule using a single rotating magnetic dipole. The screw-type magnetic capsule was equipped with an embedded permanent magnet and Hall-effect sensors, to be localized using a rotating magnetic-dipole field. However, for magnetically actuated robots, Hall-effect sensor-based methods are challenging due to magnetic field interference between the actuating electromagnetic coils and the magnet located on the sensor [151]. Miyashita *et al.* [118] developed an electromagnetically actuated untethered origami robot which could self-fold, walk, swim, and degrade in different environments. Walking had been achieved through oscillatory magnetic field actuation by permitting the front and back body parts to contact the ground through slip-stick motion alternately. Building on this work, Miyashita *et al.* [119] designed and fabricated another biocompatible origami robot that could be encapsulated in ice and actuated through an esophagus to release an embedded drug layer into a wounded region passively. Although, those robots could be used for control and actuation through walking and rolling locomotion in artificial bio-environments, their control and limited locomotion modes raise a lot of uncertainty regarding their applicability in a confined region. Bi *et al.* [18] could achieve side-wise and length-wise tumbling locomotion with a magnetic robot, which could actuate through complex terrains, however, it had limitations regarding an available control sys-

tem for manipulation in minimally accessible regions. Vogtmann *et al.* [166] developed a hexapedal magnetically actuated robot which could walk with a speed of greater than 5 body-lengths/second. Their work demonstrated how the complainant mechanism of legs and simple control system could be used to achieve faster locomotion. However, they had limitations in fabrication and control feasibility at smaller length scales. Pierre and Bergbreiter [134] studied legged locomotion at small-scale and demonstrated the versatility of magnetic actuation to study terrestrial locomotion. Although many magnetically actuated robots have been designed and explored at different length scales, no untethered scalable robot has been invented which could be capable of multi-modal locomotion with a simpler design, functional in the irregular surface, and actuated through a minimally accessible region.

Therefore, in this chapter, we present a magnetically actuated untethered millirobot, which is simple in design, capable of producing multiple surface motion modes (pivot walking, tapping, tumbling, corner maneuvering, etc.), is power-efficient, and shows immense promise in both scalability and modularity, especially in minimally accessible regions and performing different bio-engineering tasks. Multi-modal locomotion of our robot enabled itself to actuate through confined regions, such as a maze-like path and an esophagus-like bent tube. Moreover, based on this, we have combined multiple millirobots together to create a magnetically actuated stag beetle which could successfully transport an object, and a magnetic carbot which could move through a maze. Based on our current research, we plan to achieve modularity by fabricating and programming simple modular subunits, which can form both scalable and configurable structures. These structures can be used for large-scale manipulation and then disassembled into simple robotic structures for small-scale manipulation tasks. Further, we plan to achieve real-time feedback control for the modular sub-units.

1.2. Millirobot design and motion modes

The magnetically actuated untethered millirobot presented in this chapter is rectangular-shaped with cylindrical permanent magnets embedded in each of its two ends as shown in Fig. 1.1. When an external magnetic field vector with an alignment different from that of the longitudinal axis of the robot is applied, a magnetic torque is induced on the millirobot until it realigns itself with the field. Thus, the millirobot can be actuated by changing the magnitude and the direction of the magnetic field vector.

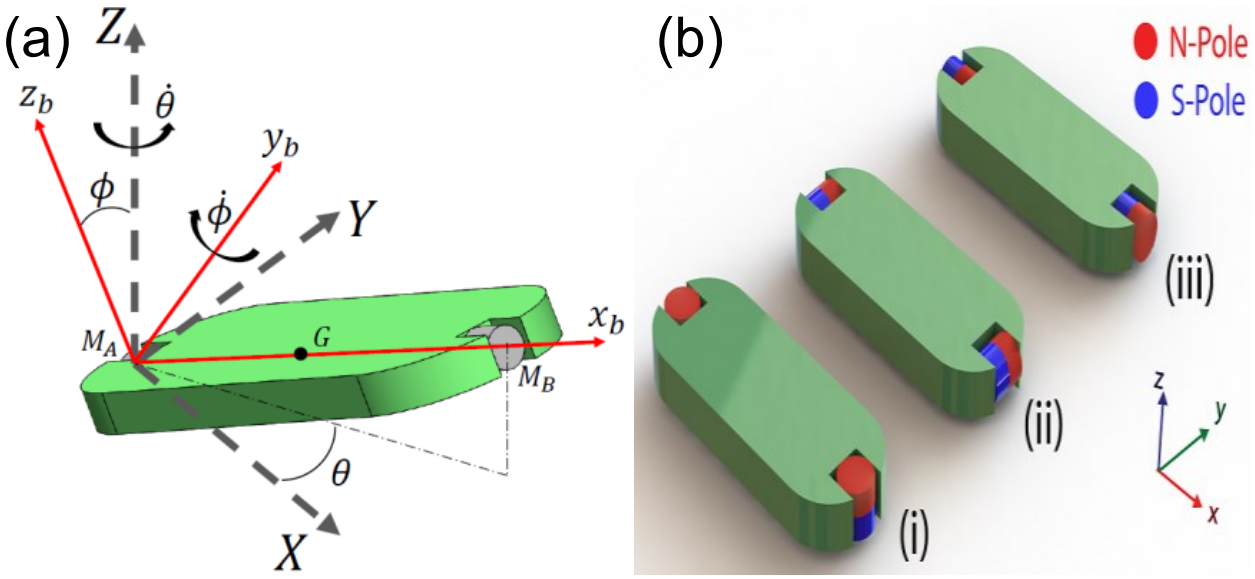

Figure 1.1. Robot design and coordinate system. **(a)** Dashed-black and red axes represent respectively the inertial (XYZ) and body ($x_by_bz_b$) frames of the robot in Cartesian space. θ and ϕ show rotations between the two frames of references. **(b)** The embedded permanent magnet pair with different configurations. Here, red represents the north pole and blue represents the south pole.

We considered several possible ways of attaching the two permanent magnets to the robot body. The orientation of the permanent magnets with respect to the body will affect the possible locomotion modes. Figure 1.1(b) shows three ways the magnets can be attached to the body. When they are arranged in the manner shown in (i) and (ii), only tapping and tumbling modes are achievable. In addition, arrangement (iii) not only can generate pivot

walking, but also can produce more efficient tapping and tumbling modes. The arrangement of the magnet pairs in terms of polarities shown in Fig. 1.1(b) leads to optimal torque generation. Also, increasing the number of permanent magnets along the robot axis will only amplify the induced magnetic torque. Therefore, only two permanent magnets were attached to the robot's body.

Based on this basic concept, various locomotion modes can be generated. Here, we listed and demonstrated four possibilities. The tapping, pivot walking, and tumbling locomotion modes listed here were achieved previously in studies [87,89,184,185] using inertial actuation schemes. Yet, magnetic actuation provides a mean for more compact and miniaturized designs since it eliminates on-board actuation mechanisms and power supplies. Pivot walking is achieved by successively alternating the direction of the magnetic field vector in negative and positive z-direction. When the magnetic field vector orients in the negative z-direction, the induced magnetic torque presses one end down while the other end is lifted up. Subsequently, while having a pivot formed at the pressed end, a counter-clockwise magnetic torque τ_z is applied. This causes the robot to rotate forward by an angle of θ_i in the $x-y$ plane. In the next step, the orientation of the magnetic field is reversed, and the pivot moves to the other end. A clockwise torque τ_z is then applied to rotate the robot by θ_{i+1} about the new pivot point. Repeating this process, locomotion along a desired path is generated as shown in Fig. 1.2(a).

Tumbling motion can be created by successively applying step torques τ_y^i about y axis to progress in the x direction (Fig. 1.2(b)). During this motion mode, one end forms a pivot, while the entire body rotates about that pivot. Figure 2(b) shows the tumbling mode where the red and black arrows show the direction of progression and the applied torques respectively. This type of locomotion is suitable for operating in narrow channels. However, the channel height should accommodate the longitudinal dimension of the robot.

The millirobot corner maneuvering motion is used to perform tight corner turns. It is similar to the tumbling mode, where the robot is erected along the longitudinal axis. When the robot reaches the upright position, τ_z is applied to change the orientation of the robot

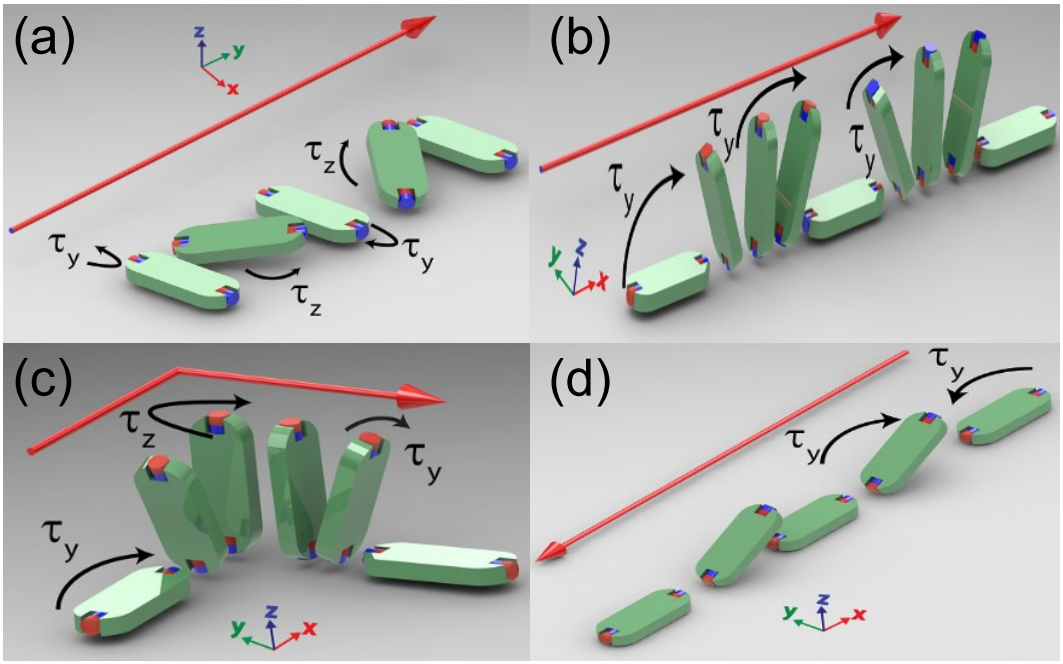

Figure 1.2. Demonstration of basic modes of motion by $15 \times 4 \times 2\,\mathrm{mm}^3$ sized millirobot. Depending on the direction of applied rotating magnetic field, multiple modes of locomotion are produced. **(a)** Pivot walking is achieved by lifting one end and forming pivot point in the other end by applying torque τ_y, then, the torque τ_z rotates the millirobot about the formed pivot; the process is then repeated in the opposite direction. **(b)** Tumbling is created by applying continuous step torques τ_y. **(c)** Corner maneuvering is made when sharp turn is required at corners. When the millirobot reaches the upright position, a torque τ_z is applied to turn the millirobot to the desired direction. **(d)** Tapping is attained by repeatedly applying positive and negative torques (τ_y and $-\tau_y$) that lift and release the trailing end and generate forward progression.

to progress in another direction. Figure 1.2(c) depicts the corner maneuvering mode where the red and black arrows represent the direction of motion and the applied torques on each pose respectively.

Lastly, tapping motion is made by first applying a clockwise torque τ_y to form a pivot point at the leading end (Fig. 1.2(d)). Next, a counter-clockwise torque τ_y presses the trailing end, and generates a forward progression in the x-direction as shown in Fig. 1.2(d). In this mode, one end (trailing) is tapping, while the other end (leading) maintains contact with the surface. The advantage of tapping mode is that the robot can move through narrow

spaces. Compared to the tumbling mode, less space is needed in the z-direction, and the only limitation is the width of the robot.

Figure 1.3 shows the feasible motions and the space restrictions of each mode. The tumbling mode requires more space in the z direction, the pivot walking mode requires the smallest space in the z direction but necessitate wider space in x direction. Finally, the tapping mode requires narrowest space in x direction and moderately higher space in the z direction.

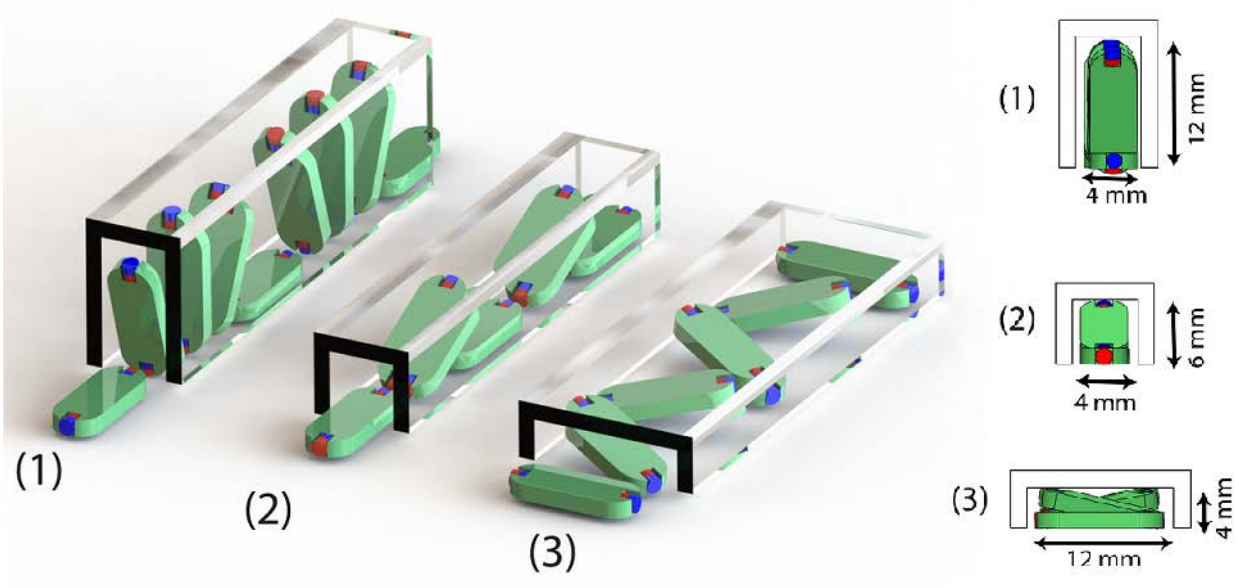

Figure 1.3. Feasible motion and space limitation of 10 mm robot. (1) The tumbling mode. (2) The tapping mode. (3) The pivot walking mode.

1.3. Equations of motion

The equations of motion are derived using Newton's method. The position of the center of mass (G) of the robot (x, y, z) and two orientation angles shown in Fig. 1.1(a) are taken as the states of the system. The robot experiences different forces and torques; a weight (mg), a surface normal force (N), a friction force (F_k) in the opposite direction of the velocity, and two external magnetic torques (τ_y, τ_z). Here, F_k depends on N, the sliding friction coefficient

μ, and the direction of the velocity of the contact point ($\vec{e}_V$). The millirobot is assumed to be symmetrical in three directions, so the moment of inertia I_m in the body frame ($x_b y_b z_b$) can be given as:

$$I_m = diag(\begin{bmatrix} I_x & I_y & I_z \end{bmatrix}) \tag{1.1}$$

where, I_x, I_y, and I_z are the moment of inertia along x, y, z -axes, respectively (they are not necessarily equal).

In the locomotion of the system, we assume that two magnetic moments M_A and M_B are acting at the pivot point. The position of one of the pivot points (A) is considered as (A_x, A_y, A_z). By using the Newton's law of motion, the equations of motion can be written as follows:

$$m\ddot{x} = (F_k\, \vec{e}_V).\vec{i} \tag{1.2}$$

$$m\ddot{y} = (F_k\, \vec{e}_V).\vec{j} \tag{1.3}$$

$$m\ddot{z} = mg - N \tag{1.4}$$

$$I_z\ddot{\theta} = -\tau_z + F_k \sin\gamma\, r \sin\phi \tag{1.5}$$

$$I_y\ddot{\phi} = -\tau_y + F_k \cos\gamma\, r \cos\phi - N\, r \sin\phi \tag{1.6}$$

where $\{i,\ j,\ k\}$ are the unit vectors of the inertial frame (XYZ), r is the distance from G to A, γ is the angle between $\vec{e}_V$ and the x_b-direction, respectively. The kinematic constraint of the pivot point allows the derivation of the following additional equations:

$$A_x = x - r \sin\phi \cos\theta \tag{1.7}$$

$$A_y = y - r \sin\phi \sin\theta \tag{1.8}$$

$$A_z = z - r \cos\phi \tag{1.9}$$

where these second derivatives are considered as constraint equations. As the system undergoes stick-slip motion, we assume that $F_k = N\,\mu$. To solve the equations of motion,

we realize that we have 6 unknowns ($\ddot{x}$, $\ddot{y}$, $\ddot{z}$, $\ddot{\theta}$, $\ddot{\phi}$, N) and five equations. To resolve this paradox, we use the pinned assumption [131]. There are different types of possible solutions that can be enumerated as:

- If $N < 0$, it means that the robot does not have any contact with the ground, so $N = F_k = 0$.
- If $F_k > F_{s_{max}}$, where $F_{s_{max}} = N\,\mu_s$, it means that a pinned point is slipping on the surface and $\ddot{A}_z = 0$

1.4. Electromagnetic coil setup

A large-scale magnetic field controller was constructed to actuate the millirobots presented in this chapter. The large-scale coil system is a nested Helmholtz configuration capable of producing uniform rotating magnetic fields in all three dimensions. The separation distance between each coil pair is directly related to their radii. The y-coil pair has an outer diameter of 50.4 cm, the x-coil pair has an outer diameter of 38.2 cm, and the z-coil pair has an outer diameter of 28 cm. The inner diameters of the y, x, and z coils are 40.1 cm, 29.2 cm, and 20 cm, respectively; coil thicknesses are 5.16 cm, 4.48 cm, and 3.8 cm. The large size of the coils allows for a total working distance of $15 \times 12 \times 8$ cm^3 at the center of the coil configuration. The coils were fabricated by Stonite Coil using insulated 13 gauge circular copper wire while all the support structures were printed using polylactic acid (PLA) on an Ultimaker 2 Extended+ at an 0.6 mm layer height. An isometric CAD drawing of the coil system, showing the different coil positions, can be seen in Fig. 1.4(a), while the front view of the actual coil system can be seen in Fig. 1.4(b). Nicknamed the 'Death Star' by the laboratory, it is one of the largest and most powerful Helmholtz configurations being used for small-scale robotics research.

When ten amps of current are applied to each coil, the system can produce magnetic fields above 20 millitesla (mT). The exact magnetic field profile for each coil pair can be seen in Fig. 1.5(a) when ten amps of current is applied. Its considerable working distance

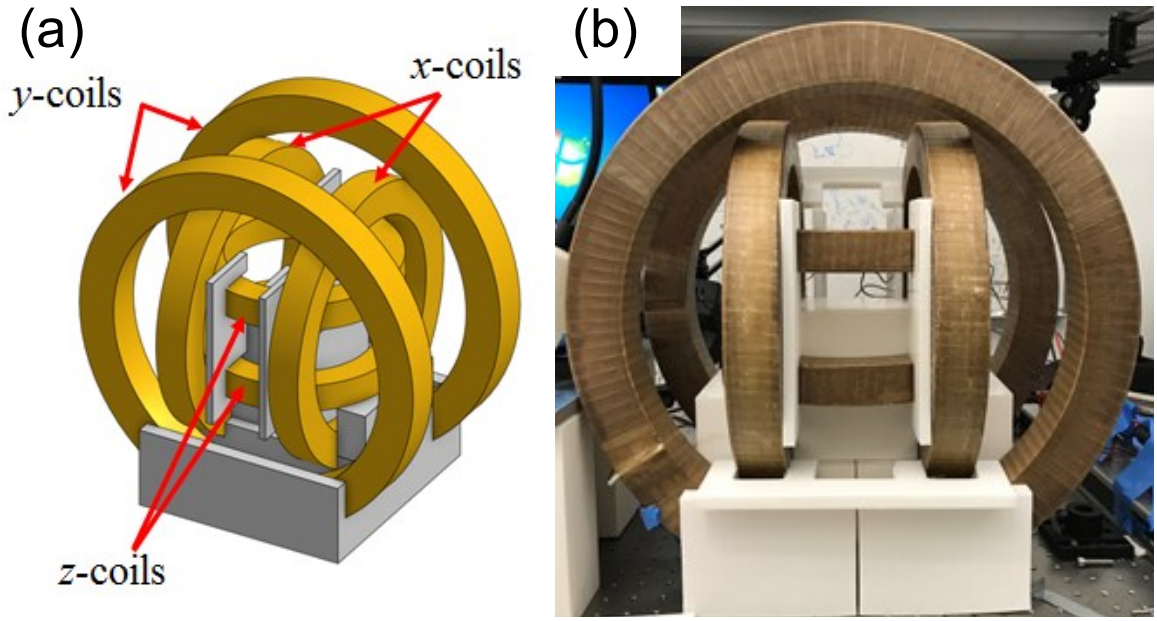

Figure 1.4. Large-scale, high-powered, nested Helmholtz coil configuration (BAST Lab). **(a)** Isometric view of the large-scale nested Helmholtz coil system (Death Star). **(b)** Front view of the actual coil system.

and significant magnetic field flux densities give millirobots ample space to maneuver and enough torque to produce any motion mode. Finally, due to the large size of the coils, heat dissipation from the coils does not affect any sample placed within the system. To demonstrate this, a room temperature beaker of saline water was placed inside the center of the coil system for 30 minutes while 10 amps of current was applied. The results can be seen in Fig. 1.5(b), where no significant change of temperature was detected in the sample, which maintained room temperature throughout the experiment. The PLA, which composes the millirobots and has a low melting temperature, would not be effected by the coil systems prolonged operation. The coil system was designed using the procedure outlined in [1]. Each coil pair is linked with its programmable power supply (Kepco, BOP 100-10M), and linked to a National Instruments data acquisition (DAQ) board. By using the DAQ board, the power supplies generate sinusoidal outputs to the coils. They can create uniform rotating magnetic fields with any user-specified time-independent magnitude and frequency. These

signals are user-specified and controlled using a customized C++ program; specific magnetic torque patterns for each coil pair were pre-specified for each motion mode. A digital camera was used to record videos of the experiments at 30 frames per second (fps).

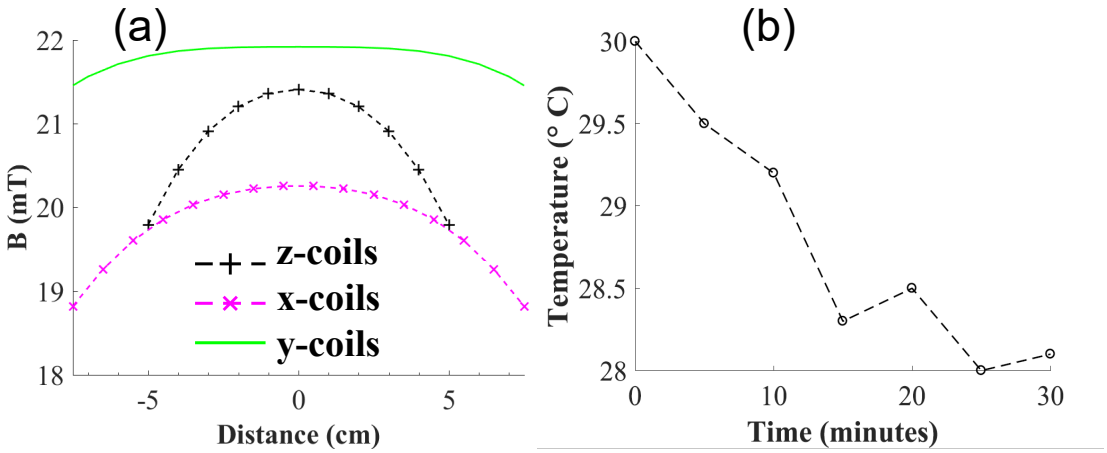

Figure 1.5. **(a)** Magnetic field flux density vs. distance profile, at 10 amps of current, measured from the center of the working space to the maximum working space along the x-direction. The z-coil has a smaller profile since it is has the smallest separation distance, but does not limit the 2D motion of the millirobots. **(b)** Temperature vs. time profile for saline solution placed in the center of the system when 10 amps of current was applied to each coil pair. Dashed line connecting the points in (b) was added to guide the eye.

In this study, one of the main goals is to represent the motion of a magnetic millirobot under the effect of a stationary electromagnet system. We propose a millirobot that is a rigid body embedded with two permanent magnets M_A and M_B. The magnetic moment M is assumed to have a constant magnitude and be rigidly connected to the frame of body. Figure 1.1 depicts schematic of the robot with reference frames.

The torque on the magnet can be expressed as follows:

$$\tau_A = M_A \times \bar{B} \tag{1.10}$$

$$\tau_B = M_B \times \bar{B} \tag{1.11}$$

where $\bar{B}$ is the vector of applied magnetic field's flux density. The torque tends to align the

magnetic moment with the applied field. In our case, the torque is aligned to the x_b axis of the body with the field. In this configuration, we are able to move the center of mass of body (G) and perform rotations of the in-plane (θ) and out-of-plane (ϕ) angles. We should note that we are unable to perform rotation about the long axis of the body (x_b). The state variables of the system are x, y, z, θ, ϕ, where x, y, z are the coordinates of the center of mass, θ, ϕ are the body frame rotation angles.

Each electromagnet creates a magnetic field throughout the workspace. At any given point in the workspace P, the magnetic field due to actuating a set of given electromagnets can be expressed as follows:

$$\bar{B}(P) = \sum_{n=1}^{N} \bar{B}_n(P) = \sum_{n=1}^{N} \bar{K}_n(P) I_n \tag{1.12}$$

where subscript n represents the nth actuated electromagnet, N is the number of electromagnets, I_n is the current value flowing through the nth electromagnet, and $\bar{K}_n(P)$ is a unit vector, thus the vector $\bar{B}(P)$ varies linearly with the current through the electromagnet. The individual field contributions are decoupled, and the fields can be individually measured and then linearly summed. The summation can be expressed in the matrix form:

$$\sum_{n=1}^{N} \bar{K}_n(P) I_n = \begin{bmatrix} \bar{K}_1 & \bar{K}_2 & \cdots & \bar{K}_n \end{bmatrix} \begin{bmatrix} I_1 \\ I_2 \\ \vdots \\ I_n \end{bmatrix} = \mathbf{K}(P)\mathbf{I} \tag{1.13}$$

where $\mathbf{K}(P)$ is the precomputed matrix at each point in workspace of magnetic field. To find the magnetic force, we need to find the derivative of the magnetic field in specific direction.

The derivative in specific e-direction can be expressed as follows:

$$\frac{\partial \bar{B}(P)}{\partial e} = \begin{bmatrix} \frac{\partial \bar{K}_1}{\partial e} & \frac{\partial \bar{K}_2}{\partial e} & \dots & \frac{\partial \bar{K}_n 1}{\partial e} \end{bmatrix} \begin{bmatrix} I_1 \\ I_2 \\ \vdots \\ I_n \end{bmatrix} = \mathbf{K}_e(P)\mathbf{I} \tag{1.14}$$

The magnetic torque and force on the magnetic moment M at point P are directly related to the current. The use of magnetic torque and force requires knowledge of the system's pose and magnetic moment configuration. In our case, we control the direction of the magnetic field, but in this case the millirobot will align with the applied field. Thus, we need to have the magnitude of M and measure the millirobot's position and orientation at point P.

The field strength, rotation direction (CW/CCW), and rotation frequency of the magnetic field can be controlled through our magnetic control system. For example, in xy-planar control, the resultant field can be expressed as

$$\bar{B} = \mathbf{K}(P)\mathbf{I} \begin{bmatrix} \sin\psi \sin\omega t & \cos\psi \sin\omega t & \cos\omega t \end{bmatrix}^T \tag{1.15}$$

which rotates with angular velocity ω around the unit vector

$$\bar{n} = \begin{bmatrix} -\cos\psi & \sin\psi & 0 \end{bmatrix}^T \tag{1.16}$$

which corresponds to the desired direction, where ω is the rotational frequency, and ψ is the rotation of the plane of the rotating field. For our Helmholtz coil, the magnitude of the field

$|\bar{K}_i|$ of a pair of coils can be modeled as:

$$|\bar{K}_i| = \frac{\mu_0 n\, R_{coil}}{2\left(R_{coil}^2 + d^2 - 2D\, d + D^2\right)^{3/2}} + \frac{\mu_0 n\, R_{coil}}{2\left(R_{coil}^2 + d^2 + 2D\, d + D^2\right)^{3/2}} \tag{1.17}$$

where μ_0 is the permeability constant, n is the number of turns of the coils, R_{coil} is the radius of the coils, D is the distance between a pair of coils, and d is the position between the coil. At the center of the coil, which is the position we are interested in, the position d is equal to zero. For more details on the Helmholtz coil configuration, refer as to [32].

1.5. Experimental verification

Various types of motion testing have been conducted to analyze the behavior of the robot as well as the actuation mechanisms proposed in this study. Figure 1.6 shows the experimental verification of the basic modes of motion for $15 \times 4 \times 2\,\text{mm}^3$ sized millirobot.

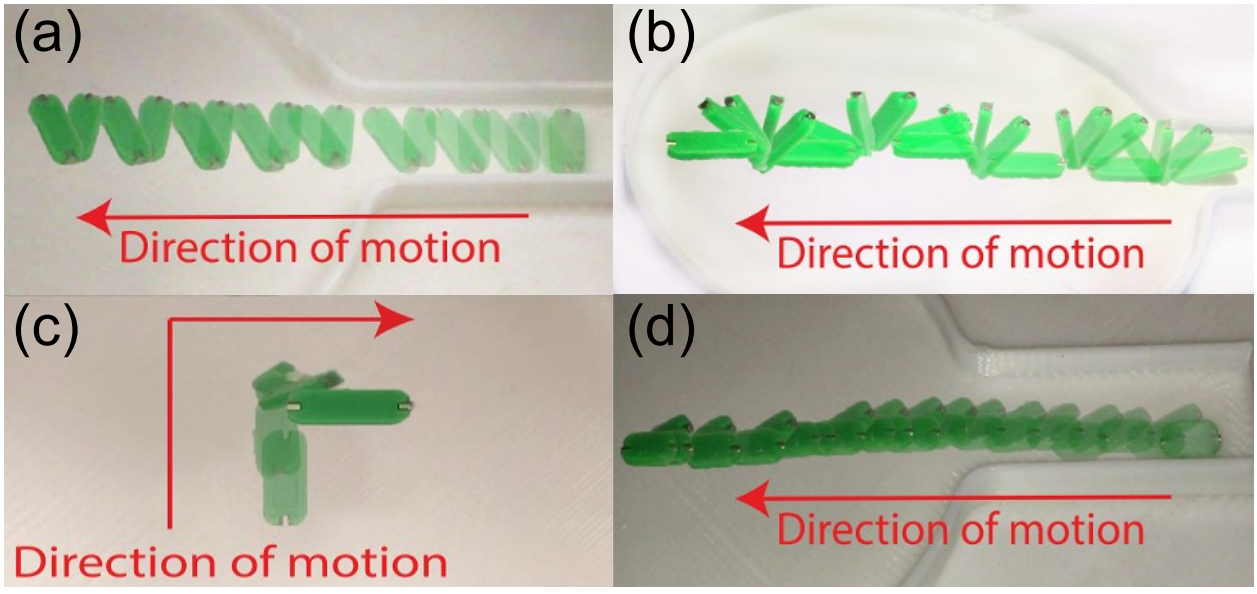

Figure 1.6. Demonstration of basic modes of motion by $15 \times 4 \times 2\,\text{mm}^3$ sized millirobot. **(a)** Pivot walking. **(b)** Tumbling. **(c)** Corner maneuvering. **(d)** Tapping.

Figure 1.7(a) depicts the applicability of the novel pivot walking strategy, where the millirobot follows a desired path that includes sharp corner. As seen in Fig. 1.7(a), the pivot walking motion mode is both robust and stable. However, this strategy requires a wider operating space to be functional. To overcome this limitary space for locomotion, one can take advantage of the strengths of each mode by creating a combined motion mode; pivot walking mode is suitable to perform fast and robust motions in wide spaces, while tapping mode is better used in tight spaces, and the corner maneuvering mode is ideal in handling sharp corners.

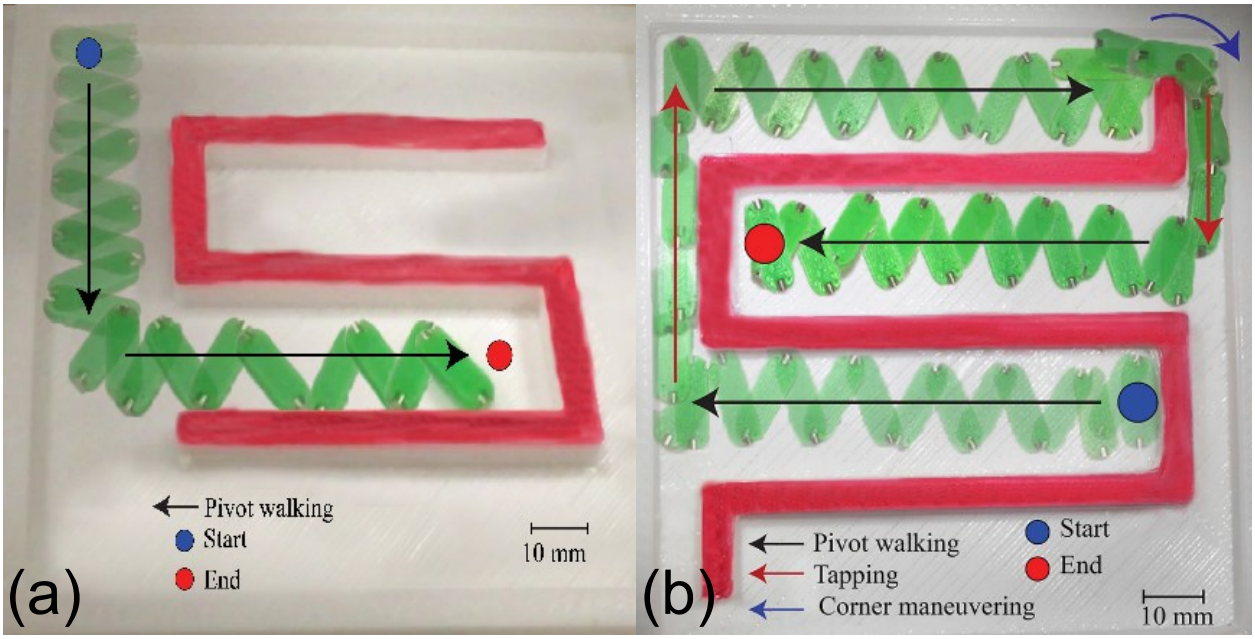

Figure 1.7. Multi-modal motion modes by $15 \times 4 \times 2\,\text{mm}^3$ sized millirobot in a maze. **(a)** Pivot walking motion: the millirobot is migrating remotely guided by a rotating magnetic field through pivot walking mode. The robot walks forward, changes its direction, and then walks inside the maze. **(b)** Combined motion modes: the millirobot travels inside a maze by switching between the proposed modes of motion based on the space of the path. It uses pivot walking in wider space, tapping in narrower, and corner maneuvering to handle sharp corners.

Figure 1.7(b) shows a combined motion mode, where the robot starts with pivot walking mode and when it reaches the narrow channel, tapping mode is used in this tight space until

it reaches the wide channel again. The robot taps until it encounters the sharp corner. Then, it uses the corner maneuvering mode to perform an in-place sharp turn. Then, it continues with tapping again until it reaches the wider space. Subsequently, the pivot walking mode is used to reach the final destination. The experimental testing was conducted without any position feedback. We plan to extend our work by conducting longer duration and more complicated experiments. These future experiments will include camera based visual feedback to localize the millirobot.

1.5.1. Parametric Analysis

The comparison of progression velocities of individual motion modes at different magnetic field frequencies is shown in Fig. 1.8(a). For pivot walking and tumbling, increasing the frequency results in faster progression velocity. But at higher frequencies, our millirobot is subject to more slippage. For tapping, increasing the frequency does not lead to higher velocities. We found a critical frequency f_c of 50 Hz, where the velocity is maximized compared to other frequencies. In general, pivot walking mode has the largest progression velocity compared to the other two modes. The slowest mode was tapping. In addition, in pivot waking, there is one contact point at a time between the millirobot and the ground. At high switching frequencies the millirobot may slip at contact with points. This slippage can be reduced by incorporating materials with higher static friction coefficient (such as rubber) at the contact points.

In addition, we investigated the effect of robot body length and sweep angle on pivot walking and the effect of step angle on tumbling. For pivot walking mode, Figure 1.8(b) depicts the variation of the progression speed with respect to robot length while other parameters are fixed. As one can see from the figure, increasing the length of the robot leads to higher progression speeds. This is due to the fact that for the same sweep angle, the traveled distance is $x = \frac{L}{2}\sin\theta$, where L is the robot length and θ is the sweep angle. Therefore, longer robots will travel longer and faster than the shorter ones. Figure 1.8(c) presents the progression velocity as a function of sweep angle for 5 mm and 10 mm long millirobots. For

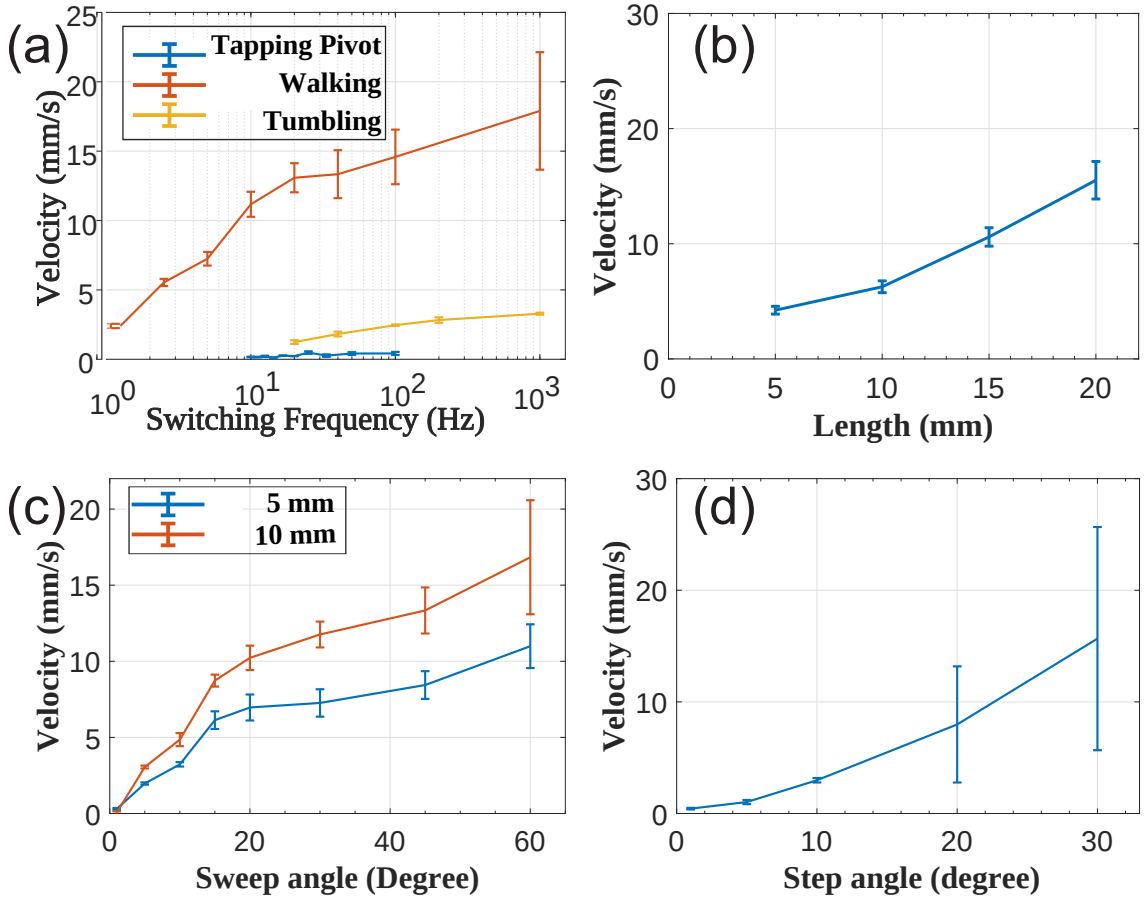

Figure 1.8. Parametric analysis. **(a)** Comparison of progression velocity between motion modes of $10 \times 4 \times 2\,\mathrm{mm}^3$ sized millirobot. **(b)** Pivot walking: variation of progression velocity as a function of robot's length. **(c)** Pivot walking: variation of velocity as a function of sweep angles. **(d)** Tumbling mode: variation of velocity as a function of angle steps.

each length increasing the sweep angle results in longer distances as well as higher progression velocities.

For tumbling mode, Fig. 1.8(d) presents the progression velocity with respect to different angle steps while the other parameters are fixed. The angle step represents the angle increment of the robot to achieve full rotation. As can be seen for a 10 mm long millirobot, increasing the step angle results in higher velocities, however, this can also result in increased slippage and unpredictable motion once the step angle becomes larger than 15 degrees. But, for angle steps larger than 15 degrees, the robot is subject to slippage and unpredicted

motion.

1.6. Biomedical and engineering applications

Here we present the feasibility and modularity of our magnetically actuated millirobot for three potential applications. First, our millirobot was tested inside gradually elevated curved tube. It shows that the millirobot can be potentially used for future exploration of esophagus-like structures for endoscopy and ENT surgical procedures. A 12.7 mm inner diameter transparent hose was used to mimic tubular structures in the three dimensions. The dimension of the millirobot used in this experiment is $5 \times 4 \times 2$ mm^3. An experiment was conducted whereas the elevation of the tube was varied. For this purpose, a special support structure was built (see Fig. 1.9(a)). In this experiment, pivot walking was initially used; after a short period of time (9s) the motion mode was changed to tumbling in order to overcome slippage caused by the incline. Once the slippage was overcome, the millirobot remained in the tumbling mode for the remainder of the experiment.

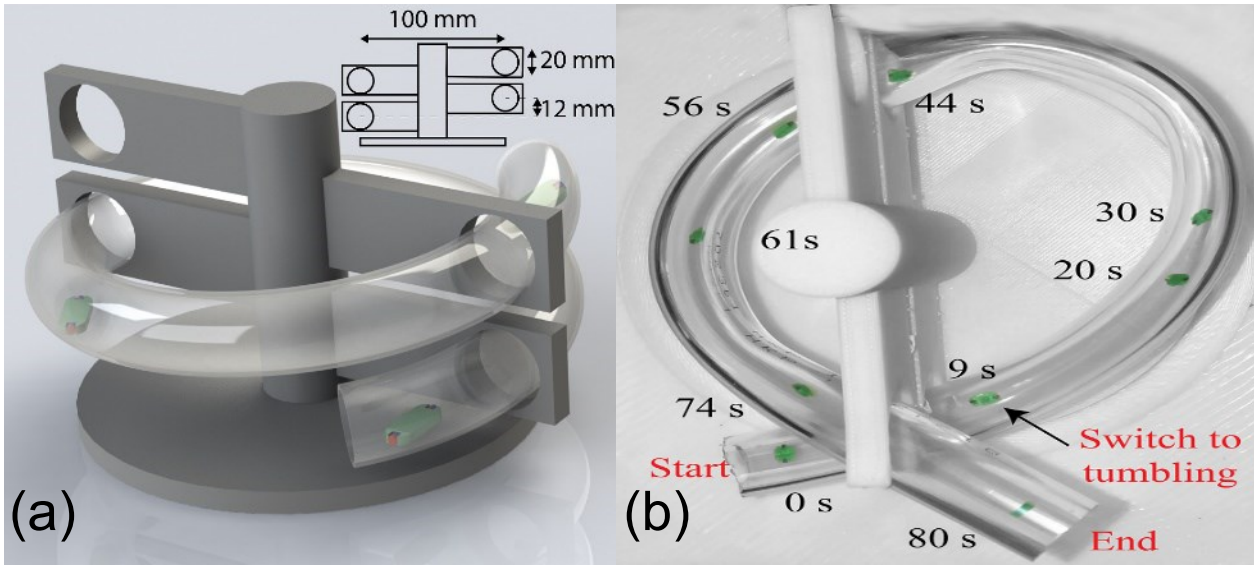

Figure 1.9. Millirobot is navigating inside a helical tube to emulate an esophagus-like structure. **(a)** CAD model of the support being used to hold the tube with 7° grade. **(b)** Robot trajectory inside a helical tube where z motion is now achieved.

The millirobot, as a modular sub-unit, can be used to construct more complicated multi-functional robotic devices. One of such devices is a stag beetle robot shown in Fig. 1.10. In this robot, two modules are mounted on a spine. Then the locomotion takes place by inducing pivot walking into the two modules of the beetle. Adding more than one pivot walker increases the traction by adding another ground contact point. In addition, the actuation force is doubled due to the addition of the second pivot walker. Therefore, the stability and robustness of walking on the surface and the accuracy of the direction of motion are improved. Figure 1.10(d) shows the stag beetle robot is navigating in a 2D maze-like environment while pushing payload. This example also demonstrates manipulation potentials of the magnetically actuated millirobot. Finally, since these experiments were conducted without any position feedback, the beetle robot has to walk slowly and adjust its orientation to navigate inside the maze. In future work, we will use visual feedback to estimate the robot position, then we can increase the navigation speed of the beetle robot.

Finally, we developed a car robot (carbot) using four millirobots in the form of wheels. In each wheel, the same configuration of magnet pairs are used. But, instead of attaching them to the rectangular-shaped body, we attached them to a circular disc-shaped one. The two discs are connected through an axle. The front and back wheels are mounted on a main body of the carbot as shown in (Figs. 1.11(a) and 1.11(b)). Figure 1.11(c) shows a 3D printed carbot in motion, where the carbot navigates through a pathway.

1.7. Discussion and Conclusion

This study introduces the possibility of developing a scalable, configurable, low-cost millirobot that is very simple and easy to manufacture. The millirobots can be remotely controlled using rotating magnetic field which allows them to perform a rich set of agile locomotion modes and tight cornering maneuvers. These robots can also be used as modular components of more sophisticated devices.

Most of the millirobots previously developed can operate well in a single motion mode. Yet, a multi-function robot can offer great advantages in agility and performance of complex

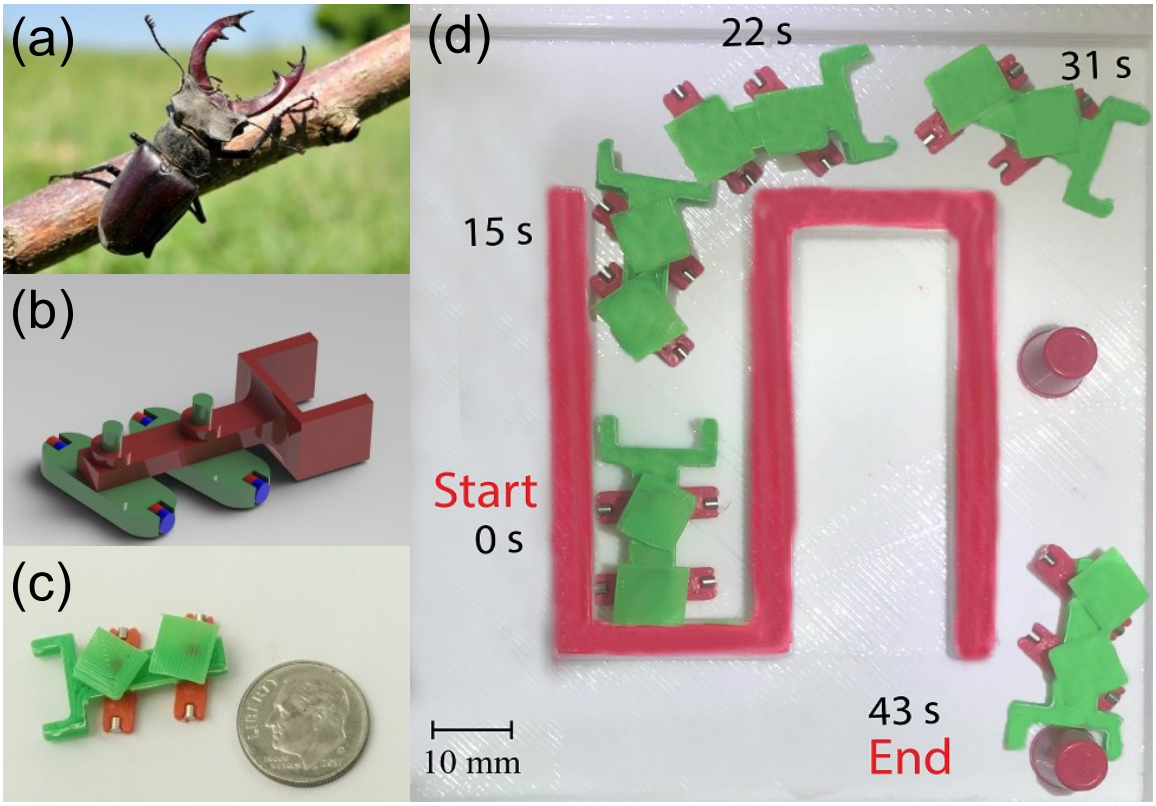

Figure 1.10. Bio-inspired stag beetle robot. **(a)** A stag beetle from [102]. **(b)** The CAD model of the beetle robot, where two millirobots have been arranged in parallel on a spine created beetle-like robot that is capable of moving on a 2D surface. Applying pivot walking mode on the modules makes the robot to walk in any desired direction. **(c)** The 3D printed stag beetle robot size compared to a quarter (diameter 24.26 mm). **(d)** Demonstration of object manipulation using stag beetle robot, where the beetle robot moves, rotates and pushes using pivot walking technique.

tasks. We established that by attaching two permanent magnets to a simple plastic member, and through the use of magnetic actuation, one can make robots capable of performing highly sophisticated motions. Such devices can find use in biomedical applications such as *in vivo* drug delivery, *in vitro* manipulation, and endoscopic tasks. In addition, they can be incorporated into non-medical micro-manipulation and manufacturing applications.

Having multiple modes of operations enhances the capabilities of a millirobot. Each mode would have its own advantages and drawbacks. For example, pivot walking, while being the fastest and the most stable mode, requires wider space in the x direction. On the other

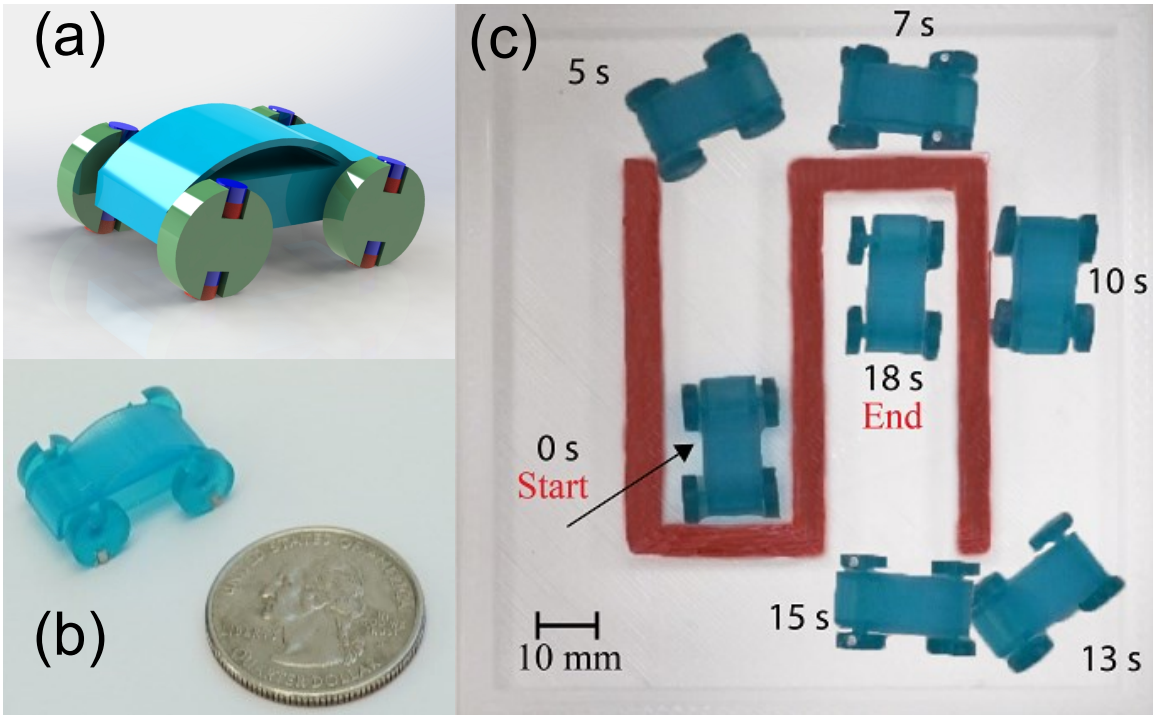

Figure 1.11. Carbot. **(a)** The CAD model of the magnetic carbot, where, four disc-shaped millirobots have been arranged to create a magnetic carbot that is capable of moving on a 2D surface. Applying tumbling mode on the modules makes the wheels to rotate and move the carbot in any desired direction. **(b)** The 3D printed carbot compared to a quarter (diameter 24.26 mm). **(c)** The 3D printed carbot robot is navigating through a path which consists of straight lines and sharp corners.

hand, tumbling has lower speed and requires wider space in the z direction. Tapping mode has the minimum space requirement, however, it is prone from possible slippage and slow progression velocities.

In summary, we developed a basic untethered millirobot which is very simple in design, highly scalable, easier to fabricate at low cost, capable of producing multimodal surface motions, and shows scope of modularity by assembly of simple sub-units to create complex structures. We demonstrated the pivot walking for the first time at millimeter length-scale as a novel way of producing stable and efficient locomotion. We demonstrated experimentally that several surface locomotion modes could be generated by a simple millirobot which enable it to actuate through confined spaces such as maze-like path and esophagus-like

bended tube. Finally, we established the scope of modularity with millirobots in creating more sophisticated devices such as a stag beetle and a carbot [6].

Future works will include incorporating position feedback using external cameras to conduct precise and more complicated experiments. In addition, adding a high friction material to the pivot points to increase the traction and decrease the slippage will be considered. Furthermore, more complicated multi-functional robotic devices will be considered and designed. We will also consider swarm control and work on reconfigurable millirobots.

Chapter 2

Feedback Control of Millimeter Scale Pivot Walkers Using Magnetic Actuation

2.1. Introduction

Biological inspired locomotion and the growth in need for mobility in challenging and unknown environments have motivated many researchers to design different miniature robots. These robots can be listed as conventional wheeled, crawling and snake-like, legged, and hopper. Recently, traversability in irregular environments has become an important feature in the design of robots. Small-scaled robots show great potential capabilities in maneuverability and reachability in such environments. Also, these robots can benefit from untethered actuation mechanisms and freed from limitations imposed by onboard actuators and power sources. Untethered tiny robots can be actuated by external forces, such as electromagnetic fields [128, 147], acoustic waves [4], and light [146, 148, 155]. In this paper, we present a millimeter-scale magnetic robot that can be steered by an external magnetic field.

Small scaled robots actuated and controlled by external magnetic fields can be used in different applications such as accessing and manipulating objects in tight spaces. Various locomotion modes has been developed for these types of robots such as *Pulling/Pushing* [2], *Tumbling/Rolling* [165], *Helical Thrusting* [22], *Swimming* [47], *Crawling* [71], *Stick-Slipping* [131], and *Pivot Walking* [6]. These locomotions can be carried out by rigid or soft mechanisms [42].

Here, we summarize these different motion modes. Steering a permanent magnet can generate a magnetic force and subsequently pull or push a magnetic body on a dry surface or in a fluid environment. Diller *et al.* [45] controlled a sub-millimeter robots by using a magnetic gradient pulling method. The resulting tumbling motion exhibited a more controllable mode without significant slippage. Bi *et al.* [19] presented a microrobot that is controlled

by an external magnetic field. A permanent magnet was rotated beneath the workspace and regulated a microrobot to tumble and travel through a narrow channel. Alternatively, when a rotating magnetic field is applied to a helical robot submersed in a fluid, it will move in the direction of the helical axis. Bozuyuk *et al.* [22] 3D printed a double-helical microswimmer made from a magnetic polymer composite. The motion of this robot was controlled using light in order to perform drug payload carry and release tasks.

In addition, robots can swim in a liquid medium by producing a wavy motion of their bodies. Zhang and Diller [176] designed a flexible magnetic sheet, which can swim in a liquid. Using the same technique, one can also generate crawling motion on dry surfaces. Accordingly, Hu *et al.* [71] developed a non-uniform magnetized soft millimeter-scale robot and controlled it to move on a solid surface, swim inside and on the surface of a liquid, and crawl in a channel.

Kashki et al, introduced an inertially actuated robot that can produce a type of wobbling gate, which they called "pivot walking" [87]. This type of locomotion is based on using two spinners that cause the robot to successively pivot and spin about two distinct points. It turns out, one can generate similar motions using magnetic instead of inertial actuation. As a matter of fact, using magnetic actuation makes it possible to significantly reduce the size of pivot walkers, because the burden of having on-board actuators is now moved elsewhere. This type of magnetically actuated locomotion was used by Dong and Sitti [48] to regulate the motion of a microgripper. They controlled the gripper to reach and grip an object, then move it and release it at a desired destination. In a recent study [6], we proposed a millirobot, with two permanent magnets mounted at each end of a rectangular shaped body. This millirobot can perform several locomotion modes, including pivot walking. The object was controlled in an open loop control mode, where sequential clockwise and counter-clockwise magnetically generated forces were applied to generate locomotion. We discovered that the most controllable motion among these modes was pivot walking. Closed-loop position control of this robot is a challenging task. In this study, we investigate the kinematic model of the pivot walking mode. We propose two control algorithms that track time-dependent

desired trajectories based on robot kinematics. The first scheme is a proportional-geometric controller, which moves the center of the robot to a desired location at that time instant. The controller performs this task by taking successive steps alternating between the two pivot points. During each step, based on the distances between the pivot points and the desired position, one of the pivot points is chosen. Then, the robot swings about the chosen pivot with a velocity that is proportional to the distance between the center of the robot and the desired point. The second control scheme is based on a gradient descent optimization technique, where the control problem is expressed as an optimization problem. The control inputs are the parameters that need to optimized to reduce the error between the center of the robot and the desired trajectory. These control algorithms enable the robot to walk and track an arbitrary trajectory.

This paper is organized as follows. In Section II, a kinematic model of the pivot walker robot is derived. Section III presents the locomotion analysis. Two control algorithms are presented in Section IV. We carry out numerical simulation runs to validate the performance of the proposed controllers in Section V, and the conclusion is presented in Section VI.

2.2. Kinematic model

The robot is composed of a rigid link with a permanent magnet embedded in the center as shown in Fig. 2.1. This robot is capable of forming a pivot point at the two ends by manipulating the surrounding magnetic field [6]. As shown in Fig. 2.2, the pivot points are labeled as A and B. Magnetic robots are influenced by the presence of an external magnetic field $\mathbf{B}$ both in terms of torque and magnetic force. The induced magnetic torque will rotate and align the robot's permanent magnetic $\mathbf{M}$ with the external magnetic field. The applied torque on the robot can be expressed as follows:

$$\tau = \mathbf{M} \times \mathbf{B} \tag{2.1}$$

where τ is the induced magnetic torque vector.

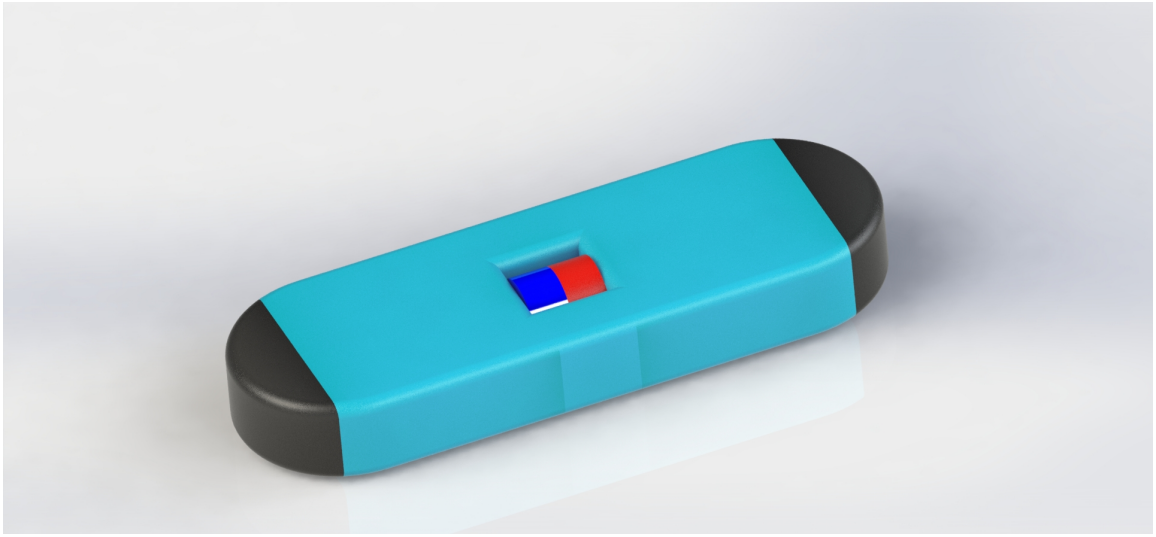

Figure 2.1. Pivot walking robot.

Derivation of kinematics of the pivot walker is based on the assumption that the robot is constructed as a rigid body. Here, we follow the same procedure to derive the kinematic model as in [5, 7–9]. First, we used two reference frames; the global reference frame and the local reference frame to identify the robot position on the plane as shown in Fig. 2.2. The axes X_I and Y_I define an arbitrary inertial basis in the global reference frame. To specify the position of the robot, a point C on the center of the robot's chassis is chosen as its positional reference. The basis x_C and y_C defines the robot's local reference frame that passes through C on the robot's body. The position of C in the global reference frame is specified by coordinates x and y, and the angle between the two frames is given by θ. The robot pose is then fully determined by the three state variables x, y, and θ. A 3×1-vector q_I is defined to describe the robot state in the global frame and q_R in the local frame.

$$q = \begin{bmatrix} x & y & \theta \end{bmatrix}^T \tag{2.2}$$

The transformation between the robot frame and inertial frame is described as follows:

$$\dot{q}_R = R(\theta)\dot{q}_I \tag{2.3}$$

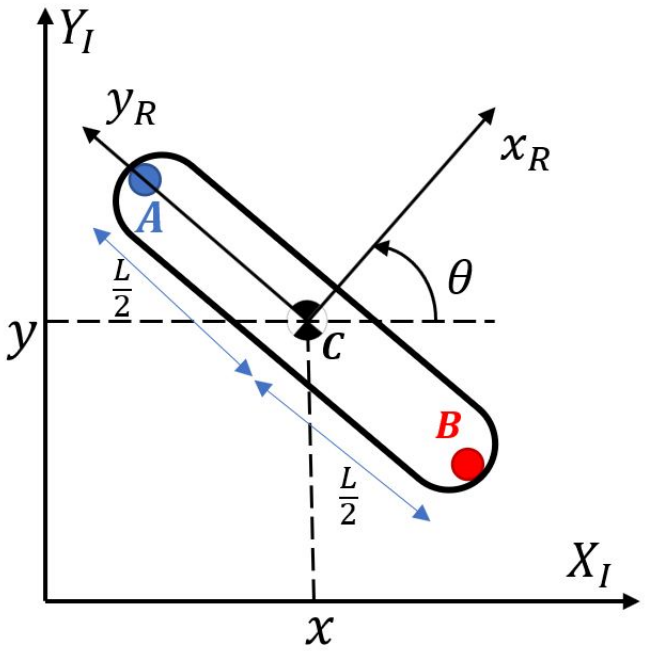

Figure 2.2. The global reference frame and the robot local reference frame.

where, $R(\theta)$ is the rotation matrix. Based on Eq. 2.3 the kinematics of the robot in the inertial frame can be written as follows:

$$R(\theta) = \begin{bmatrix} \cos\theta & \sin\theta & 0 \\ -\sin\theta & \cos\theta & 0 \\ 0 & 0 & 1 \end{bmatrix} \tag{2.4}$$

where, $R(\theta)$ is the rotation matrix. Based on Eq. 2.3 the kinematics of the robot in the inertial frame can be written as follows:

$$\dot{q}_I = R(\theta)^{-1}\dot{q}_R \tag{2.5}$$

Thus, we have to obtain the kinematics in the robot frame. But before presenting the derivation of the kinematic model of the pivot walker, few assumptions will be presented.

The robot can only rotate about the pivots without slippage. Figure 2.3 describes how the robot is rotating about each pivot, wherein Fig. 2.3a, the active pivot is A, therefore the point is fixed and the robot is rotating about it. While point B is fixed when pivot B is active as shown in Fig. 2.3b. Successive switching between the two pivots will enable the robot to generate locomotion.

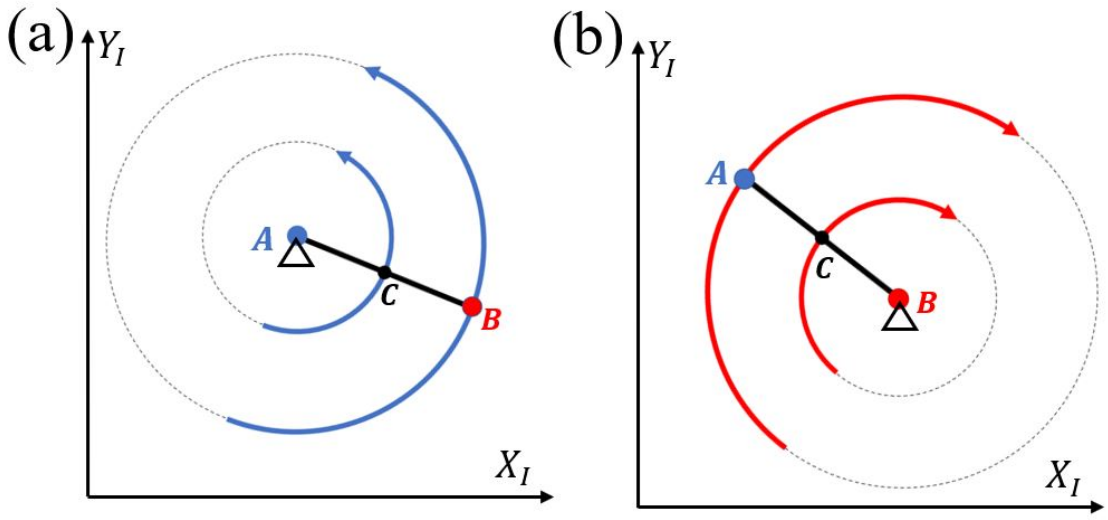

Figure 2.3. The global reference frame and the robot local reference frame.

Since the robot has two pivots, it has two kinematic models, one for each pivot. The derivation of the kinematic model with respect to pivot A is as follows: The velocity of the robot's center in the robot frame v_C^R is defined using the relative velocity between points C and A as follows:

$$v_C^R = v_A^R + \bar{\omega} \times r_{C/A}^R \tag{2.6}$$

where, v_A is equal to zero since the point A is fixed pivot, $\bar{\omega}$ is the robot angular velocity about z-axis, and $r_{C/A}^R$ is the position vector between point C and A. Then, $\bar{\omega}$ and $r_{C/A}^R$ are

defined as follows:

$$\bar{\omega} = \begin{bmatrix} 0 \\ 0 \\ \omega \end{bmatrix} \tag{2.7}$$

$$r^R_{C/A} = \begin{bmatrix} 0 \\ -\frac{L}{2} \\ 0 \end{bmatrix} \tag{2.8}$$

where, ω is the angular velocity about the $z-axis$ and L is the robot length. So, v^R_C simplifies to

$$v^R_C = \begin{bmatrix} \frac{L\omega}{2} \\ 0 \\ 0 \end{bmatrix} \tag{2.9}$$

Now, using Eq. 2.5, the robot velocity in the inertial frame v^I_C can be obtained as follows:

$$v^I_C = \begin{bmatrix} \frac{L}{2}\omega\cos(\theta) \\ \frac{L}{2}\omega\sin(\theta) \\ 0 \end{bmatrix} \tag{2.10}$$

Similarly, for pivot B, Eqs. 2.6 - 2.10 are used to obtain the robot velocity in the inertial frame v^I_C. Where the relative velocity between the points C and B is defined as follows

$$v^R_C = v^R_B + \bar{\omega} \times r^R_{C/B} \tag{2.11}$$

where, v_B is equal to zero since the point B is fixed pivot and $r_{C/B}$ is the position vector between the points C and B. Then, $r_{C/B}$ is defined as follows:

$$r^R_{C/B} = \begin{bmatrix} 0 \\ \frac{L}{2} \\ 0 \end{bmatrix} \tag{2.12}$$

Therefore, the robot velocity in the inertial frame v^I_C is described as follows:

$$v^I_C = \begin{bmatrix} -\frac{L}{2}\omega\cos(\theta) \\ -\frac{L}{2}\omega\sin(\theta) \\ 0 \end{bmatrix} \tag{2.13}$$

The pivot walker kinematic model can be summarized as follows:

$$\dot{q}_I = \begin{cases} \left.\begin{array}{c} \dot{x} = \frac{L}{2}\omega\cos(\theta) \\ \dot{y} = \frac{L}{2}\omega\sin(\theta) \\ \dot{\theta} = \omega \end{array}\right\} & \text{for pivot A} \\ \\ \left.\begin{array}{c} \dot{x} = -\frac{L}{2}\omega\cos(\theta) \\ \dot{y} = -\frac{L}{2}\omega\sin(\theta) \\ \dot{\theta} = \omega \end{array}\right\} & \text{for pivot B} \end{cases} \tag{2.14}$$

where $\dot{x}$ and $\dot{y}$ are the robot linear velocities, $\dot{\theta}$ is the robot angular velocity. As can be seen, the kinematic model is a hybrid model that contains continuous-time functions and discrete events (e.g the switching between the two models). Hybrid systems [74] are harder

to control. As we have the control over the switching between the two pivots, the switching can be modeled as input to the kinematic model that results in combining the two kinematic models into single model as presented:

$$\dot{q}_I = \begin{bmatrix} \frac{L}{2}\sigma\omega\cos(\theta) \\ \frac{L}{2}\sigma\omega\sin(\theta) \\ \omega \end{bmatrix} \tag{2.15}$$

where, σ is the switching control input between the models, If $\sigma = 1$, the pivot A is active, whereas $\sigma = -1$, means that B is the active pivot. Value of the parameter σ is constrained by either 1 or -1 depending on the desired active pivot.

Finally, the positions of pivots A and B are obtained using vector projection. Where pivot A position is calculated as follows

$$x_A = x - \frac{L}{2}\sin\theta \tag{2.16}$$

$$y_A = y + \frac{L}{2}\cos\theta \tag{2.17}$$

similarly, the position of pivot B is

$$x_B = x + \frac{L}{2}\sin\theta \tag{2.18}$$

$$y_B = y - \frac{L}{2}\cos\theta \tag{2.19}$$

2.3. Locomotion Analysis

The locomotion of the robot is composed of successive steps. Each step can be described as a motion about a pivot point. The location of the pivot point alternates between the two contact points with the ground surface. Fig. 2.4 schematically shows a two-step progression of this type of locomotion. During the first step, pivot A is active and no motion occurs

there. Meanwhile, pivot B is free to move with the robot body. Once the main link rotates into the desired angle the active pivot is switched to pivot B and now pivot A is free to move with the main link. This process is repeated to generate forward locomotion.

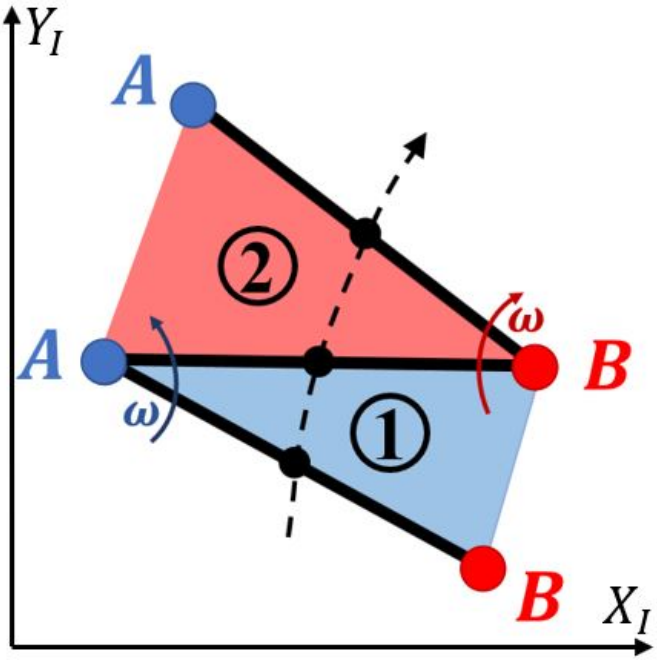

Figure 2.4. A two step angular progression in pivot walking.

In general, walking consists of successive steps. In order to analyze the locomotion of the robot, we defined a set of gait parameters. The sweep angle θ_s is defined as the angle between two successive steps. The number of switches between the two pivots is defined as the number of steps N_s. The sweep angle has a significant impact on the motion, the number of steps, and the travel distance. In order to demonstrate the effect of the sweep angle, a locomotion algorithm is designed to control the robot to walk along a straight line. This locomotion algorithm was designed such that the robot starts from initial position, then takes a step with half of the desired sweep angle. Subsequently, the pivot is switched and followed by a step with a full desired sweep angle. Finally, the pivot is switched again to perform the next step on the other pivot. The straight-line locomotion is shown in Algorithm 1.

Algorithm 1: Straight walking locomotion

$N_s = 0$; $\theta_0 = 0$;
$\omega = \omega_0$; $\sigma = 1$;
while $y_d - y > 0$ **do**
  if $N_s = 1$ **then**
    $\theta_s = \frac{\theta_d}{2}$;
  else
    $\theta_s = \theta_d$;
  end
  if $|\theta - \theta_0| = \theta_s$ **then**
    $\sigma = -\sigma$;
    $\omega = -\omega$;
    $\theta_0 = \theta$;
  end
  q = robotKinemaitc (q, σ, ω);
  $N_s = N_s + 1$;
end

Figure 2.5 shows different robot trajectories for different sweep angles in the range of 1° to 360°. Where the purple dashed line represents the straight path, the center of the robot trajectory is shown as a thick black line. The blue and red lines represent the pivots A and B respectively. Blue and red areas indicate that the robot rotates about pivots A and B respectively. The change in color in these areas represents the number of switches between the two pivots, hence the number of steps. As can be seen from Fig. 2.5, the sweep angle has a significant effect on the number of steps. Whereas, the number of steps is very large for small angles and gradually reduces for increasing values of the sweep angle. Another observation is that the robot path is almost a straight line at smaller angles, while curved paths appear at larger sweep angles. A full parametric analysis is conducted to see the effect of the sweep angle on the number of steps and travel distance.

Figure 2.6 shows the number of steps as a function of the sweep angle for a travel distance of 6 cm. At lower sweep angles, the number of steps is very large with a singularity at $\theta_s = 0$. Increasing the sweep angle results in fewer number of steps, As can be seen in Fig.2.5, after about 200°, the number of steps starts increasing as the contribution of the steps to the

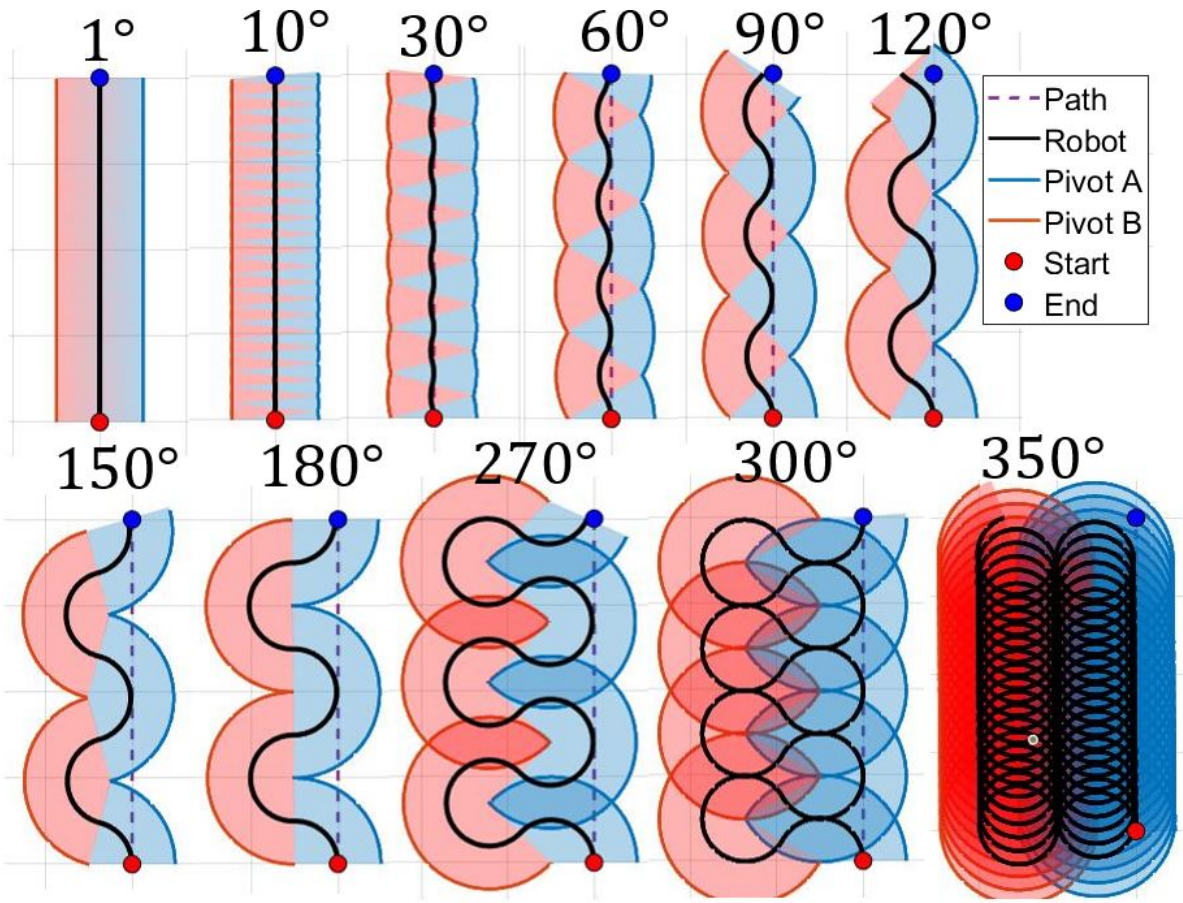

Figure 2.5. Different robot paths for different sweep angles. the robot length is 10 mm and the desired path length is 40 mm.

forward motion diminish. At $\theta_s = 360°$, there is another singularity since the robot rotates around its own central axis. Also, higher number of steps results in longer completion times. Figure 2.7 depicts the robot's travel distance as a function of the sweep angle. Ideally, the travel distance is equal to the path length at lower sweep angles. But increasing the sweep angle results in drifts from the path length leading to higher travel distances, and therefore, to longer task completion times.

These two parametric analysis results can be used in designing and optimizing control algorithms for the pivot walker robot. For example, a small sweep angle can be used to perform accurate tasks, but small sweep angles result in higher number of steps. Therefore,

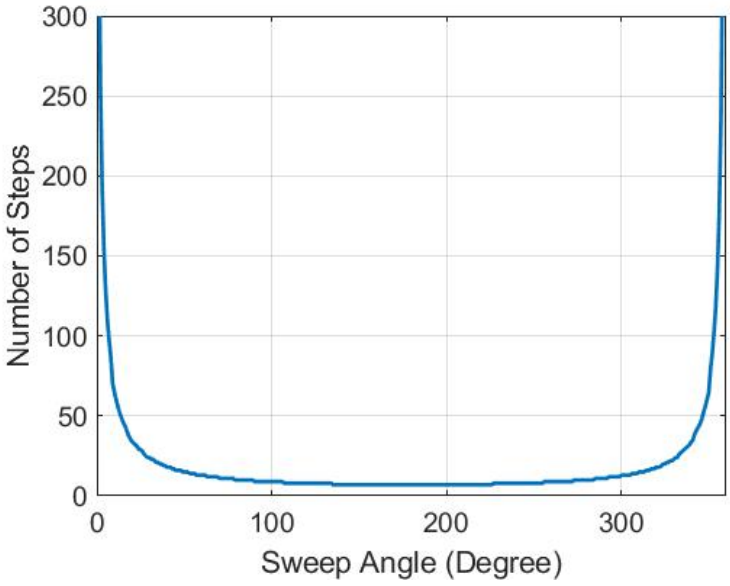

Figure 2.6. Variation of a number of steps to travel 6 cm as a function of sweep angle.

the process becomes a trade-off between accuracy and task completion time.

2.4. Control Design

Based on the kinematic model presented in Eq. 2.15, the robot motion can be governed using two control inputs σ and ω. The input σ determines the active pivot that the robot rotates about and ω defines how fast the robot will rotate about the active pivot. In this section, we present a control algorithm for pivot walking robots to track an arbitrary trajectory. The goal of this controller is to minimize the error e between the robot center (x, y) and the desired trajectory (x_d, y_d). Figure 2.8 shows the robot and the desired trajectory. The challenge in designing a control algorithm for such systems is how to handle the switching between the two kinematic models. There are two ways to solve this problem. First, preplan the motion using algorithms that take into consideration the robot kinematics (e.g humanoid and bipedal robots). Second, design an algorithm that can solve the planning and control problem, simultaneously. In this section, we will focus on the second approach, where, two algorithms are proposed to track the desired trajectory without pre-planning the motion.

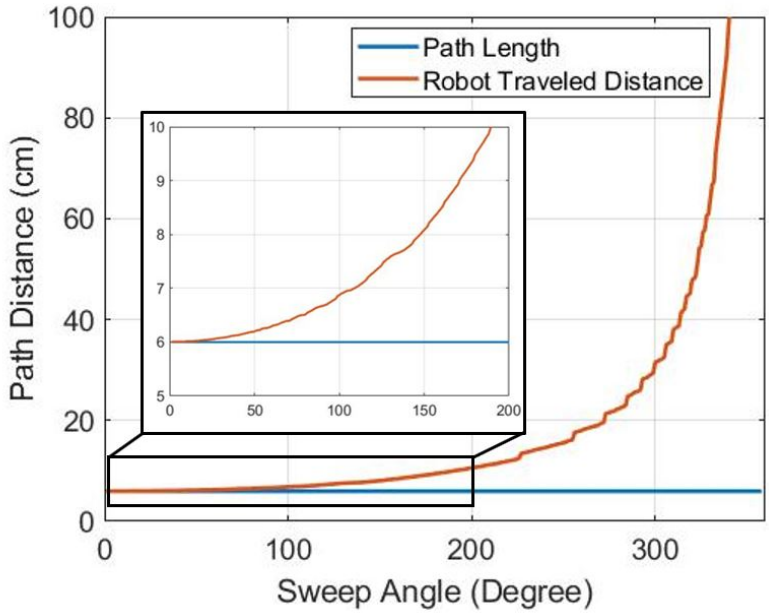

Figure 2.7. Variation of robot traveled distance as function of sweep angle.

2.4.1. Geometry based controller

As discussed earlier, the challenge in controlling a walking robots is how to design the control algorithm that switches between the pivots to minimize the error. We propose to use the distance between the two pivots and the desired path, and based on the distance the robot uses the nearest pivot as the active pivot and rotates about it. The idea behind this algorithm is that the robot rotates about the nearest pivot (e.g. A) to the trajectory until the other pivot (e.g. B) becomes the nearest one. Then, the pivot is switched to B until A becomes the nearest pivot to the trajectory and so on. Consequently, the algorithm is formulated. Expressions for the distances between the pivots and the desired trajectory are shown in Fig. 2.8, and can be obtained as follows:

$$d_{Ad} = \sqrt{(x_A - x_d)^2 + (y_A - y_d)^2)} \tag{2.20}$$

$$d_{Bd} = \sqrt{(x_B - x_d)^2 + (y_B - y_d)^2)} \tag{2.21}$$

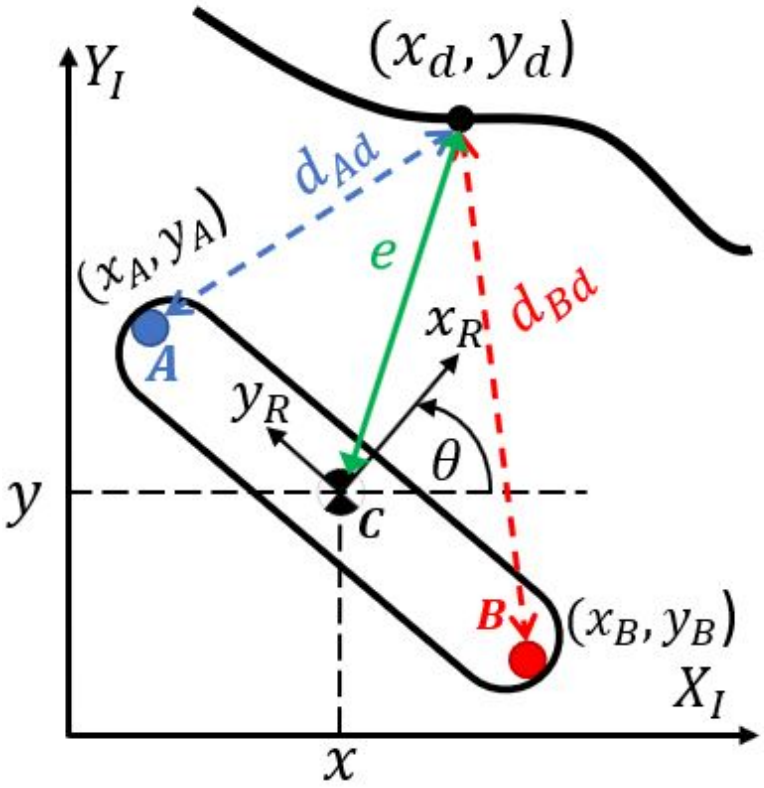

Figure 2.8. Control problem description.

Then, the active pivot is:

$$\sigma = sign(d_{Bd} - d_{Ad}) \tag{2.22}$$

where $\sigma = 1$ if d_{Bd} is greater than d_{Ad} and $\sigma = -1$ if d_{Bd} is less than d_{Ad}.

After selecting the active pivot that minimizes the error, a proportional controller for the angular velocity ω is formulated as follows:

$$\omega = k\,\sigma\,e_n \tag{2.23}$$

where k is a positive gain, and e_n is the norm of error between the robot center and the desired trajectory given by:

$$e_n = \sqrt{(x - x_d)^2 + (y - y_d)^2)} \tag{2.24}$$

The sign of σ plays an important role in this control law (Eq.2.23) to specify in what direction the robot should rotate. Finally, this control algorithm integrated with the sweep angle concept and shown in Algorithm 2. Where the switching between the two pivots is constrained by completing the sweep angle.

Algorithm 2: Geometry based controller

```
Initialization ;
q = q0;
e_n = sqrt((x - x_d)^2 + (y - y_d)^2) ;
d_Ad = sqrt((x_A - x_d)^2 + (y_A - y_d)^2) ;
d_Bd = sqrt((x_B - x_d)^2 + (y_B - y_d)^2) ;
σ = sign(d_Bd - d_Ad) ;
ω = σ e_n ;
while t < t_f do
    if θ - θ_0 = θ_s then
        θ_0 = θ ;
        d_Ad = sqrt((x_A - x_d)^2 + (y_A - y_d)^2) ;
        d_Bd = sqrt((x_B - x_d)^2 + (y_B - y_d)^2) ;
        σ = sign(d_Bd - d_Ad) ;
    end
    e_n = sqrt((x - x_d)^2 + (y - y_d)^2) ;
    ω = k σ e_n ;
    q = robotKinemaitc (q, σ, ω);
    t = t + Δt;
end
```

2.4.2. Optimization based controller

In controls theory, the control law's purpose is to minimize the error between the robot and the desired states. In other words, the control problem is an optimization problem with

the following cost function J.

$$J = \frac{1}{2}(q - q_d)^2 \tag{2.25}$$

and in more details,

$$J = \frac{1}{2}((x - x_d)^2 + (y - y_d)^2 + (\theta - \theta_d)^2)) \tag{2.26}$$

Our goal here is to minimize the cost function, by optimizing the control inputs σ and ω. Using the kinematic model (Eq. 2.15), the sensitivity of the cost function with respect to control inputs is obtained using the chain rule. This control algorithm has a similar structure to a neural network, but it is based on the kinematic network. This network consists of several layers; the first layer is the input nodes and the last layer is the robot position and orientation. The intermediate layers represent the kinematic connection between the input and the output. Finally, the back-propagation depends on the same concept of the sensitivity of the objective function with respect to control inputs.

The derivation of the proposed control algorithm is presented next. The sensitivity of the cost function with respect to the angular velocity $\frac{\partial J}{\partial \omega}$ is derived as:

$$\frac{\partial J}{\partial \omega} = \frac{\partial J}{\partial x}\frac{\partial x}{\partial \omega} + \frac{\partial J}{\partial x}\frac{\partial x}{\partial \theta}\frac{\partial \theta}{\partial \omega} + \frac{\partial J}{\partial y}\frac{\partial y}{\partial \omega} + \frac{\partial J}{\partial y}\frac{\partial y}{\partial \theta}\frac{\partial \theta}{\partial \omega} + \frac{\partial J}{\partial \theta}\frac{\partial \theta}{\partial \omega} \tag{2.27}$$

where the partial derivatives are obtained as follows

$$\begin{aligned}
&\frac{\partial J}{\partial x} = x - x_d && , \frac{\partial J}{\partial y} = y - y_d && , \frac{\partial J}{\partial \theta} = \theta - \theta_d \\
&\frac{\partial x}{\partial \omega} = \sigma \cos\theta && , \frac{\partial y}{\partial \omega} = \sigma \sin\theta && , \frac{\partial \theta}{\partial \omega} = 1 \\
&\frac{\partial x}{\partial \theta} = -\sigma\omega \sin\theta && , \frac{\partial y}{\partial \theta} = \sigma\omega \cos\theta &&
\end{aligned} \tag{2.28}$$

Next, the sensitivity of the cost function with respect to the active pivot $\frac{\partial J}{\partial \sigma}$ becomes:

$$\frac{\partial J}{\partial \sigma} = \frac{\partial J}{\partial x}\frac{\partial x}{\partial \sigma} + \frac{\partial J}{\partial y}\frac{\partial y}{\partial \sigma} + \frac{\partial J}{\partial \theta}\frac{\partial \theta}{\partial \sigma} \tag{2.29}$$

where the partial derivatives are obtained as follows

$$\frac{\partial x}{\partial \sigma} = \omega \cos\theta \qquad , \frac{\partial y}{\partial \sigma} = \omega \sin\theta \qquad , \frac{\partial \theta}{\partial \sigma} = 0 \tag{2.30}$$

Using the gradient decent, the control laws are

$$\omega_0 = \omega_0 - \eta \frac{\partial J}{\partial \omega} \tag{2.31}$$

$$\sigma_0 = \sigma_0 - \eta \frac{\partial J}{\partial \sigma} \tag{2.32}$$

where, η is the learning rate. Then, saturation and sign functions are used to constrain the control inputs.

$$\omega = sat(\omega_0) \tag{2.33}$$

$$\sigma = sign(\sigma_0) \tag{2.34}$$

This control algorithm learns and optimizes the control inputs to minimize the cost function, which is the error in this case. Also, this algorithm has an advantage over the previous algorithm because it is able to regulate the orientation of the robot. Finally, the control algorithm integrated with the sweep angle concept and shown in Algorithm 3. Finally, we note that the switching between the two pivots is constrained by completing the sweep angle, and the gradient descent algorithm runs N iteration time to ensure convergence.

2.5. Simulation Results

We test the performance of the proposed controllers by conducting a set of simulation runs in different scenarios. In each case, we use a parametrized circular path as the desired

Algorithm 3: Optimization based controller

Initialization ;
$q = q_0$;
$\sigma = \sigma_0$;
$\omega = \omega_0$;
while $t < t_f$ **do**
  for $k \leftarrow 1$ *to* N **do**
    $q_c = q$;
    $q_c =$ robotKinemaitc (q_c, σ_0, ω_0);
    $J = \frac{1}{2}(qc - q_d)^2$;
    $\frac{\partial J}{\partial \omega} = \frac{\partial J}{\partial x}\frac{\partial x}{\partial \omega} + \frac{\partial J}{\partial x}\frac{\partial x}{\partial \theta}\frac{\partial \theta}{\partial \omega} + \frac{\partial J}{\partial y}\frac{\partial y}{\partial \omega} + \frac{\partial J}{\partial y}\frac{\partial y}{\partial \theta}\frac{\partial \theta}{\partial \omega} + \frac{\partial J}{\partial \theta}\frac{\partial \theta}{\partial \omega}$;
    $\frac{\partial J}{\partial \sigma} = \frac{\partial J}{\partial x}\frac{\partial x}{\partial \sigma} + \frac{\partial J}{\partial y}\frac{\partial y}{\partial \sigma} + \frac{\partial J}{\partial \theta}\frac{\partial \theta}{\partial \sigma}$;
    $\omega_0 = \omega_0 - \eta \frac{\partial J}{\partial \omega}$;
    $\sigma_0 = \sigma_0 - \eta \frac{\partial J}{\partial \sigma}$;
  end
  if $\theta - \theta_0 = \theta_s$ **then**
    $\theta_0 = \theta$;
    $\sigma = sign(\sigma_0)$;
    $\omega = sat(\omega_0)$;
  end
  $q =$ robotKinemaitc (q, σ, ω);
  $t = t + \Delta t$;
end

trajectory. The initial pose of the robot used in the simulation is $q_I = [0\ 0\ \frac{\pi}{2}]^T$. Also, to study the effect of the sweep angle, different tests are considered to see its effect. In tests 1 and 2, the following circular trajectory is used.

$$x_d = -4\ \sin(0.1\ t) \tag{2.35}$$

$$y_d = 4\ \cos(0.1\ t) \tag{2.36}$$

In test A, the control algorithms use a sweep angle of 1°, while 30° is used in test B.

2.5.1. Test A

In this test, a 1° sweep angle is used, therefore, the two controllers are tested in the absence of sweep angle and number of steps constraints. Figure 2.9 depicts the trajectories

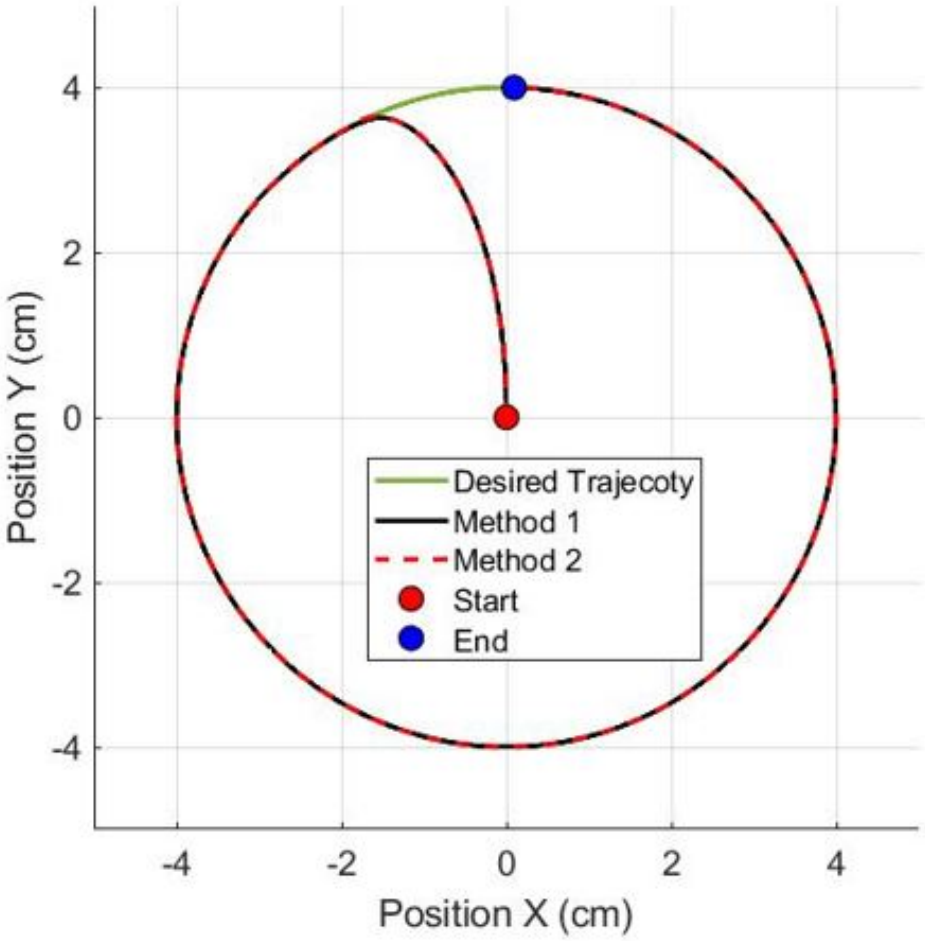

Figure 2.9. Pivot walking robot tracking with a 1° sweep angle.

of test A, where the green line represents the desired trajectory. The black and dashed red lines represent robot trajectories. Finally, the red circle shows the start position and the black circle shows the end position. As can be seen, the two methods perfectly track the desired trajectory. Figure 2.10 shows the norm of the tracking error e_n that is presented in Eq. 2.24. Where the blue and red lines represent the error of method 1 and 2 respectively. As can be seen, the tracking error is less than 0.1 cm. Therefore, the two controllers perform well, but the method 2 shows better performance. Also, in terms of the number of steps method 2 takes 2035 steps to track the desired trajectory, while 2037 steps are taken in the case of method 1.

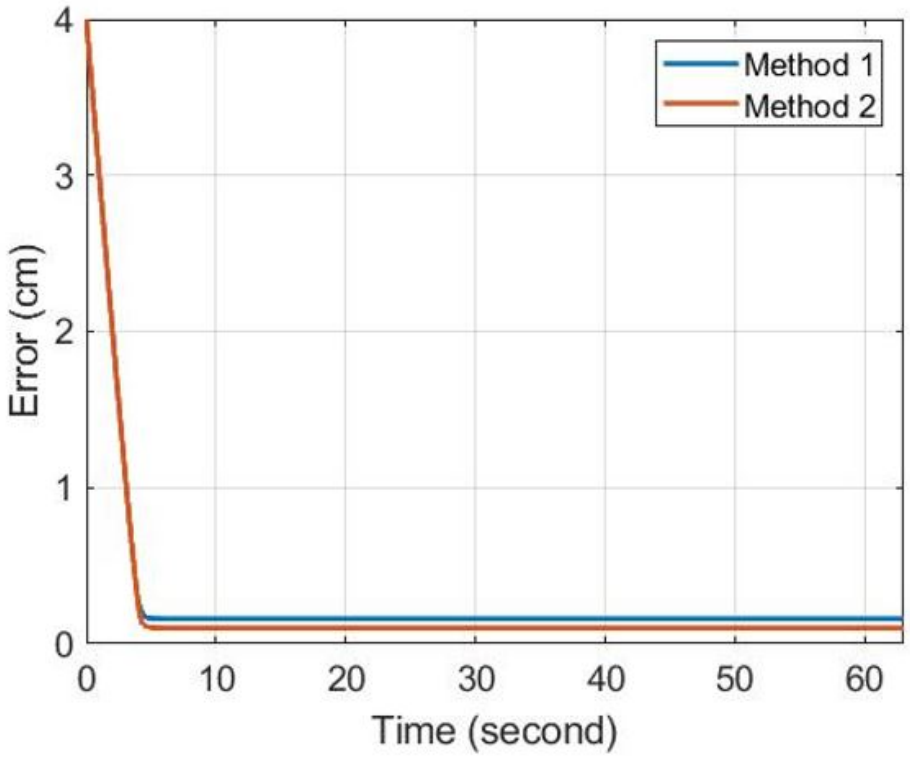

Figure 2.10. The norm of the tracking error for a 1° sweep angle.

2.5.2. Test B

In order to test the robustness of the proposed controllers, they are tested in the presence of a 30 sweep angle. Figure 2.11 depicts the trajectories of test B, where the green line represents the desired trajectory. The black and dashed red lines represent the robot trajectories using the two proposed control methods. Finally, the red and black circles show the initial and final positions respectively. As can be seen, the two methods track the desired trajectory while using a 30 sweep angle. In the presence of the sweep angle, the control inputs are updated after each step. The norm of the tracking error e_n is shown in Fig. 2.12, where the blue and red lines represent the error of methods 1 and 2, respectively. As can be seen, the tracking error is within 0.2 cm. Therefore, the two controllers perform well, but the method 2 outperforms method 1. Also, in terms of the number of steps, the two methods take a similar number of steps; for example, 64 steps are taken in method 2 and 65

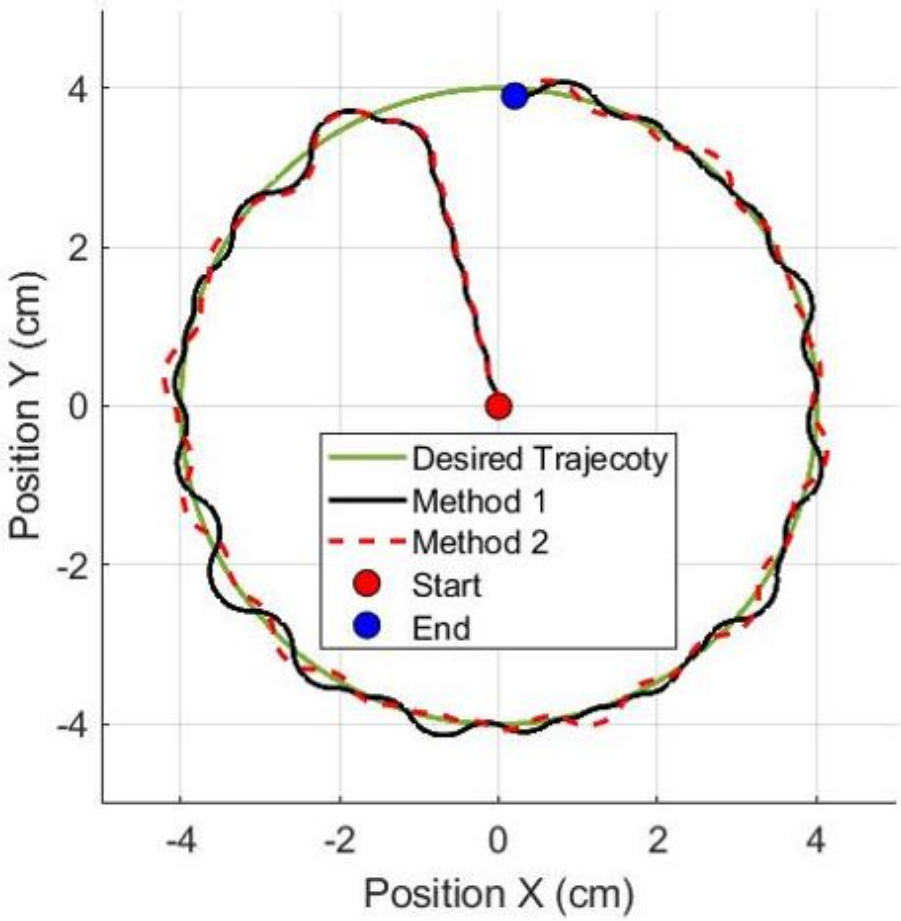

Figure 2.11. Pivot walking robot tracking with a 30° sweep angle.

steps in method 1.

Clearly, the sweep angle affects the controllers' performance because it constrains the robot kinematics. As predicted, a comparison of tests A and B shows that larger sweep angles results in fewer number of steps but the tracking error performance deteriorates.

2.6. Conclusion

In this paper, kinematic modeling and control for pivot walking millirobots are addressed. This paper proposes two control algorithms to guide the pivot walker while it follows a desired path. The first controller is a proportional-geometric based approach. In this approach, the

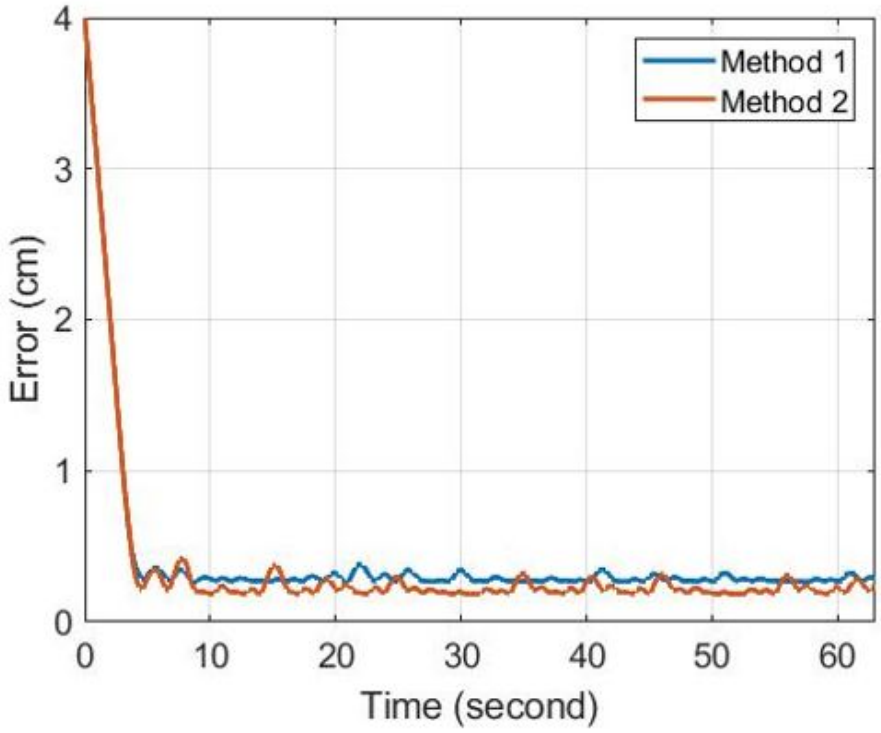

Figure 2.12. The norm of the tracking error for a 30° sweep angle.

controller activates the nearest pivot to the desired trajectory. Then, it uses a proportional controller to regulate the angular velocity about that pivot. The second method is based on optimization approach. The gradient descent algorithm is used to optimize the active pivot and the angular velocity such that the tracking error between the robot and the desired trajectory is minimized.

We conducted a parametric analysis to investigate the effect of the sweep angle on the number of steps and travel distance. We validate the performance of the tracking algorithms by using two simulation scenarios. In the first scenario, the two algorithms were tested without placing constraints on the sweep angle. While in the second scenario, the simulations were carried out by placing constraints on the sweep angle. In the two scenarios, the optimization-based controller slightly outperformed the proportional-geometric approach. It had faster convergence time, smaller tracking error, and fewer number of steps. In the future,

we plan to conduct experimental tests to verify the performance of the proposed robot and controllers in different navigation environments.

Chapter 3

Teleoperation Control Scheme for Magnetically Actuated Microrobots with Haptic Guidance

3.1. Introduction

Microscale robots, especially untethered ones, have been intensively investigated due to the many possible applications: micro-manipulation, micro-fabrication, drug delivery, tissue manipulation, in situ sensing, cell therapy and in vivo diagnostics [56]. For example, in biomedical applications, microrobots can act as co-robots that directly work on human patients, alongside healthcare providers, performing critical medical procedures. Such ideas have deep roots in popular culture and may even be considered the final frontier of medical microrobotics [117]. While most of the microrobots presented here are based on autonomous techniques [33, 56, 91, 180], there is increasing importance in human-in-the-loop strategies. For safety, public acceptance, and responsibility [127], it is helpful to equip human operators with efficient and intuitive ways for manipulating the microrobots. One such way is haptic feedback, making it an important approach in these human-in-the-loop teleoperation schemes [145, 158].

Thus far, several haptic feedback devices have been developed to control and manipulate microrobots. Bhatti *et al.* [17] designed an intuitive haptic interface known as Atomic Force Microscopy (AFM), which estimates haptic force at the end of the tip by using geometric deformation principles. Another technique for haptic feedback is visual sensing. Pacchierotti *et al.* [126] presents a particle-filter based algorithm to track the position of a robot wirelessly while a 6-DOF haptic interface enables the operator to remotely move a microrobot to its target position. Boukhni fer and Ferreira [21] used a 1-DOF haptic feedback to employ a passivity-based approach with bilateral and robust fault tolerant control. Mohand Ousaid *et*

al. [125] investigated a modular microteleportation system that includes custom components designed to take into account passivity and transparency constraints. Mehdi Ammi and Antonie Ferreo [11] use 3-D vision with haptic rendering for manipulation and penetration of cells. Asgari *et al.* [13] offer a method to represent the mechanical properties of biological cells by considering a hybrid model of micro-nano multi particles and continuum approaches. While effective, these preliminary systems have no mechanism to estimate the ambient forces acting on micro-robots when they encounter an unknown fluid or obstacle. For this purpose, we propose the development of a master-slave system for force feedback and manipulation of micro/nano objects. The master-slave system consists of two parts: a haptic controller (master) and magnetic tweezer system (slave).

The magnetic tweezer system has six magnetic poles for releasing magnetic field fluxes to generate magnetic field gradients. By applying current to certain electromagnetic coils on the poles, different magnetic gradient fields can interact with magnetized microrobots to produce propulsion magnetic forces [31, 34, 62, 177, 178, 181]. The magnetic tweezer system requires microrobots to be magnetic only without imposing any restrictions on the structure or the rigidity [136]. Therefore, it can only affect magnetized objects, offering advantages for in-vivo environments, as the biological substances are mostly non-magnetized [16, 62]. In our previous work, this magnetic tweezer system has achieved closed-loop control for real time 3D manipulation and swarm motion [179, 180], with inputs given through a user customized control interface. However, to develop the system further for human-in-the-loop application, alternative methods to apply control inputs are necessary.

The Systems Lab at SMU has been extensively engaged in haptic interface research for more than a decade. The Pneumatic Haptic Interface (PHI) was one of the first Haptic Interfaces developed [51, 73, 78, 156]. The PHI is an exoskeleton master arm with a 7-DOF system. The exoskeleton applies the interaction forces with the virtual/real environment to the right arm of the human operator in order to render a force display. Another haptic application in development is a glove [54, 55] that enables the operator to feel ultrasound data. This system can be used to interactively explore the human body for medical diagnostics,

surgery planning, and other medical applications. Furthermore, we have a commercially available off-the-shelf haptic controller (Novint Falcon) [80] that will be used in this study.

In this chapter, we integrate a haptic device together with the magnetic tweezer system to achieve path planning of microrobots with the implementation of an artificial potential field in conjunction with a virtual grid map. We focus on the teleoperation control of the magnetically actuated microrobots and haptic rendering of the environment. The rest of this chapter is organized as follows. System setup and the introduction of master and slave subsystems are shown in section 3.2. Section 3.3 illustrates the control scheme for teleoperation. The mechanisms of the potential field and haptic controller are discussed in section 3.4. Section 3.5 elaborates the experiment analysis, and the validation and conclusion are in sections 3.6 and 3.7, respectively.

3.2. Overview of the system

The experimental setup used for microrobot teleoperation is shown in Fig. 3.1 The master device is a Novint Falcon haptic device, while the slave system is the magnetic tweezer with a magnetically actuated microrobot. The control algorithm and communications software infrastructure make use of Robotic Operating System (ROS) libraries and Matlab. This selection simplifies developing, debugging and testing stages.

The teleoperation system considered in this chapter is shown in Fig. 1. The human operator commands the microrobot slave by moving the haptic device. This motion is translated into forces that will be applied by the magnetic actuation system. Lastly, when the microrobot approaches an obstacle, the virtual interaction forces are transmitted to the Falcon haptic interface, rendering the terrain as force feedback.

3.2.1. The master device

The Novint Falcon is a haptic device, which has a 3-DOF grip connected via three parallel arms. It can also be used as a 3-DOF position input and force feedback device [80]. The Falcon library translates cartesian pose state vector to the ROS-based network using our

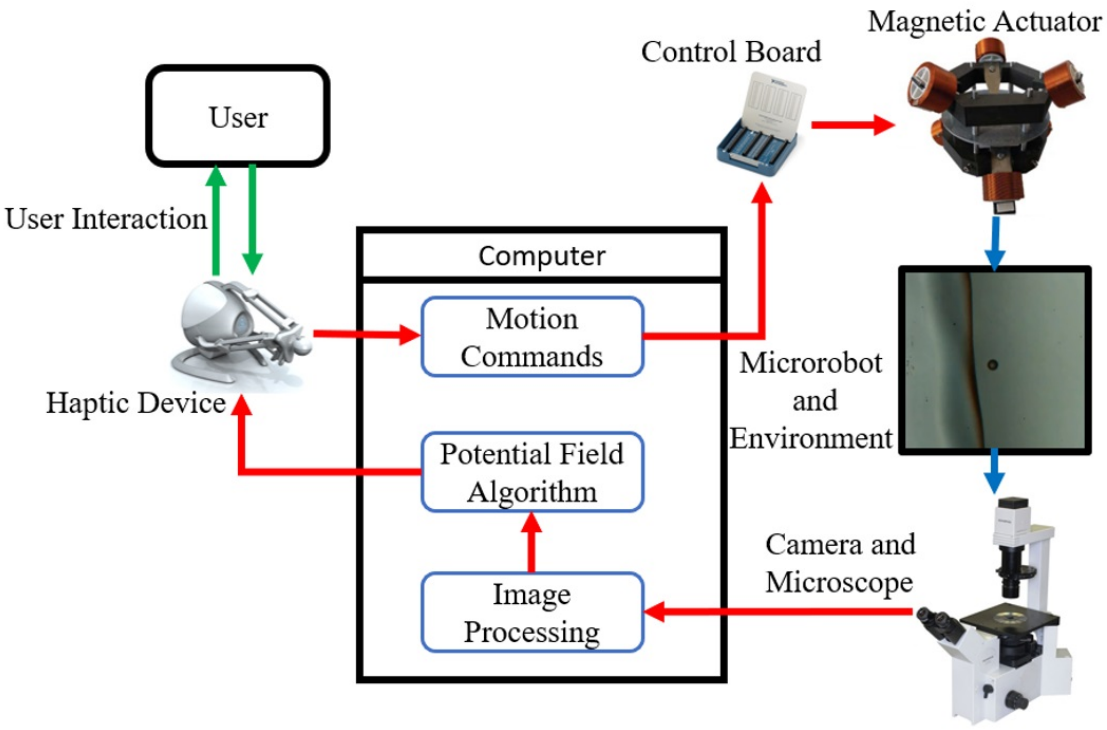

Figure 3.1. Overview of the teleoperation system: The virtual interaction forces are computed and transmitted to the human operator to guide him in performing path-following tasks. The position of the haptic device is used to compute the motion commands sent to the magnetic tweezer.

customized software.

3.2.2. The slave station

The slave station consists of magnetically actuated microrobots, the magnetic tweezer [177], and a camera with a microscope. The station will be connected to a computer for visual feedback processing and implementation of motion control. The microrobots are 10 μm coated ferromagnetic particles.

Magnetic particles are acted upon by forces that are generated by an external magnetic field ($\mathbf{B}$). In this study, the magnetic force acting on a microrobot is given by

$$\mathbf{f_{magnetic}} = (\mathbf{c}.\nabla)\mathbf{B} \tag{3.1}$$

where, $\mathbf{c}$ is the magnetic moment of the magnetic particle and $\nabla\mathbf{B}$ is the magnetic field gradient. In Stokes flow, the drag force on a microrobot undergoing translational motion can be written as,

$$\mathbf{f_{drag}} = -\zeta\,\dot{\mathbf{x}} \tag{3.2}$$

$$\zeta = 6\,\pi\,\gamma\,r \tag{3.3}$$

where, $\dot{\mathbf{x}}$ is the translational velocity of the microrobot in x, y, z-directions with radius of r, γ is viscosity of the fluid, and ζ is the spherical microrobot drag coefficient, which is commonly known as Stokes' law [172]. Figure 3.2 shows the free-body diagram of the microrobot. Thus, the equation of motion of the microrobot can be derived as follows:

$$m\ddot{\mathbf{x}} - \mathbf{f_{drag}} = \mathbf{f_{magnetic}} \tag{3.4}$$

where m is the mass of the microrobot.

3.3. Teleoperation Control Schemes

In this section, the three control strategies of teleoperation are adopted from [132] are given as:

3.3.1. Position-position

The simplest and most intuitive teleoperation scheme is the position-position control [98]). This control scheme maps the master displacement to desired slave displacement. In

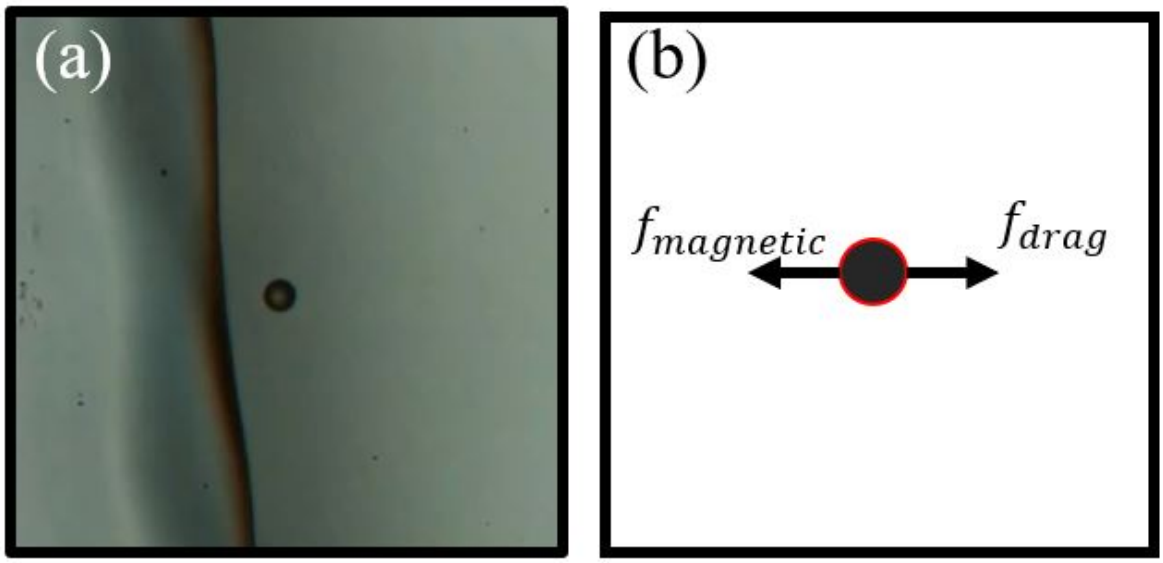

Figure 3.2. **(a)** Microrobot in a static fluid **(b)** The free-body diagram of microrobot, which illustrates the magnetic force and drag force acting on the microrobot.

order to overcome dimensional differences between master/slave workspaces, a convenient scaling criteria may be used. In our application, however, this scheme requires closed-loop position control on the slave side.

3.3.2. Position-velocity

When the slave workspace is significantly greater than the one of the master, a scaling problem may arise. One way of solving this issue is to map the master device displacement to the slave desired velocity. This mapping scheme provides more reliable performance and is appropriate for teleoperation of microrobots with infinite workspaces. Hence, similar to the position-position scheme, it requires a velocity closed-loop control on the slave side.

3.3.3. Position-force

Similar to position-velocity scheme, the position-force control scheme provides better performance when the slave workspace is greater than the master's. In this case, the forces applied to the slave are defined by the displacement of the master. Therefore, the master

displacement is translated into magnetic force using

$$\mathbf{f_{magnetic}} = K\mathbf{x_h} \tag{3.5}$$

where, $\mathbf{x_h}$ is the haptic device displacement and K is the scaling matrix. To guarantee stability of the overall system, a passivity-based approach has been adopted in the design of the control scheme. From equations (3.4) and (3.5), if $\mathbf{x_h}$ is zero, then $\mathbf{f_{magnetic}}$ is zero and the $\mathbf{f_{drag}}$ will dissipate the energy. Then, it can be easily concluded that the system is passive and therefore stable.

3.4. Haptic Guidance

3.4.1. Motion tracking

The haptic guidance problem can be addressed as a path following problem. The goal is to minimize the distance between a single microrobot and a predefined path. An algorithm based on the artificial potential field is used to generate a constrained motion in the proximity of the desired path. The proposed attractive potential field U_p is expressed as:

$$U_p(\mathbf{x}, \mathbf{x}_p) = \frac{1}{1 + e^{-\left(\left\|\mathbf{x} - \mathbf{x}_p\right\|^2 - \tau^2\right)}} \tag{3.6}$$

where, $\mathbf{x}$ and $\mathbf{x_p}$ are the microrobot and path point positions respectively, and τ is the radius of attraction. The attractive force can be easily derived as the negative gradient of the field as given in

$$\mathbf{F}_p(\mathbf{x}, \mathbf{x}_p) = -\nabla U_p(\mathbf{x}, \mathbf{x}_p) \tag{3.7}$$

The potential field is constant, as the distance between the robot and path is small, and therefore, its gradient vanishes. In addition, as the distance starts increasing the potential field increases, and its gradient changes and reaches its maximum and minimum at τ and $-\tau$ respectively. As we get further away from the desired path, the field becomes constant

again as shown in Fig. 3.3.

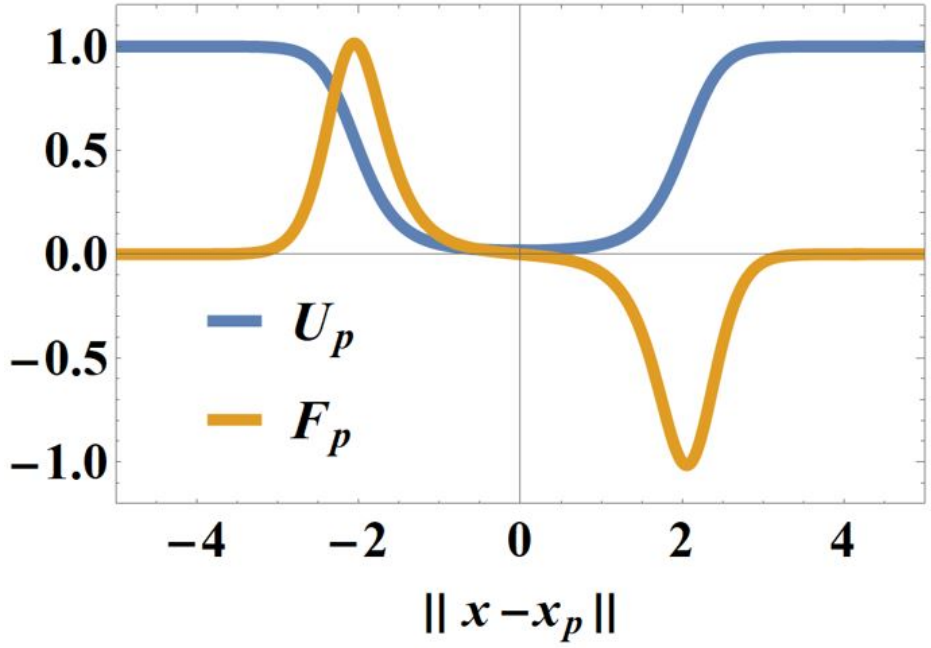

Figure 3.3. The attractive field due to the path, when $\tau = 2$

The artificial potential field around the desired path serves as a guide for the operator. As the microrobot moves along the path, the operator feels only the drag force, but when the operator drives the microrobot away from the path, the operator feels forces indicating that the microrobot is drifting. In this mode, the haptic feedback will guide and influence but not constrain the operator to move the microrobot along the desired path. The tracking accuracy relies on visual feedback and the operator. This mode combines visual and haptic feedback.

3.4.2. Haptic rendering of the environment

A virtual force can be generated by the environment to give the user a haptic feeling about the workspace. This problem can be considered as an obstacle avoidance and path planning problem. Thus, we used the artificial potential field to avoid obstacles. First, a grid is generated and superimposed on the environment. Then, each grid cell occupied by

an obstacle contributes a repulsive potential field as shown in Fig. 3.4. We define C as a set of all occupied cells. The potential field U_i is generated by a single cell $c_i \in C$ as follows:

$$U_i(\mathbf{x}, \mathbf{x}_{c_i}) = \begin{cases} \frac{1}{2}\eta \left(\frac{1}{\|\mathbf{x}-\mathbf{x}_{c_i}\|} - \frac{1}{\rho} \right) & , \|\mathbf{x} - \mathbf{x}_{c_i}\| \leq \rho \\ 0 & , \text{otherwise} \end{cases} \tag{3.8}$$

where, $\mathbf{x}$ is the robot position, $\mathbf{x}_{c_i}$ is the occupied cell position, η is a positive scaling factor, and ρ is the range of influence.

The resultant repulsive force is obtained from the negative gradient of the repulsive potential. The repulsive force exerted by each occupied cell is,

$$\mathbf{F}_i(\mathbf{x}, \mathbf{x}_{c_i}) = -\nabla U_i(\mathbf{x}, \mathbf{x}_{c_i}) \tag{3.9}$$

Using superposition, the total potential field U of all occupied cells is:

$$U = \sum_{c_i \in C} U_i(\mathbf{x}, \mathbf{x}_{c_i}) \tag{3.10}$$

and the total repulsive force exerted by the environment on the robot is given by:

$$\mathbf{F} = -\sum_{c_i \in C} \nabla U_i(\mathbf{x}, \mathbf{x}_{c_i}) \tag{3.11}$$

Subsequently, the force $\mathbf{F}$ will be transmitted to the Falcon haptic device in order to give the operator the sensation that the microrobot is approaching an obstacle. Figure 3.4 shows the obstacles and the boundaries, as well as the generated artificial potential field. As can be seen, each obstacle is surrounded by a potential field with a specific area of influence. Therefore, once the microrobot enters the field, the operator starts feeling the generated forces. As shown in Fig. 3.5, the potential field gradient around the obstacle position causes the forces to increase proportionally as the microrobot gets closer to the obstacle.

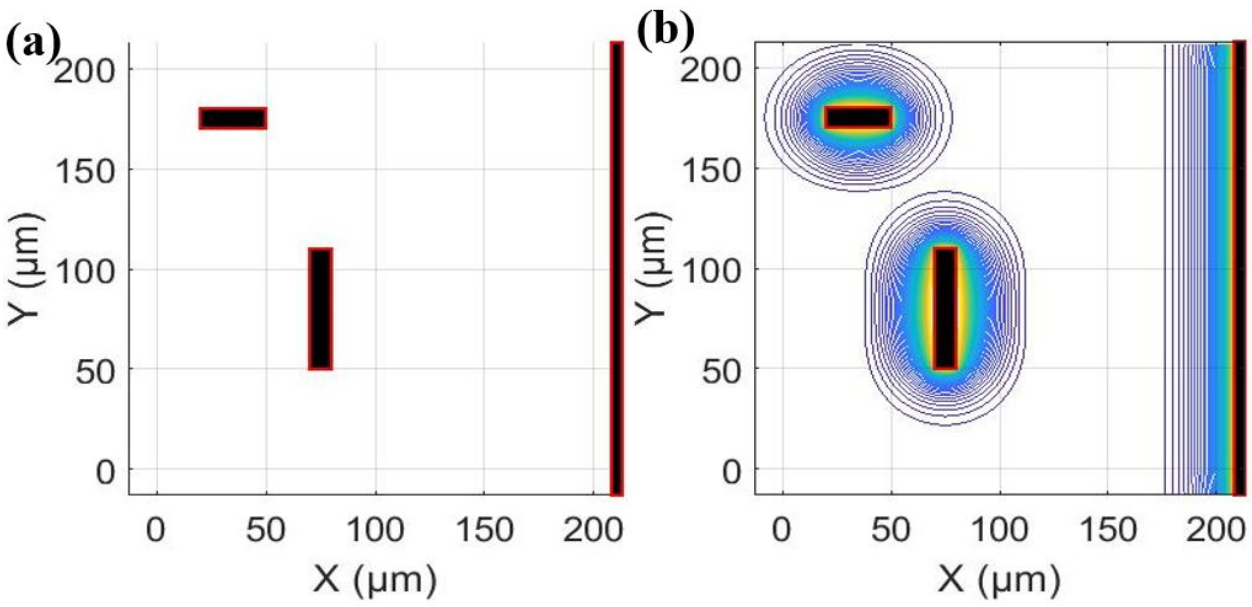

Figure 3.4. Representation of the environment. **(a)** Occupancy Grid Mapping of the environment. **(b)** The grid map with a repulsive potential field due to obstacles.

3.5. Experimental Results

The experimental results section will be divided into four parts: the first will discuss the experimental setup and signal processing; the second will discuss the proposed teleoperation scheme, where the haptic device will be used to control the microrobot; the third will discuss the proposed teleoperation scheme with the haptic guidance to track a desired path; and the forth will discuss the haptic rendering of the environment.

3.5.1. Experimental setup and signal processing

We used a magnetic tweezer system setup that was built in house. The magnetic tweezer system was mounted on an inverted microscope (Olympus IX50) with a 40X microscope lens (Fig. **??**). Each microrobot was made from ferromagnetic microbeads (Spherotech SVFM-100-4 Ferromagnetic Particle) with an average diameter of $10.6\,\mu m$. First, a 20% concentration NaCl solution was injected into a PDMS (Polydimethylsiloxane) chamber,

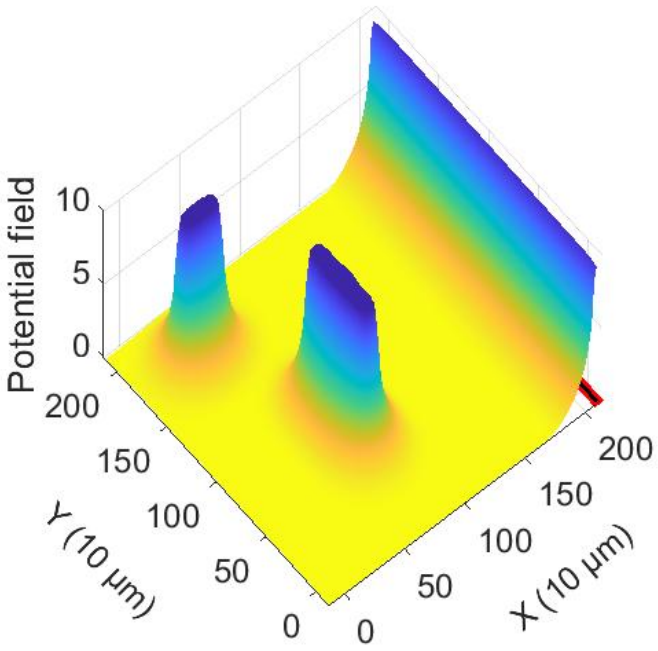

Figure 3.5. 3D presentation of the repulsive field due to the obstacles.

which then was placed in the center of the magnetic tweezer. Tween 20 was also added to the solution in order to reduce the surface contact friction. Subsequently, a population of microrobots, diluted to 5% to minimize the aggregation due to mutual magnetic attraction, was also injected into the chamber. The setup was designed such that the fluid was stationary, so there would be no fluid flow in the inner chamber except for the movement of microrobots. The control action was restricted to a single bead of robots in the center of the chamber to avoid the drag forces due to the walls. Figure 3.6a shows three microrobots and an obstacle. The positions of the microrobots and the obstacle were estimated using image processing techniques.

Image processing algorithms were used to estimate the microrobot's position from the video stream. We used a circular Hough transform technique to detect the circles that define the microrobots using phase coding [14]. The phase coding is capable of estimating the center locations and radii of the circles. Additionally, the boundary can be modeled as a line

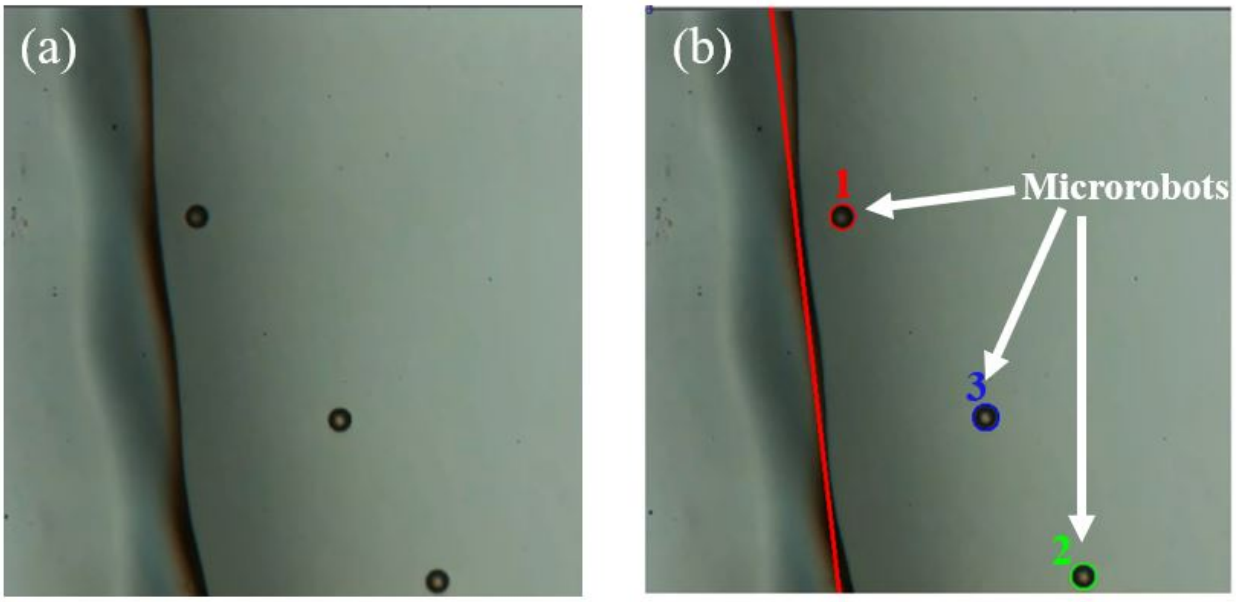

Figure 3.6. Experimental results.**(a)** A raw image of the video stream depicting three microrobots and an obstacle. **(b)** The detected microrobots and the obstacle using image processing techniques.

for visual and haptic rendering purposes. We extracted the line segments from the streamed images based on a Hough transform [115] to detect an obstacle in the environment. Figure 3.6b shows the three detected microrobots, which were labeled as 1, 2, and 3. The red line represents the obstacle.

Finally, transmission delays are negligible because data are exchanged over a local network and the robots move with relatively slow velocities.

3.5.2. Teleoperation control

An experimental test was performed using the teleoperation control scheme described in Sec. 3.3. A simple task was conducted to evaluate the proposed teleoperation method. The operator used the Falcon haptic interface as a joystick to move the microrobots. As expressed in Eq. 3.5, the displacement of the haptic device was converted to desired magnetic forces to be generated at the slave station. Figure 3.7a shows how the task was carried out, where the

microrobot was labeled as 2. The microrobot trajectory in the x - y plane is shown in Fig. 3.7b, where the red square represents the initial position, and the blue square represents the final position.

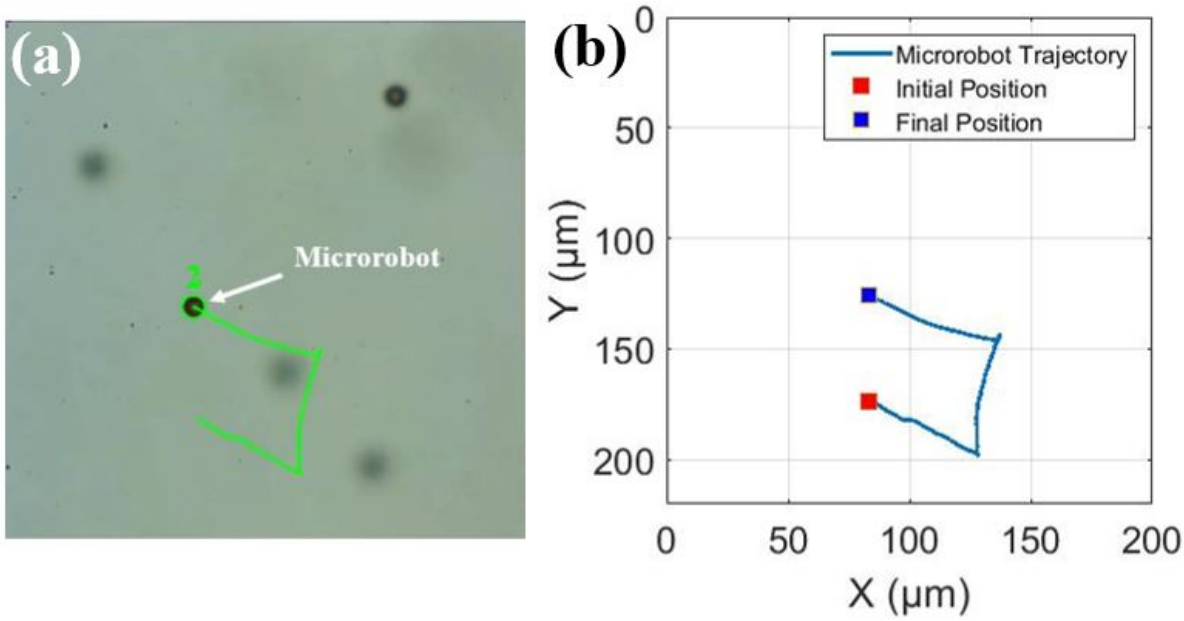

Figure 3.7. Experimental results. **(a)** A $10\,\mu m$ microrobot is controlled using the haptic interface. **(b)** The microrobot trajectory, initial, and final position are shown.

3.5.3. Motion tracking

An experiment was carried out using the teleoperation control scheme with the haptic guidance to track a desired path. In this experiment, the microrobot locations are estimated using the image processing techniques presented in Sec.3.5.1. Figure 3.8a shows the microrobot as well as the desired path. An attractive potential field was generated using the algorithm discussed in Sec.3.4.1. The field is shown in Fig. 3.8b, where the predefined path is represented as a red line encircled by the attractive potential field. In this experiment, the operator attempted to follow the path in the presence of haptic guidance, as shown in Fig. 3.9a. Figure 3.9b shows the haptic forces felt by the operator. As can be seen, when the microrobot drifted away from the path, the haptic algorithm guided the operator back

to it.

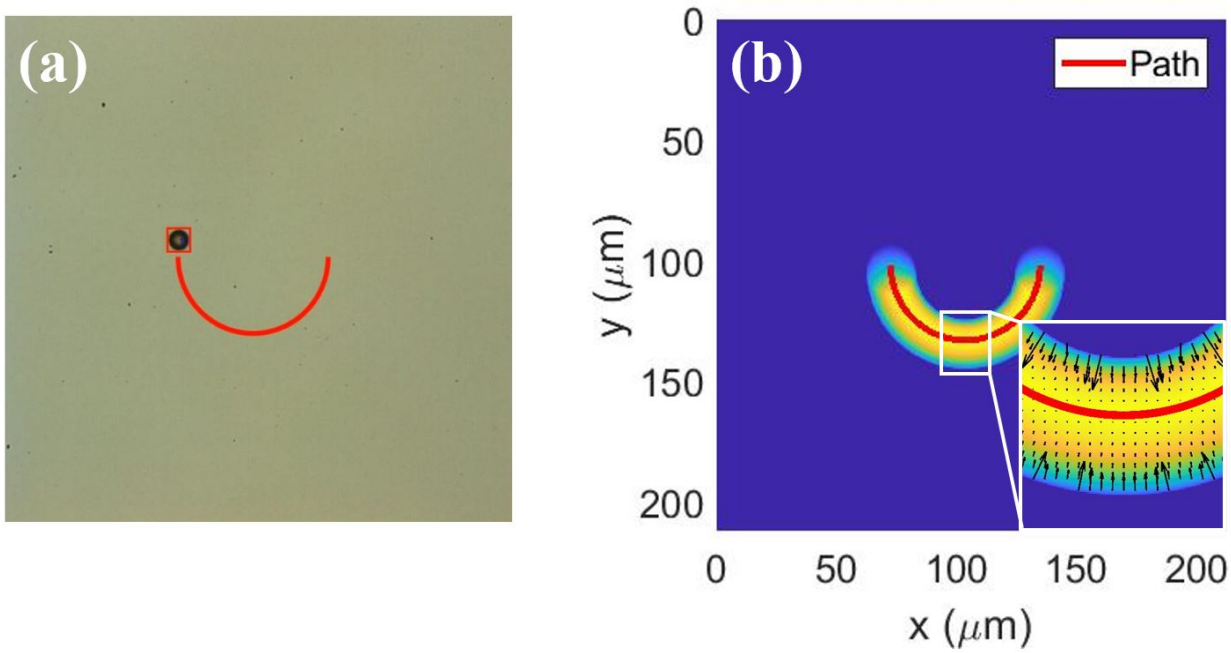

Figure 3.8. Experimental results. **(a)** A $10\,\mu m$ microrobot is controlled using the haptic interface to follow a predefined curved path. **(b)** The attractive potential field around the path.

3.5.4. Haptic rendering of the environment

In this section, an experimental test was performed using the teleoperation control scheme with haptic rendering of the environment as described in Sec. 3.4. With awareness of obstacle locations, a grid map of the environment was constructed. Figure 3.10a shows a contour representation of the repulsive field due to an obstacle. Here, the influence range of the obstacles is $10\mu m$. Since we only have one haptic interface, the operator can only feel the force acting on a single robot. Thus, in this situation, microrobot (1) is the microrobot of interest to be tracked and controlled by the operator. Additionally, Fig 3.10a shows the microrobot (1) and its trajectory as the black circle and blue line, respectively. The obstacle and its potential field are represented as a red line with contour showing the area of influence of the obstacle. As can be seen, the microrobot started from an initial location outside the

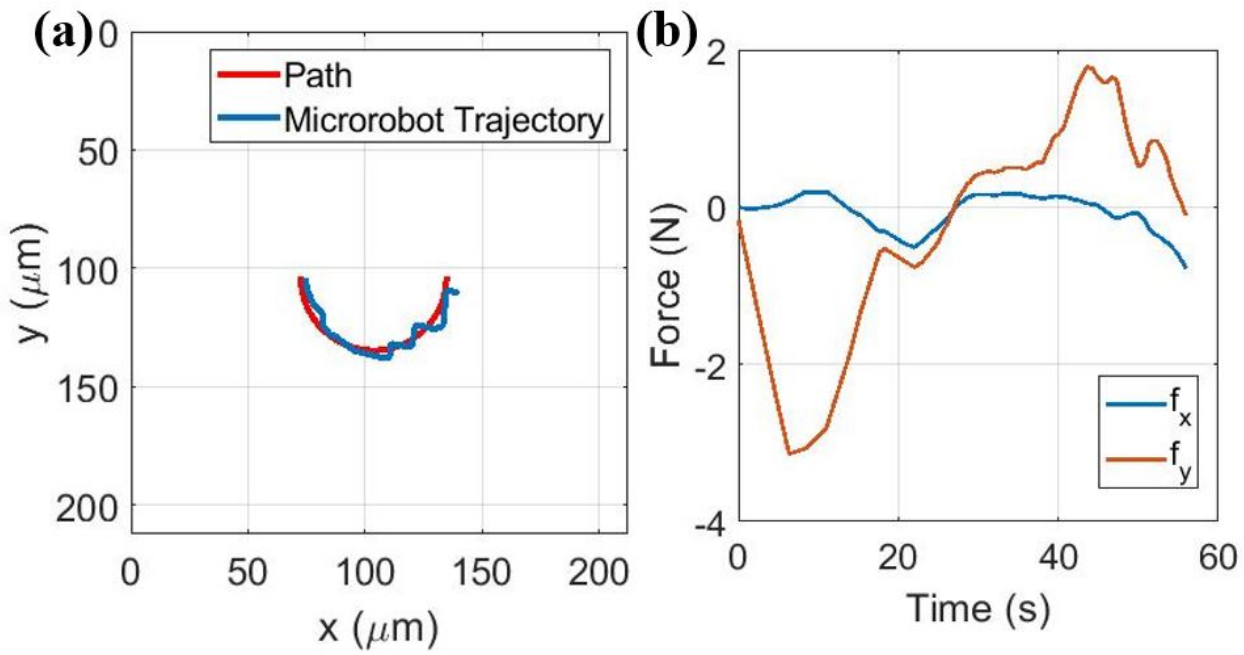

Figure 3.9. Experimental results. **(a)** A predefined curved path and a 10 μm microrobot trajectories. **(b)** The haptic forces, which displaced to operator.

influence region of the obstacle potential field. As the operator move the microrobot in the direction of the obstacle, the microrobot entered the influence region, and the operator started to feel the forces from the haptic device as shown in Fig. 3.10b. The blue and red lines represent the forces in x and y directions, respectively. The black lines represent the upper and lower force limits of the Falcon haptic device. Also, as can be seen from Fig. 3.10, the forces are proportional to the distance between the microrobot and the obstacle. As the microrobot approaches the obstacle, the operator felt stronger forces. Finally, as the operator moved the microrobot away from the obstacle, smaller forces were experienced until the microrobot escaped the influence region of the obstacle.

3.6. Validation

For benchmarking purposes, two groups of experiments were carried out. In the first group, we attempted to move a single microrobot along a predefined path without haptic

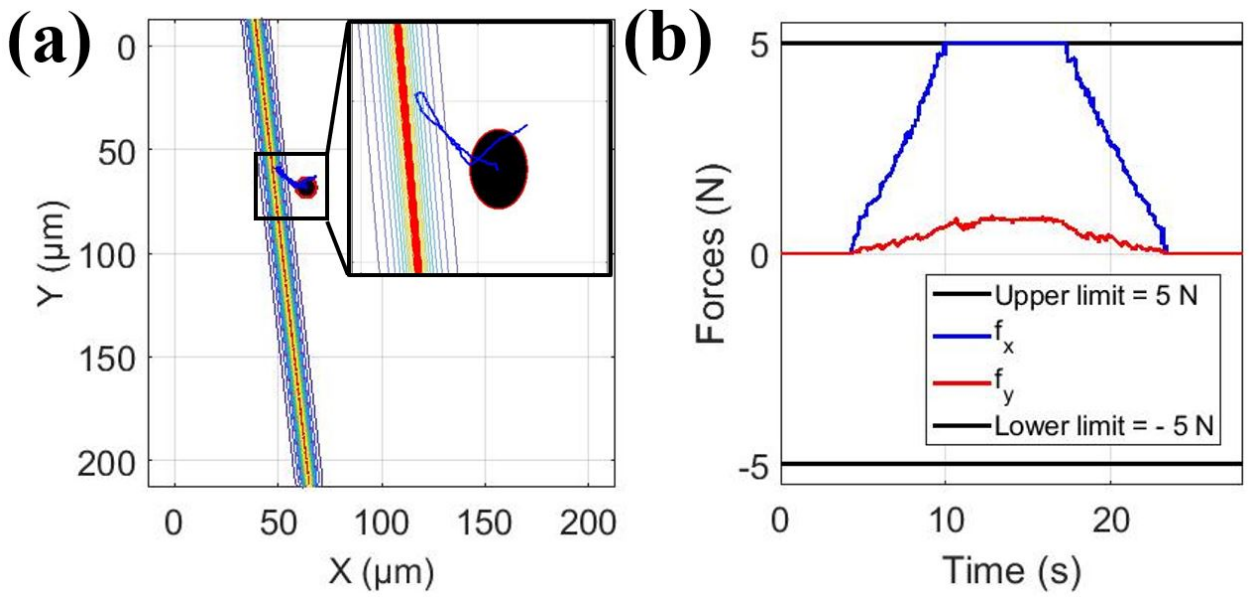

Figure 3.10. Experimental results. **(a)** Position of the microrobot with respect to the obstacle. **(b)** The forces in x and y directions that are obtained using the potential field algorithm.

guidance. Then, this task was repeated with haptic guidance. At each trial, we were able to follow the displayed path with minimal error. Two criteria were selected to evaluate the benchmark process: average path error and completion time. The average path error was calculated as the mean of the perpendicular distance between the microrobot position and the path. The completion time was the time period between the time instants the operator started tracking the path and when the end of path was reached.

The data obtained from these experiments showed significant improvement when adding the haptic feedback in the system. As can be seen in Fig. 3.11, the average path error was reduced by a factor of 3, accompanied by a slight decrease in the completion time. The slight improvement of the completion time was due to the simplicity of the task.

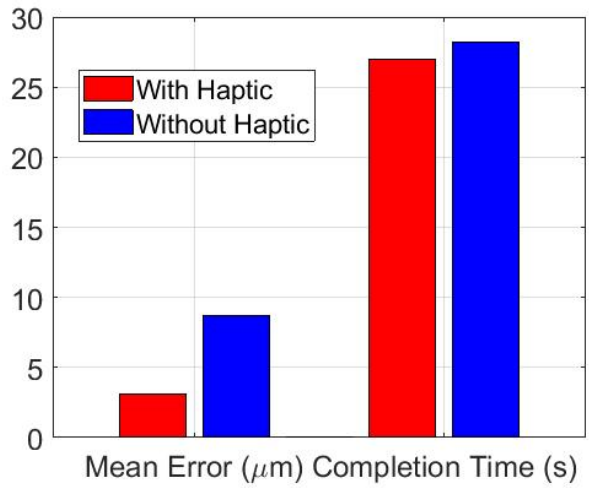

Figure 3.11. The results of the validation study show that teleoperation with haptics in the loop is significantly better than with visual feedback only.

3.7. Conclusion

We developed a teleoperation setup for microrobots using a haptic device and magnetic tweezers. In our setup, the microrobot is virtually linked to the haptic device. Its movements are controlled by the movement of the haptic tool. To improve task performance, the guidance forces are presented to the operator through the haptic interface for better task performance. We conducted a basic set of trials where we tracked a straight line segment using the Falcon device with and without haptic guidance. The trials showed that haptic guidance significantly improves tracking errors but leads to modest benefits in task completion time. Future work will aim at improving the teleoperation system in more complex tasks. Also, the developed haptic glove [54, 55] will be used to perform teleoperation and mapping tasks.

Chapter 4

Inertially Actuated Wheeled Baton Robot

4.1. Introduction

Wheeled locomotion is one of the oldest and most successful inventions of humanity. This form of locomotion is fast, efficient, and easy to create. Yet, wheeled vehicles have constraints when traversing rough terrain and maneuvering in tight spaces. On the other hand, natural creatures do not have wheeled locomotion, mainly because it is impossible to supply blood to a rotating wheel. Instead, nature's solution is to use muscles and limbs to generate regular motions such as walking, running, jumping, galloping, and lateral undulation. Biological creatures are energetically efficient and maneuverable, and they can avoid obstacles with ease. These appealing characteristics of biological systems have led many researchers to mimic biology in developing mobile robots. Yet, most of the resulting systems are limited in speed and have overly complicated drive mechanisms compared to the human-made wheeled robots.

The locomotion of robotic systems is addressed in this chapter. Locomotion refers to the different methods that biological organisms and man-made entities use to navigate in space ([20], [3], [74]). In general, many robots that have been developed are inspired by natural species that "underwent the test" of nature. The most common forms of robotic gait are snake, quadruped, biped, and several forms of legged locomotion (see [157], [150], [113], [68]). But, successes of the biological systems may not necessarily represent the best possibilities for robotic systems. We believe that exploring beyond what nature offers may lead to significant progressions in robotic locomotion.

The inertia-based system relies on the transfer of momentum to initiate a hop. Such systems can be observed when a human being can maximize his/her jump by swinging

his/her arms in a pendulum-like motion. This swing motion enhances the jumping height by 28%. Several hopping robots utilized pendulum-like motion (see [65, 79, 103]). Self-energizing springs and two arms are used in [124] to perform vertical jumps of 18 cm. In [101] have shown that this motion can enhance the jump by 28%. This pendulum-like motion have been utilized in several designs (see [65, 79, 103, 139, 142]). Okubo *et al.* [124] achieved vertical jumps of 18 cm by utilizing self-energizing springs and two arms oscillating at imposed angular velocities and maximum angles. A similar approach was used in [64] to build pendulum-type jumping robots, where the robot performed small vertical jumps by utilizing a two-link machine actuated by a servomotor.

In this chapter, we seek to develop a hybrid robot that is based on wheeled locomotion. Yet it can also generate a rich set of motion modes. We introduced a simple car-like robot that is highly agile, extremely maneuverable, energetically efficient, and capable of performing a variety of locomotive tasks. The design of this robot is challenging because of the robot should have structurally reliable and a compact design so that it can tolerate repeated collisions with the ground. Also, Its control action should lead to stable locomotion that can handle parameter uncertainties and reject disturbances and perturbations.

The motivation of developing the present system comes from previous results reported in [161, 163]. The study revealed that inertial actuation could be used in driving the motion of baton based locomotion systems. In [186], the authors considered a very simple inertially actuated locomotion system consisting of two spinning masses connected with a straight bar (baton). Subsequently, purely inertial actuation was used to guide a "Waddling Robot" in the horizontal plane [88]. Next, in [90], an adaptive control scheme was developed to regulate the motion of an inertially actuated hopper, which is restricted to move vertically. Finally, the theoretical work of the wheeled baton robot was firstly introduced in Kashki's dissertation [86]. However, the main focus of this chapter to experimentally verify the existence of the proposed motion modes.

The rest of this chapter is organized as follows. System description is shown in section 4.2. In Section 4.3, we derive the nonlinear equations of motion of the robot. The motion

modes are discussed in Section 4.4. In Section 4.5, the nonlinear tracking control method is presented. In Section 4.6, the experimental setup is developed. The experimental results are shown in Section 4.7 and the conclusion is presented in Section 4.8.

4.2. System Description

The robot is formed of four identical wheels connected by a rigid link. each wheel can be actuated independently by an actuator (e.g., motor). Figure 4.1 represents the robot schematic the vertical plane ($z = 0$).

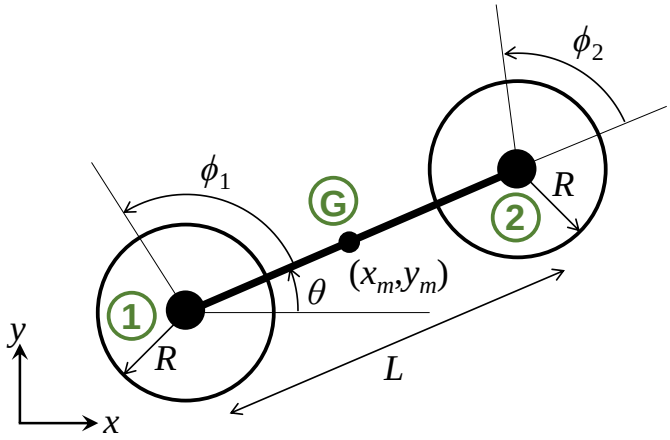

Figure 4.1. Schematic representation of robot

Here, L is the link length, m_b is the mass of the rigid link, and R is the radius of the wheels. Also, m is the mass of the wheels, M is the mass of actuator (e.g., motor). Therefore, the system has five degrees of freedom with generalized coordinates vector of $q = [\theta, \phi_1, \phi_2, x_m, y_m]^T$, where θ is the angle of the link with respect to the positive direction of x-axis, ϕ_1 and ϕ_2 are the angular position of the wheels with respect to the link, x_m and y_m are the horizontal and vertical positions of the center of the link in the inertial reference frame. The angular positions θ, ϕ_1 and ϕ_2 are measured in the counterclockwise rotational directions.

4.3. Equations of Motion

The equations of motion are derived using Lagrange's method. The robot's center of mass position vectors and the centers of the wheels as shown in Figure 4.1 can be written as follows:

$$\begin{aligned}
\boldsymbol{r}_G &= \begin{pmatrix} x_m \\ \\ y_m \end{pmatrix} \\
\boldsymbol{r}_1 &= \boldsymbol{r}_G + R_z(\theta) \begin{pmatrix} -L/2 \\ \\ 0 \end{pmatrix} \\
\boldsymbol{r}_2 &= \boldsymbol{r}_G + R_z(\theta) \begin{pmatrix} L/2 \\ \\ 0 \end{pmatrix}
\end{aligned} \tag{4.1}$$

where, $R_z(\cdot)$ is the rotation matrix about the z-axis. This matrix can be expressed as follows:

$$R_z(\alpha) = \begin{bmatrix} \cos\alpha & -\sin\alpha \\ \\ \sin\alpha & \cos\alpha \end{bmatrix} \tag{4.2}$$

The robot center of mass and wheels angular velocities are obtained by differentiating the corresponding position and angular position vectors, respectively. and they are as follows:

$$\begin{aligned}
&\boldsymbol{v}_1 = \dot{\boldsymbol{r}}_1, \boldsymbol{v}_2 = \dot{\boldsymbol{r}}_2, \boldsymbol{v}_G = \dot{\boldsymbol{r}}_G \\
&\boldsymbol{\omega}_1 = \dot{\phi}_1 \boldsymbol{k}, \boldsymbol{\omega}_2 = \dot{\phi}_2 \boldsymbol{k}, \boldsymbol{\omega}_b = \dot{\theta} \boldsymbol{k}
\end{aligned} \tag{4.3}$$

where, $\boldsymbol{v}_1$, $\boldsymbol{v}_2$ and $\boldsymbol{v}_G$ are velocity vectors of wheels' center and link's center respectively, $\boldsymbol{\omega}_1$, $\boldsymbol{\omega}_2$ and $\boldsymbol{\omega}_b$ are angular velocity vectors of wheels and the link respectively, and $\boldsymbol{k}$ is the unit vector along the z-axis. The robot dynamics can be divided into three distinct modes of motion as follows:

(i) *Vehicle Mode (V)*: Both wheels are in contact with the ground surface. The wheels may slide while rolling on the surface;

(ii) *Wheelie Mode (W)*: One of the wheels is in the air while another is in contact with the ground;

(iii) *Flight Mode (F)*: Both wheels are in the air.

Now, the equations of motion can be obtained using the Lagrangian formulation:

$$\begin{aligned} &\mathcal{L} = \mathcal{T} - \mathcal{V} \\ &\frac{d}{dt}\left[\frac{\partial \mathcal{L}}{\partial \dot{q}_j}\right] - \frac{\partial \mathcal{L}}{\partial q_j} = \mathcal{Q}_j \\ &j = 1, 2, \cdots, n_q \end{aligned} \tag{4.4}$$

Where $\mathcal{T}$ and $\mathcal{V}$ are the kinetic and potential energies, respectively. Also, q_j is the jth generalized coordinate, $\mathcal{Q}_j$ is the jth generalized force, and $n_q = 5$ is the number of generalized coordinates. The generalized forces in each mode of motion are defined based on D'Alambert principle of virtual work:

$$\begin{aligned} \delta W &\equiv \sum_k \boldsymbol{f}_k \cdot \boldsymbol{\delta r}_k + \sum_r \boldsymbol{\Gamma}_r \cdot \boldsymbol{\delta \theta}_r \\ &= \sum_{j=1}^{n_q} \mathcal{Q}_j \delta q_j \end{aligned} \tag{4.5}$$

where, δW is the virtual work, $\boldsymbol{f}_k$'s and $\boldsymbol{\Gamma}_r$'s are the external forces and moments respectively, and $\boldsymbol{\delta r}_k$'s and $\boldsymbol{\delta \theta}_r$ are the virtual displacement and rotation vectors respectively.

All three motion modes have the same system's kinetic and potential energy functions:

$$\mathcal{T} = K_{tr} + K_{rot} \tag{4.6}$$

where K_{tr}, K_{rot}, and $\mathcal{V}$ are obtained as follows:

$$K_{tr} = \frac{1}{2}\Big[(m+M)\left(\boldsymbol{v}_1 \cdot \boldsymbol{v}_1 + \boldsymbol{v}_2 \cdot \boldsymbol{v}_2\right) + m_b \boldsymbol{v}_G \cdot \boldsymbol{v}_G\Big] \tag{4.7}$$

$$K_{rot} = \frac{1}{2}\Big[J_w\left(\boldsymbol{\omega}_1 \cdot \boldsymbol{\omega}_1 + \boldsymbol{\omega}_2 \cdot \boldsymbol{\omega}_2\right) + J_b \boldsymbol{\omega}_b \cdot \boldsymbol{\omega}_b\Big] \tag{4.8}$$

$$\mathcal{V} = g\Big[(m+M)(\boldsymbol{r}_1 + \boldsymbol{r}_2) + m_b \boldsymbol{r}_G\Big] \cdot \boldsymbol{j} \tag{4.9}$$

Where, K_{tr} and K_{rot} are translational and rotational kinetic energies respectively, J_w is the moment of inertia of the wheels about their centroidal axes, J_b is the link's moment of inertia about its center of mass, $\boldsymbol{j}$ is the unit vector along the y-axis, "$\cdot$" is the inner product operator, and g is the gravitational acceleration. We assume that the wheels and the link have uniformly distributed masses. Therefore, the moment of inertia can be obtained as follows:

$$J_w = \frac{1}{2} m R^2 \tag{4.10}$$

$$J_b = \frac{1}{12} m_b L^2 \tag{4.11}$$

Figure 4.2 shows the general free-body-diagram of the wheeled baton robot. Here, $\boldsymbol{W}_1 = \boldsymbol{W}_2 = -(m+M)g\,\boldsymbol{j}$ and $\boldsymbol{W}_b = -m_b g\,\boldsymbol{j}$ are gravitational forces, c_1 and c_2 are wheels contact point with the ground surface, β_1 and β_2 are the angular positions of the contact points with respect to vertical axis in counter-clockwise directions. Moreover, the contact point position angle can be defined as the angle of the tangent line to the road profile at the corresponding

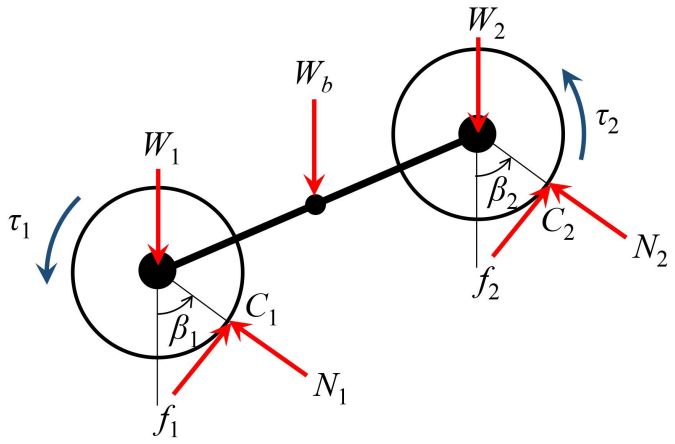

Figure 4.2. General free-body-diagram of the system

contact point:

$$\beta_i = \tan^{-1}\left(\frac{d}{dx}\rho(\boldsymbol{r}^{c_i}\cdot\boldsymbol{i})\right);\quad i=1,2 \tag{4.12}$$

where, $\rho=\rho(x)$ is the road profile, $\boldsymbol{r}^{c_i}$ is the corresponding contact point position vector, and $\boldsymbol{i}$ is the unit vector of the positive direction of the x-axis.

Furthermore, $\boldsymbol{N}_1$ and $\boldsymbol{N}_2$ are normal forces due to unilateral constraints at the contact points, and $\boldsymbol{f}_1$ and $\boldsymbol{f}_2$ are friction forces based on Coulomb's model due to rolling/slipping wheel contacts. The friction and normal forces can be written as:

$$\begin{aligned}\boldsymbol{N}_1 &= N_1\boldsymbol{e}_n^{c_1},\ \boldsymbol{f}_1 = -\mu N_1\ sign(\boldsymbol{v}^{c_1}\cdot\boldsymbol{e}_t^{c_1})\boldsymbol{e}_t^{c_1}\\ \boldsymbol{N}_2 &= N_2\boldsymbol{e}_n^{c_2},\ \boldsymbol{f}_2 = -\mu N_2\ sign(\boldsymbol{v}^{c_2}\cdot\boldsymbol{e}_t^{c_2})\boldsymbol{e}_t^{c_2}\end{aligned} \tag{4.13}$$

where, $\boldsymbol{e}_n^{c_1}$, $\boldsymbol{e}_n^{c_2}$, $\boldsymbol{e}_t^{c_1}$, and $\boldsymbol{e}_t^{c_2}$ are the normal and tangent unit vectors at contact points, respectively. The $\boldsymbol{v}^{c_1}$ and $\boldsymbol{v}^{c_2}$ are velocity vectors of contact points ($\boldsymbol{v}^{c_i}=\dot{\boldsymbol{r}}^{c_i}$), and μ is the coefficient of Coulomb friction.

In addition, Eq.(4.13) implies that each mode of motion requires two additional constraint equations that depend on contact conditions. Then, the complete set of equations of motion

can be formed by using Eqs.(4.4), (4.13), and the two additional constraint equations that are summarized in Table 4.1.

Table 4.1. Additional constraint equations

Mode of Motion	Constraint Equations
Vehicle Mode	$\boldsymbol{v}^{c_1} \cdot \boldsymbol{e}_n^{c_1} = 0 \ \wedge \ \boldsymbol{v}^{c_2} \cdot \boldsymbol{e}_n^{c_2} = 0$
Wheelie Mode	$\boldsymbol{v}^{c_i} \cdot \boldsymbol{e}_n^{c_i} = 0 \ \wedge \ \boldsymbol{N}_j = 0; \ \ i \neq j = 1, 2$
Flight Mode	$\boldsymbol{N}_1 = 0 \ \wedge \ \boldsymbol{N}_2 = 0$

When the wheels collide with the ground, the robot experiences multiple collisions ([75] and [23]). The impact problem can be expressed as follows:

$$\begin{aligned} \dot{\zeta}^{+} &= impact(\zeta, \dot{\zeta}^{-}) \\ \zeta &= [x_1, y_1, x_m, y_m, x_2, y_2, \phi_1, \phi_2, \theta] \end{aligned} \tag{4.14}$$

where, $\dot{\zeta}^{+}$ is the post-impact velocity vector and ζ and $\dot{\zeta}^{-}$ are the position and the pre-impact velocity vectors respectively. The solution to the impact problem is complex. Such problems have been addressed in the literature and the reader may refer to [10, 23, 75, 141, 161] for solution of similar problems.

Finally, the equations for each mode of motion can be written in the following general form:

$$H(q_i)\ddot{q}_i + C(q_i, \dot{q}_i) + G(q_i) = Q(q_i, \dot{q}_i) \tag{4.15}$$

where, $H(q_i)$ is the inertia matrix, $C(q_i, \dot{q}_i)$ is the Coriolis matrix, $G(q_i)$ is gravitational, and $Q(q_i, \dot{q}_i)$ is the generalized force matrix. The equations of motion are highly nonlinear due to the presence of trigonometric functions. Thus, we use Wolfram Mathematica© to numerically analyze their solutions.

4.4. Modes of Motion

The transition between different modes of motion of the wheeled baton robot is presented in [86]. Therefore, we present them briefly in this section. The wheels' actuation torques enable the robot to transition between different modes of motion. The mode transition flow diagram is shown in Figure 4.3. We assume that the robot moves along a horizontal path to simplify the analysis. In this case, β_1 and β_2 are zeros. At any instant of time, the robot dynamics can be described in one of these unique modes.

$$\pi \in \{V, W_1, W_2, F\} \tag{4.16}$$

Where, π is the mode of motion, V stands for vehicle mode of motion, W_1 and W_2 denote wheelie mode with wheel 1 and wheel 2 in contact with the ground surface respectively, and F means flight mode of motion. We assign a particular mode transition with "$\pi_k \rightarrow \pi_{k+1}$" where π_k is the current mode and π_{k+1} is the next mode of motion. Only two modes are considered in this dissertation, vehicle to wheelie and wheelie to vehicle modes. The details of transition modes can be described as follows:

4.4.1. Vehicle to Wheelie Mode Transition

Based on the assumption that the robot travels along a horizontal path and vehicle mode constraint, the robot orientation and height are:

$$\theta(t) = 0, \; y_m(t) = R \tag{4.17}$$

Then, the normal forces on each wheel can be obtained by solving Eqs.(4.4) and (4.17), which gives:

$$\begin{aligned} N_1 &= g\Big(m + M + \frac{m_b}{2}\Big) - \frac{\tau_1 + \tau_2}{L} \\ N_2 &= g\Big(m + M + \frac{m_b}{2}\Big) + \frac{\tau_1 + \tau_2}{L} \end{aligned} \tag{4.18}$$

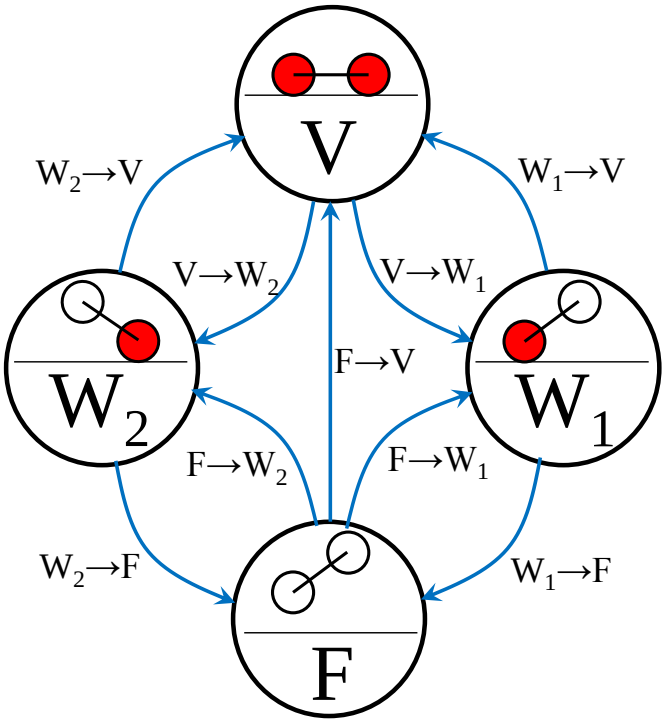

Figure 4.3. Mode of motion transition flow diagram

Therefore, the vehicle mode of motion transition into wheelie mode when the following torque combination values are satisfied :

$$
\begin{aligned}
&V \rightarrow W_1 : \tau_1 + \tau_2 \leq -\tau^W \\
&V \rightarrow W_2 : \tau_1 + \tau_2 \geq \tau^W \\
&\tau^W = gL\Big(m + M + \frac{m_b}{2}\Big)
\end{aligned}
\tag{4.19}
$$

where, W_1 and W_2 are wheelie modes with wheel 1 and wheel 2 is in contact with the ground respectively, and τ^W is the minimum required combined torque to transit to wheelie mode from vehicle mode. Also, Eq.(4.19) implies the system cannot reach flight mode directly from vehicle mode of motion. Figure 4.4 represents the torques map corresponding to different modes of motion.

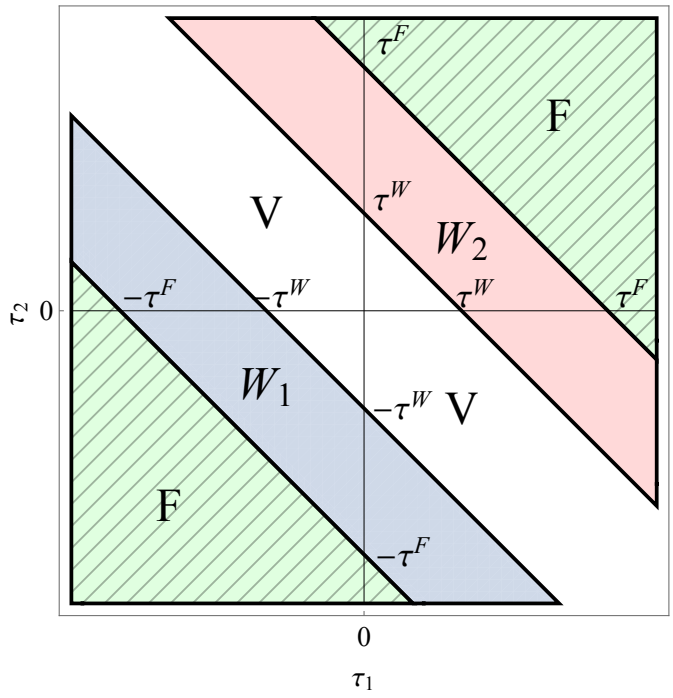

Figure 4.4. Torque map for different modes of motion

4.4.2. Wheelie to Vehicle Mode Transition

When the wheel in the air hits the ground, the wheelie mode may involve multiple micro impacts. Therefore, The transition occurs when the collisions subside, and θ reaches zero.

$$\begin{aligned} W_1 \to V &: \sin\theta = 0 \ \wedge \ \boldsymbol{v}^{c_2} \cdot \boldsymbol{j} = 0 \\ W_2 \to V &: \sin\theta = 0 \ \wedge \ \boldsymbol{v}^{c_1} \cdot \boldsymbol{j} = 0 \end{aligned} \tag{4.20}$$

4.5. Control Design

This section addresses the control design for this tracking problem. Here we propose feedback linearizing variable structure control (VSC) method because of its effectiveness and robustness in control of nonlinear systems. This is a modified version of the method

presented in [86, 140]. For this purpose, Eq.(4.4) can be rewritten in affine-control form as:

$$\begin{aligned} \dot{\boldsymbol{x}} &= \mathbf{f}(\boldsymbol{x}) + \mathbf{g}(\boldsymbol{x})\tau \\ \boldsymbol{y} &= \mathbf{h}(\boldsymbol{x}) \end{aligned} \tag{4.21}$$

where, $\boldsymbol{x} = [\theta, \dot{\theta}, \phi_1, \dot{\phi}_1, \phi_2, \dot{\phi}_2, x_m, \dot{x}_m, y_m, \dot{y}_m]^T$ is 10×1 state variables vector, $\boldsymbol{y} = [y_1, y_2]^T$ is 2×1 output vector, $\mathbf{f}$ is 10×1 drift vector field, $\mathbf{g}$ is 10×2 input vector fields, $\mathbf{h} = [h_1, h_2]^T$ is 2×1 output vector field, and $\boldsymbol{\tau} = [\tau_1, \tau_2]^T$ is motor torques.

Assume that r_j is the relative degree of the jth output, which is the smallest number of differentiation such that input appears in the output y_j. Then, differentiating the outputs r_j times yields:

$$\mathbf{Y} = \mathbf{F}(\boldsymbol{x}) + \mathbf{G}(\boldsymbol{x})\boldsymbol{u} \tag{4.22}$$

where,

$$\mathbf{Y} = \begin{bmatrix} y_1^{(r_1)} \\ \\ y_2^{(r_2)} \end{bmatrix}, \mathbf{F}(\boldsymbol{x}) = \begin{bmatrix} L_{\mathbf{f}}^{r_1} h_1 \\ \\ L_{\mathbf{f}}^{r_2} h_2 \end{bmatrix} \tag{4.23}$$

$$\mathbf{G}(\boldsymbol{x}) = \begin{bmatrix} L_{\mathbf{g_1}}(L_{\mathbf{f}}^{r_1-1} h_1) & L_{\mathbf{g_2}}(L_{\mathbf{f}}^{r_1-1} h_1) \\ \\ L_{\mathbf{g_1}}(L_{\mathbf{f}}^{r_2-1} h_2) & L_{\mathbf{g_2}}(L_{\mathbf{f}}^{r_2-1} h_2) \end{bmatrix} \tag{4.24}$$

where, $\boldsymbol{u} = [\tau_1, \tau_2]^T$ is the control input vector containing the torques applied by the wheels. and L is the Lie Derivative operator defined as:

$$\begin{aligned} L_X Y &= X \frac{\partial Y}{\partial \boldsymbol{x}} \\ L_X^r y &= L_X(L_X^{r-1} Y) \end{aligned} \tag{4.25}$$

Applying feedback linearization principle to Eq.(4.22) yields:

$$\boldsymbol{u} = \mathbf{G}(\boldsymbol{x})^{-1}[-\mathbf{F}(\boldsymbol{x}) + \boldsymbol{v}] \tag{4.26}$$

where, $\boldsymbol{v}$ is the pseudo-input variable. We define the two-dimensional sliding surface as a linear function of tracking error signal, given by:

$$\begin{aligned} s_j &= \frac{d^{r_j-1}e_j}{dt^{r_j-1}} + \sum_{r=0}^{r_j-2} \lambda_r \frac{d^r e_j}{dt^r}; j = 1, 2 \\ \boldsymbol{e} &= \boldsymbol{y} - \boldsymbol{y}_d \end{aligned} \tag{4.27}$$

where, λ's are the placed poles of characteristic polynomial ($Re(\lambda_i) < 0$), $\boldsymbol{y}_d$ is desired outputs, and $\boldsymbol{e}$ is the tracking error. Suppose the following positive definite *Lyapanov* function.

$$V = \frac{1}{2}\boldsymbol{s}^T\boldsymbol{s} > 0 \tag{4.28}$$

where, $\boldsymbol{s}$ is the sliding surface vector field. The dynamics of sliding surface functions should guarantee stable dynamics of $\boldsymbol{e}$ when $\boldsymbol{s}$ approaches to zero, where $\boldsymbol{e} = \boldsymbol{y} - \boldsymbol{y}_d$ is the tracking error vector, and $\boldsymbol{y}_d$ is the vector of desired trajectories. The sliding surface can be defined as:

$$\boldsymbol{s} = \dot{\boldsymbol{e}} + \lambda\, \boldsymbol{e} \tag{4.29}$$

where, $\lambda > 0$ is the convergence rate. The pseudo-input is obtained by solving Eq.(4.26)

satisfying

$$v_j = \frac{d^{r_j} y_j}{dt^{r_j}} - \sum_{r=1}^{r_j - 1} \lambda_r \frac{d^r e_j}{dt^r} - \eta \, tanh\Big(\frac{s_j}{\phi}\Big) \tag{4.30}$$

$$\dot{\boldsymbol{s}} = -\eta \, tanh\Big(\frac{\boldsymbol{s}}{\varphi}\Big) \tag{4.31}$$

Using Eqs. (4.26)-(4.30) yields:

$$\dot{V} = \dot{\boldsymbol{s}}^T \boldsymbol{s} = -\eta \sum_j s_j tanh\Big(\frac{s_j}{\varphi}\Big) < 0 \tag{4.32}$$

Here, the role of $\eta > 0$ is to overcome system uncertainties and un-modeled dynamics and guarantee the negative definiteness of derivative of the Lyapunov function. Having a positive definite Lyapunov function and a negative definite derivative ensures the convergence of the sliding surface $\boldsymbol{s} = 0$.

4.6. Experimental Setup

An experimental robot is developed to verify the concept of inertial actuation for the wheeled baton robot. Figure 4.5 shows the CAD and the actual models of the robot. It is a planar bicycle-like robot and has a four-wheel vehicle structure with large wheels and compact chassis. The robot has two wheel assemblies. Each assembly consists of two motors, two encoders, and one motor controller.

In our design, four brushless DC motors are selected to meet the torque requirements obtained from the numerical analysis. The motor model is D5065-270 KV. Also, an encoder is mounted on each wheel. Rotary encoders measure the spinning velocity of the wheels. We choose the CUI AMT102 optical rotary encoder to meet the design and motor requirements. It provides 8192 counts per revolution in the quadrature mode. The motors were controlled using the off-the-shelf motor controller, ODrive. It can be used to perform current, velocity, and position control tasks. In this project, it is used to perform torque-related tasks. It uses the field-ordinated-control method to regulate the motor torques at a frequency of 10 kHz.

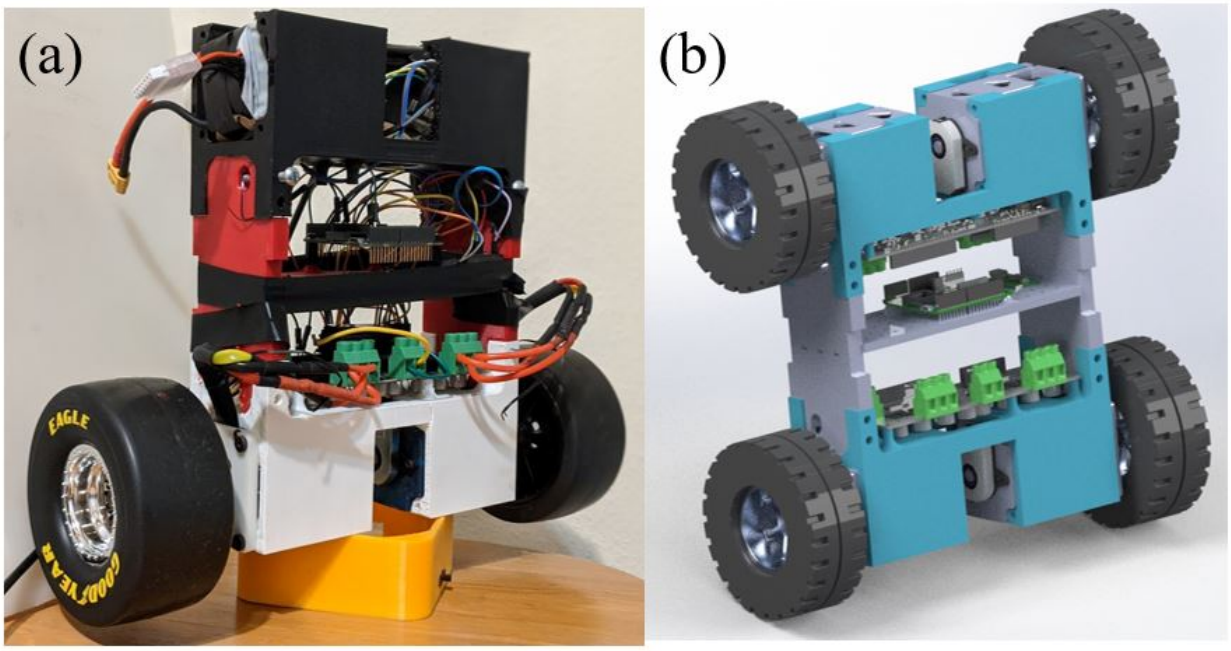

Figure 4.5. The Wheeled Baton Robot. (a) The actual robot. (b) The CAD model.

Finally, each set of two motors and encoders is integrated through a single ODrive controller. The wheel-assembly parameters are shown in Table 4.2.

An inertial measurement unit (IMU) is used to measure robot orientation and angular velocity. We select Xsens MTi-3 AHRS model in our design because it provides high-rate, accurate measurements. It uses Extended Kalman filtering to provide data rate up to 100 Hz for body angles and up to 800 Hz for the raw data. In addition, a 6S battery equipped with a power distribution board (PDB) is used to provide a constant voltage supply to all the components. Also, a wireless remote controller (RC) is used to send high-level commands to the robot. Finally, the main core of the control system is implemented on a powerful microcontroller. A low-cost and Arduino-compatible Teensy 4.0 from PJRC is selected because it features real-time capabilities and multi-channel communication. The technical specifications of Teensy 4.0 are shown in Table 4.3.

In summary, the electrical system of the robot consists of a microcontroller, four motors (M), two motor controllers (ODrive), an inertial measurement unit (Xsens), a battery,

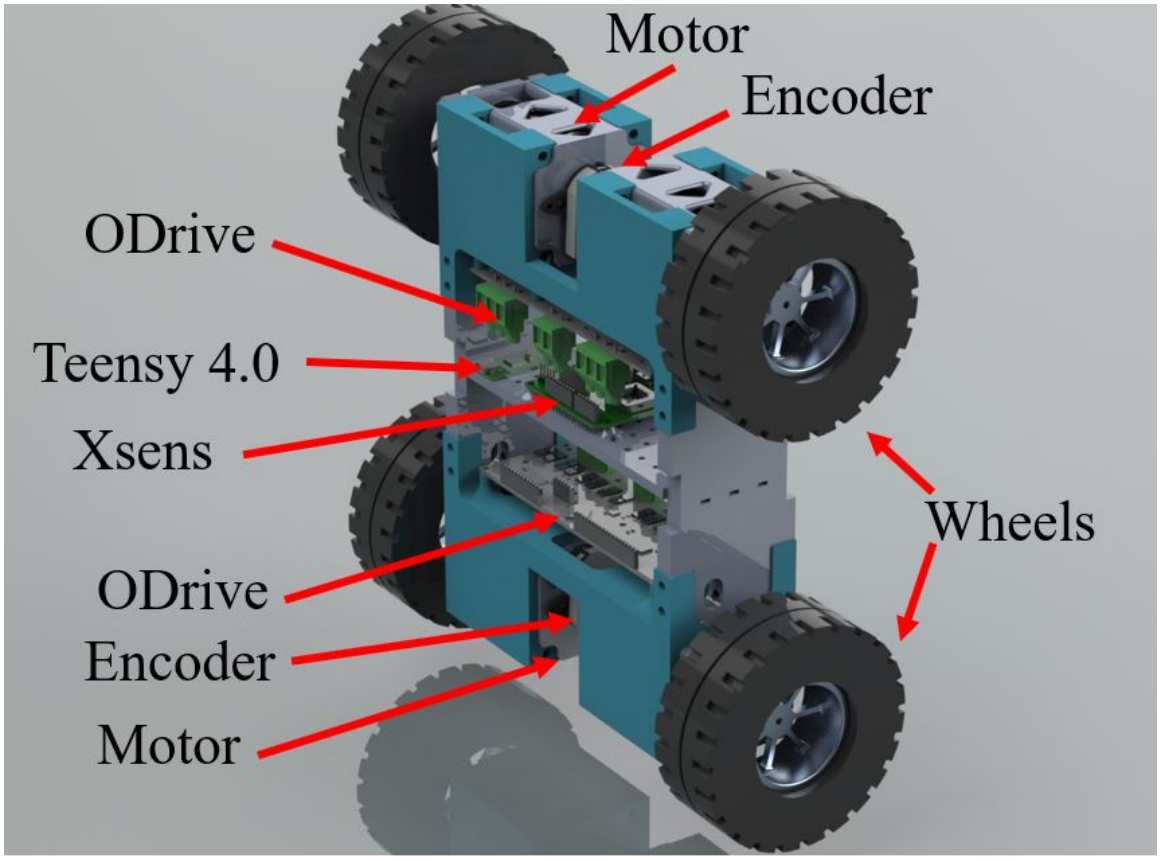

Figure 4.6. The Wheeled Baton Robot hardware.

a power distribution board (PDB), and an RC receiver. The electrical system is summarized in Fig. 4.7, the black and green lines represent power and communication flow lines, respectively. The robot's physical parameters are listed in Table 4.4.

The control algorithm proposed in Section 4.5 is implemented on the Teensy 4.0 board using the C++ programing language. The tracking control algorithm is executed with a frequency of 200 Hz, and the torque control loop is executed on the ODrive board at 10 kHz. The radio RC is used to select the desired mode as well as the desired progression velocity. Figure 4.8 shows the experimental control block diagram, where the distribution of the control loops is illustrated. The black and green lines represent the feedforward and feedback paths, respectively.

The robot control system can be divided into three layers. First, the operator-microcontroller

Table 4.2. The wheel-assembly parameters

Description	Value
Motor mass	0.420 kg
Motor maximum voltage	32 V
Motor max current	65 A
Motor torque	1.99 N.m
Motor velocity	8640 RPM
Encoder type	through bore
Encoder resolution	8192 count/rev
Encoder Max speed	7500 RPM
Odrive channels	2
Odrive peak current	120 A per motor
Odrive feedback	Encoder and hall sensor
Odrive interface	USB, UART, CAN, and PWM
Odrive control feature	position, velocity, and torque controls

layer, where the operator sends the high-level command, such as motion mode and desired progression velocity. Second, the microcontroller-Odrive layer, where the microcontroller computes the motor torques and sends them to the ODrive. Finally, The ODrive-motor layer, where the ODrive controls and generates the current to provide the desired torque.

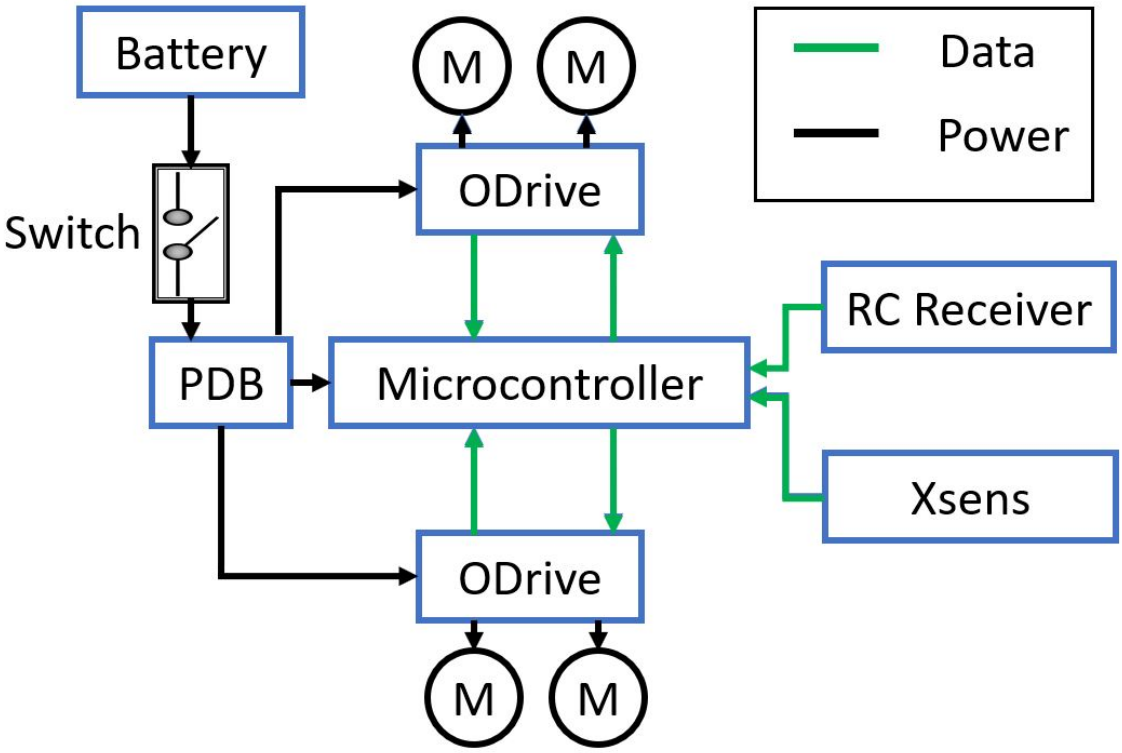

Figure 4.7. The electrical system diagram.

Table 4.3. Teensy 4.0 specifications

Description	Value
CPU	ARM Cortex-M7 at 600 MHz
Size	1.4 by 0.7 inch
Pins	40 digital pins, 31 PWM, 14 analog pins, all interrupt capable
Interfaces	2 USB, 7 UART, 3 CAN, 3 I2C, 3 SPI

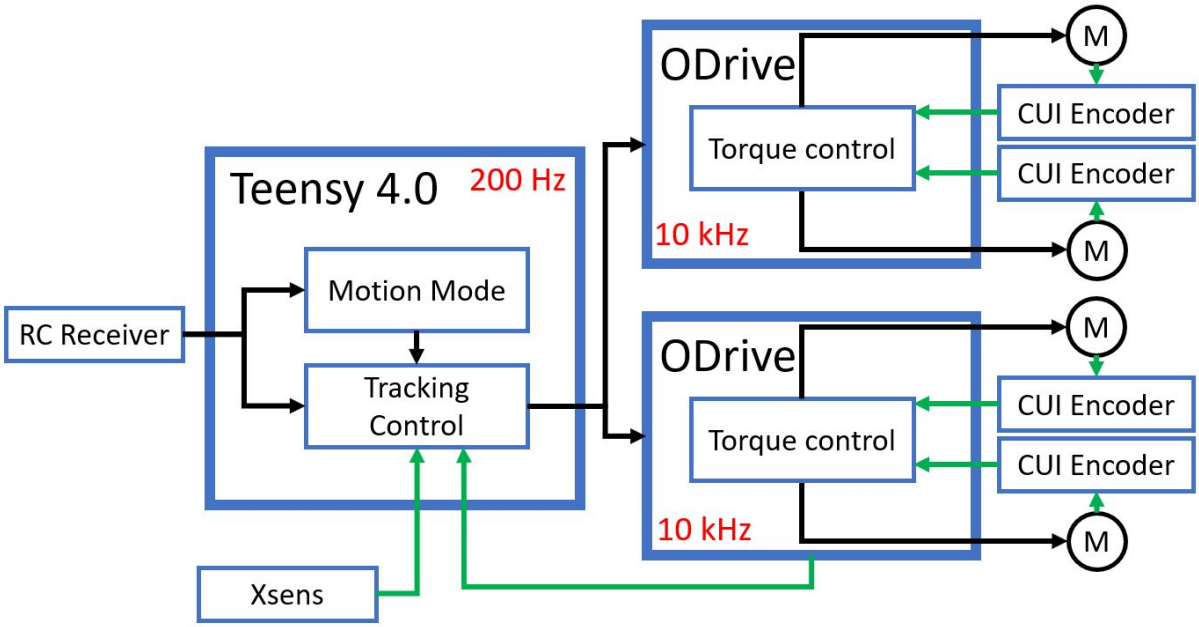

Figure 4.8. The control block diagram.

Table 4.4. Robot Physical Parameters

Symbol	Description	Value
M	Mass of each motor	0.42 kg
m	Mass of each wheel	0.165 kg
m_b	Mass of rigid link	1.0 kg
m_r	The robot total mass	2.4 kg
L	Length of main link	30 cm
R	Radius of wheels	10 cm

4.7. Experimental Results

In this section, we present two sets of experiments that were conducted to verify the idea of this robot. In the first experimental run, we demonstrate the capabilities of the proposed design to transition between different motion modes. The second set of experiments were conducted to demonstrate the inverted pendulum locomotion. In each test, the robot is initially in vehicle mode at rest.

4.7.1. Modes of Motion Transition

In this section, the transition between the motion modes is presented. First, the transition from vehicle to wheelie mode is demonstrated. The robot is initially at rest in vehicle mode with a robot angle θ of 185 deg. Then the RC is used to send a signal to initiate the transition from vehicle to wheelie mode. The robot angle reaches approximately 90 deg in the wheelie mode. Figure 4.9a shows the time response of the robot angle, and the blue and red lines represent the desired and robot angles, respectively. The robot position is shown in Fig. 4.9b.The green line represents the robot's center trajectory of the robot, and the black rectangle represents the robot's body. The black color is the final pose, whereas the gray is the initial pose of the robot.

The transition is easier in case of the transition from wheelie to vehicle mode because the robot is going from an unstable to a stable configuration, as shown in 4.10a. Figure 4.10b depicts the time response of the robot angle. The blue and red lines represent the desired and robot angles, respectively.

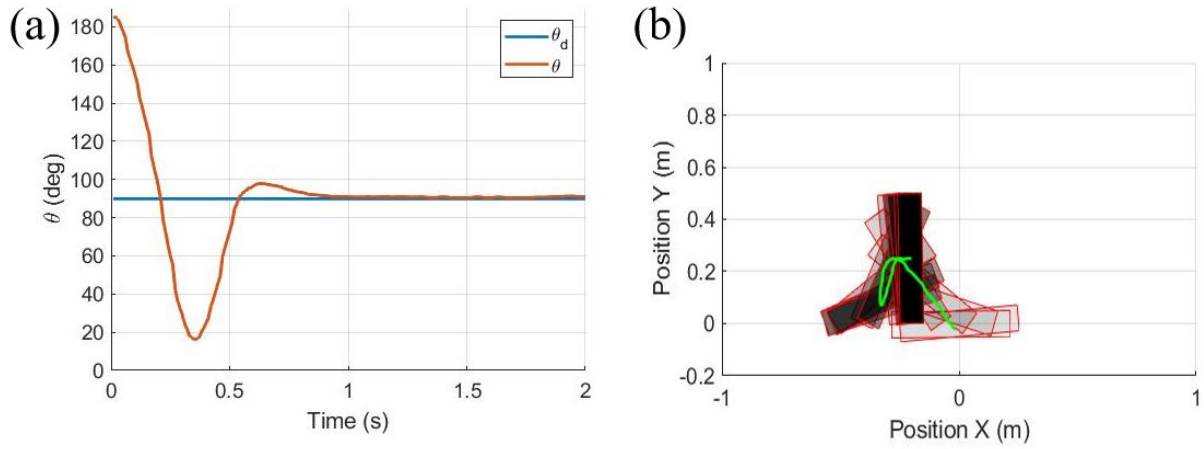

Figure 4.9. The transition from vehicle to wheelie mode. (a) The time response of the robot's angle. (b) The robot's center trajectory.

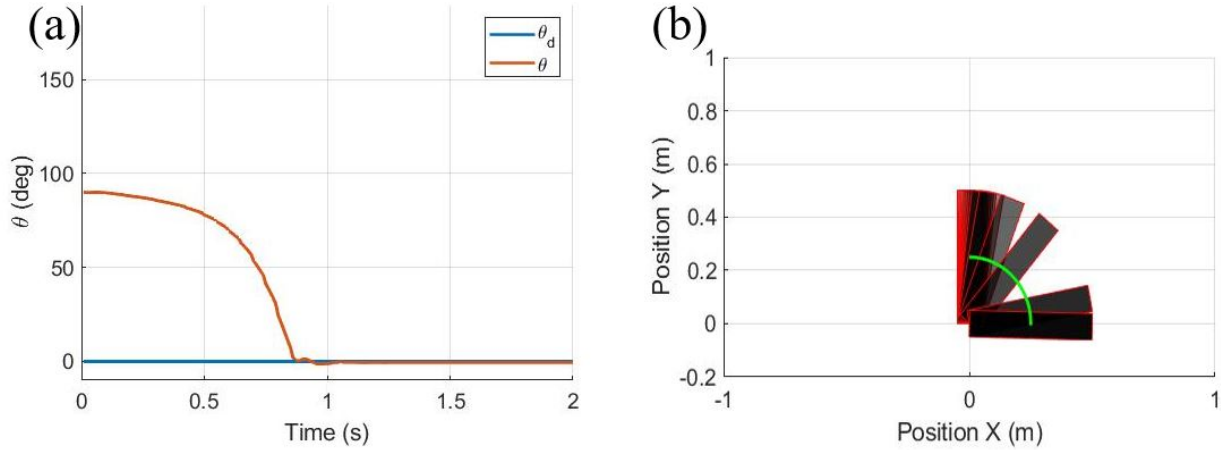

Figure 4.10. The transition from wheelie to vehicle mode. (a) The time response of the robot's angle. (b) The robot's center trajectory.

4.7.2. Inverted Pendulum Locomotion

In this experiment, we have tested the inverted pendulum locomotion pattern on flat and inclined surfaces. In the two tests, the robot is initially at rest. Then the operator sends the command to initiate the transition from vehicle to wheelie mode. When the robot enters the wheelie mode, the operator can define the progression velocity via the RC to perform the inverted pendulum locomotion pattern.

Figure 4.11 depicts the experimental results of the inverted pendulum locomotion on a flat surface. The pattern is scheduled as follows. First, the robot starts at rest in vehicle mode. Then, the robot transitions to wheelie mode in 1 second. Finally, the robot tracks the desired progression speed. The time response of the robot angle is shown in Fig. 4.11b, and the blue and red lines represent the desired and robot angle, respectively.

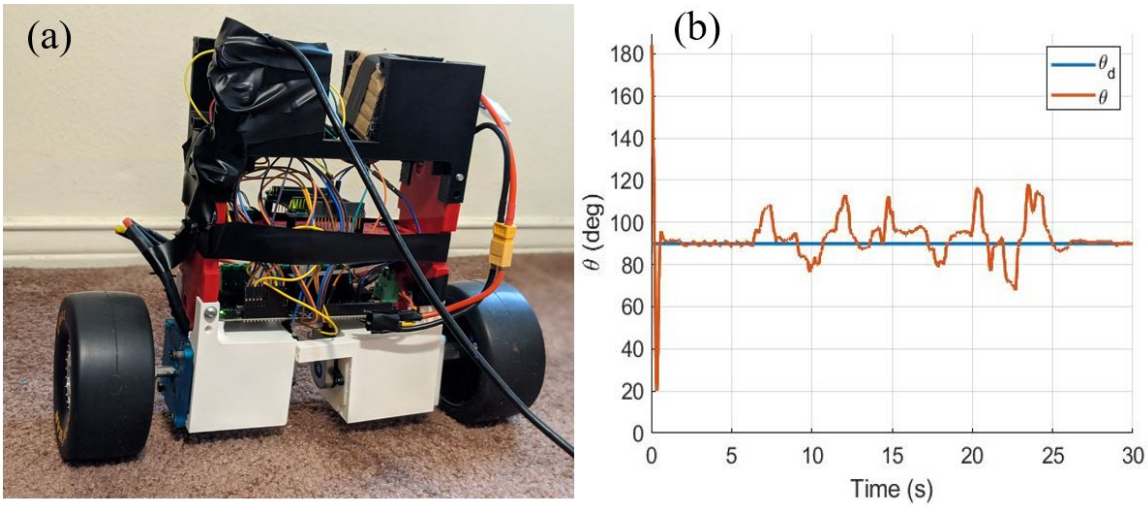

Figure 4.11. The experimental result of the inverted pendulum locomotion pattern on a flat surface. (a) The Wheelie mode on a flat surface. (b) The time response of the robot angle.

Additionally, the robot is able to balance and perform the same pattern on a 20 deg inclined surface, as shown in 4.12.The same pattern as in the flat case is scheduled. The main link angle as a function of time is presented in Fig. 4.12b.

4.7.3. Validation

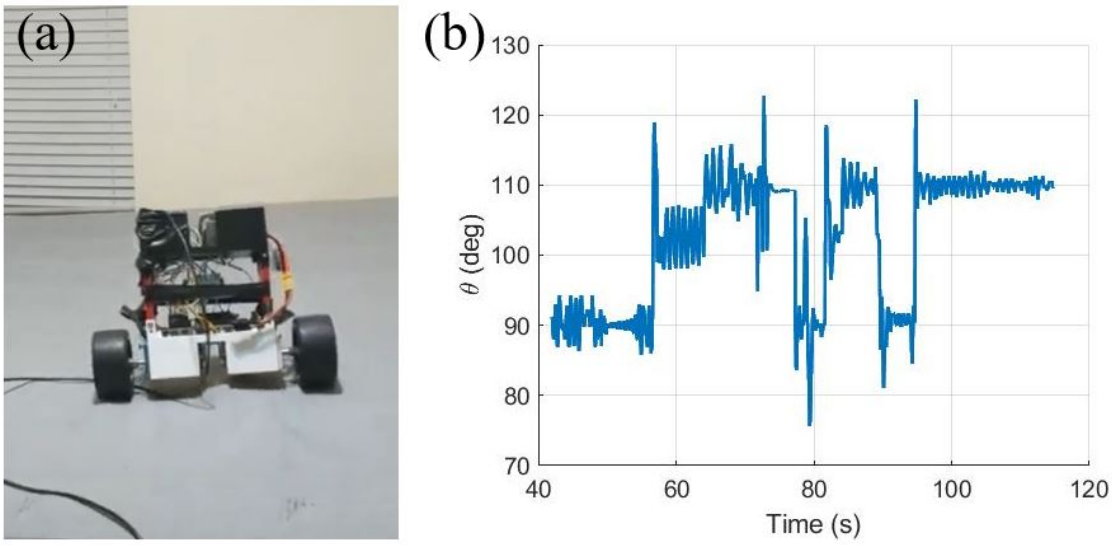

Figure 4.12. The Wheelie mode on a 20 deg inclined surface.

In this section, we present a validation test to verify the robustness of the proposed controller. In this test, an external load of 420 g is attached to the robot body (see Fig. 4.13), thereby changing the robot's mass, center of gravity, and moment of inertia. The ratio of the added mass to the robot total mass is about 20%. Also, the controller has no information about the added mass, the surface friction, normal forces, and contact angles.

Figure 4.14 shows the robot angle during the transition from vehicle to wheelie mode in the presence of the added uncertainties. As can be seen from the time response, the robot angle θ has a larger overshoot compared to the case without the added mass. The inverted pendulum pattern is also demonstrated, with the robot balancing at 100 deg, as shown in Fig. 4.14b. The equilibrium point is 100 deg instead of 90 deg because the added mass shifts the center of gravity outward from the robot axis.

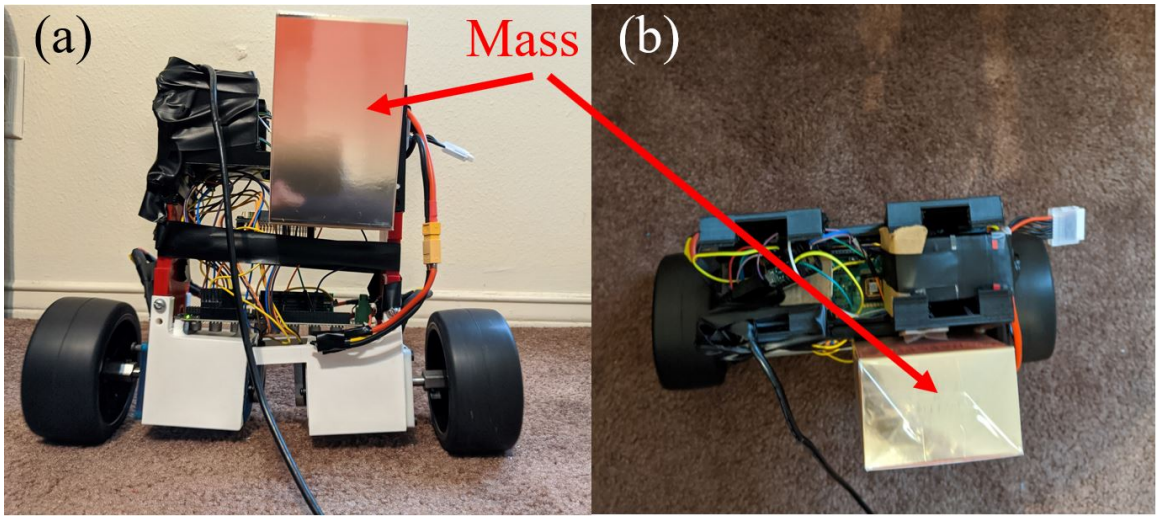

Figure 4.13. The Wheelie mode on a flat surface with large uncertainties in robot mass and inertia. (a) The front view. (b) The top view.

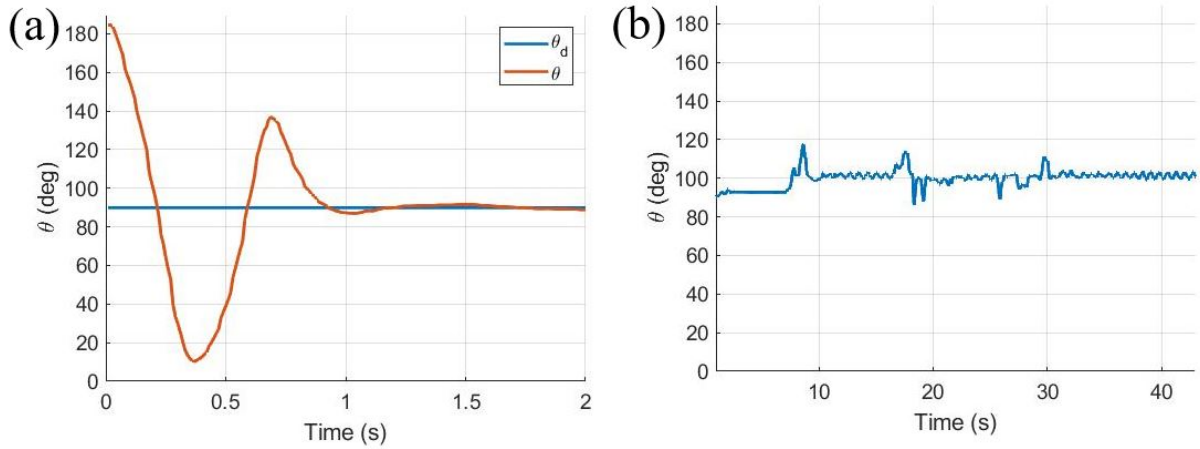

Figure 4.14. The Wheelie mode on a flat surface with large uncertainties in robot mass and inertia. (a) The transition from vehicle to wheelie mode. (b) The inverted pendulum locomotion.

4.8. Conclusion

In this chapter, we introduce a wheeled, inertially actuated robot. The proposed system is described, and different modes of motion of the system are identified. Then, equations of motion, as well as kinematic constraints of each mode, are derived. We proved mathematically that each mode of motion could transform into a dynamically well-defined set of modes of motion. We showed that a wide range of locomotion patterns could be generated using different transitions of identified locomotion modes. Next, a nonlinear tracking controller is designed to fulfill the control schedule of modes of locomotion pattern. Finally, we designed and built an experimental prototype to verify the existence of the locomotion modes. We demonstrated experimentally that a car-like robot could generate several locomotion modes. The locomotion modes enable the robot to navigate in different environments and perform complicated tasks.

BIBLIOGRAPHY

[1] Abbott, J. J. Parametric design of tri-axial nested helmholtz coils. *Review of Scientific Instruments 86*, 5 (2015), 054701.

[2] Abbott, J. J., Peyer, K. E., Lagomarsino, M. C., Zhang, L., Dong, L., Kaliakatsos, I. K., and Nelson, B. J. How should microrobots swim? *The international journal of Robotics Research 28*, 11-12 (2009), 1434–1447.

[3] Adolfsson, J., Dankowicz, H., and Nordmark, A. 3d passive walkers: Finding periodic gaits in the presence of discontinuities. *Nonlinear Dynamics 24*, 2 (2001), 205–229.

[4] Aghakhani, A., Yasa, O., Wrede, P., and Sitti, M. Acoustically powered surface-slipping mobile microrobots. *Proceedings of the National Academy of Sciences 117*, 7 (2020), 3469–3477.

[5] Al Khatib, E. *A Navigation and Control System for a Robot in Indoor/Outdoor Environments*. PhD thesis, 2016.

[6] Al Khatib, E., Bhattacharjee, A., Razzaghi, P., Rogowski, L. W., Kim, M. J., and Hurmuzlu, Y. Magnetically actuated simple millirobots for complex navigation and modular assembly. *IEEE Robotics and Automation Letters 5*, 2 (2020), 2958–2965.

[7] Al Khatib, E. I., Al-Masri, W. M., Mukhopadhyay, S., Jaradat, M. A., and Abdel-Hafez, M. A comparison of adaptive trajectory tracking controllers for wheeled mobile robots. In *2015 10th International Symposium on Mechatronics and its Applications (ISMA)* (2015), IEEE, pp. 1–6.

[8] Al Khatib, E. I., Jaradat, M. A., Abdel-Hafez, M., and Roigari, M. Multiple sensor fusion for mobile robot localization and navigation using the extended kalman filter. In *2015 10th international symposium on mechatronics and its applications (ISMA)* (2015), IEEE, pp. 1–5.

[9] Al Khatib, E. I., Jaradat, M. A. K., and Abdel-Hafez, M. F. Low-cost reduced navigation system for mobile robot in indoor/outdoor environments. *IEEE Access 8* (2020), 25014–25026.

[10] Alluhydan, K., Razzaghi, P., and Hurmuzlu, Y. On planar impacts of cylinders and balls. *Journal of Applied Mechanics 86*, 7 (2019).

[11] Ammi, M., and Ferreira, A. Realistic visual and haptic rendering for biological-cell injection. In *Proceedings of the 2005 IEEE International Conference on Robotics and Automation* (2005), IEEE, pp. 918–923.

[12] Armour, R., Paskins, K., Bowyer, A., Vincent, J., and Megill, W. Jumping robots: a biomimetic solution to locomotion across rough terrain. *Bioinspiration & biomimetics 2*, 3 (2007), S65.

[13] Asgari, M., Ghanbari, A., and Nahavandi, S. 3d particle-based cell modelling for haptic microrobotic cell injection. In *Proceedings of the 15th International Conference on Mechatronics Technology: Precision Mechatronics for Advanced Manufacturing, Service, and Medical Sectors* (2011), ICMT, pp. 1–6.

[14] Atherton, T. J., and Kerbyson, D. J. Size invariant circle detection. *Image and Vision computing 17*, 11 (1999), 795–803.

[15] Basdogan, C., Kiraz, A., Bukusoglu, I., Varol, A., and Doğanay, S. Haptic guidance for improved task performance in steering microparticles with optical tweezers. *Optics Express 15*, 18 (2007), 11616–11621.

[16] Bausch, A. R., Möller, W., and Sackmann, E. Measurement of local viscoelasticity and forces in living cells by magnetic tweezers. *Biophysical journal 76*, 1 (1999), 573–579.

[17] Bhatti, A., Khan, B., Nahavandi, S., Hanoun, S., and Gao, D. Intuitive haptics interface with accurate force estimation and reflection at nanoscale. In *Advances in Global Optimization*. Springer, 2015, pp. 507–514.

[18] Bi, C., Guix, M., Johnson, B., Jing, W., and Cappelleri, D. Design of microscale magnetic tumbling robots for locomotion in multiple environments and complex terrains. *Micromachines 9*, 2 (2018), 68.

[19] Bi, C., Niedert, E. E., Adam, G., Lambert, E., Solorio, L., Goergen, C. J., and Cappelleri, D. J. Tumbling magnetic microrobots for biomedical applications. In *2019 International Conference on Manipulation, Automation and Robotics at Small Scales (MARSS)* (2019), IEEE, pp. 1–6.

[20] Borzova, E., and Hurmuzlu, Y. Passively walking five-link robot. *Automatica 40*, 4 (2004), 621–629.

[21] Boukhnifer, M., and Ferreira, A. Fault tolerant control of a teleoperated piezoelectric microgripper. *Asian Journal of Control 15*, 3 (2013), 888–900.

[22] Bozuyuk, U., Yasa, O., Yasa, I. C., Ceylan, H., Kizilel, S., and Sitti, M. Light-triggered drug release from 3d-printed magnetic chitosan microswimmers. *ACS nano 12*, 9 (2018), 9617–9625.

[23] Brogliato, B. *"Nonsmooth Mechanics: Models, Dynamics and Control"*. Springer-Verlag, 1999.

[24] Burdick, J., and Fiorini, P. Minimalist jumping robots for celestial exploration. *The International Journal of Robotics Research 22*, 7-8 (2003), 653–674.

[25] Byun, D., Choi, J., Cha, K., Park, J.-o., and Park, S. Swimming microrobot actuated by two pairs of helmholtz coils system. *Mechatronics 21*, 1 (2011), 357–364.

[26] Caprari, G., Balmer, P., Piguet, R., and Siegwart, R. The autonomous micro robot" alice": a platform for scientific and commercial applications. In *Micromechatronics and Human Science, 1998. MHS'98. Proceedings of the 1998 International Symposium on* (1998), IEEE, pp. 231–235.

[27] Caprari, G., Estier, T., and Siegwart, R. Fascination of down scaling-alice the sugar cube robot. *Journal of micromechatronics 1*, 3 (2001), 177–189.

[28] Casarez, C., Penskiy, I., and Bergbreiter, S. Using an inertial tail for rapid turns on a miniature legged robot. In *Robotics and Automation (ICRA), 2013 IEEE International Conference on* (2013), IEEE, pp. 5469–5474.

[29] Chan, R. P. M., Stol, K. A., and Halkyard, C. R. Review of modelling and control of two-wheeled robots. *Annual reviews in control 37*, 1 (2013), 89–103.

[30] Chan, R. P. M., Stol, K. A., and Halkyard, C. R. Review of modelling and control of two-wheeled robots. *Annual reviews in control 37*, 1 (2013), 89–103.

[31] Chang, L., Howdyshell, M., Liao, W.-C., Chiang, C.-L., Gallego-Perez, D., Yang, Z., Lu, W., Byrd, J. C., Muthusamy, N., Lee, L. J., et al. Magnetic tweezers-based 3d microchannel electroporation for high-throughput gene transfection in living cells. *Small 11*, 15 (2015), 1818–1828.

[32] Cheang, U. K., Dejan, M., Choi, J., and Kim, M. Towards model-based control of achiral microswimmers. In *ASME 2014 Dynamic Systems and Control Conference* (2014), ASME, pp. V002T33A002–V002T33A002.

[33] Cheang, U. K., Kim, H., Milutinović, D., Choi, J., and Kim, M. J. Feedback control of an achiral robotic microswimmer. *Journal of Bionic Engineering 14*, 2 (2017), 245–259.

[34] Chen, L., Offenhäusser, A., and Krause, H.-J. Magnetic tweezers with high permeability electromagnets for fast actuation of magnetic beads. *Review of Scientific Instruments 86*, 4 (2015), 044701.

[35] Chen, X.-Z., Hoop, M., Mushtaq, F., Siringil, E., Hu, C., Nelson, B. J., and Pane, S. Recent developments in magnetically driven micro-and nanorobots. *Applied Materials Today 9* (2017), 37–48.

[36] Choi, H., Jeong, S., Lee, C., Park, B. J., Ko, S. Y., Park, J.-O., and Park, S. Three-dimensional swimming tadpole mini-robot using three-axis helmholtz coils. *International Journal of Control, Automation and Systems 12*, 3 (2014), 662–669.

[37] Chowdhury, S., Jing, W., and Cappelleri, D. Towards independent control of multiple magnetic mobile microrobots. *Micromachines 7*, 1 (2016), 3.

[38] Chung, S.-J., and Miller, D. W. Propellant-free control of tethered formation flight, part 1: Linear control and experimentation. *Journal of guidance, control, and dynamics 31*, 3 (2008), 571–584.

[39] Chung, S.-J., Slotine, J.-J. E., and Miller, D. W. Nonlinear model reduction and decentralized control of tethered formation flight. *Journal of Guidance, Control, and Dynamics 30*, 2 (2007), 390–400.

[40] Chung, S.-J., Slotine, J.-J. E., and Miller, D. W. Propellant-free control of tethered formation flight, part 2: Nonlinear underactuated control. *Journal of guidance, control, and dynamics 31*, 5 (2008), 1437–1446.

[41] Cui, R., Guo, J., and Mao, Z. Adaptive backstepping control of wheeled inverted pendulums models. *Nonlinear Dynamics 79*, 1 (2015), 501–511.

[42] de Oliveira Barros, A., and Yang, J. A review of magnetically actuated milli/micro-scale robots locomotion and features. *Critical Reviews™ in Biomedical Engineering 47*, 5 (2019).

[43] Dean, N. L. System for converting rotary motion into unidirectional motion, May 19 1959. US Patent 2,886,976.

[44] Degani, A., Choset, H., and Mason, M. T. Dsac-dynamic, single actuated climber: local stability and bifurcations. In *IEEE international conference on Robotics and automation (ICRA), 2010* (2010), IEEE, pp. 2803–2809.

[45] Diller, E., Giltinan, J., and Sitti, M. Independent control of multiple magnetic microrobots in three dimensions. *The International Journal of Robotics Research 32*, 5 (2013), 614–631.

[46] Diller, E., Pawashe, C., Floyd, S., and Sitti, M. Assembly and disassembly of magnetic mobile micro-robots towards deterministic 2-d reconfigurable micro-systems. *The International Journal of Robotics Research 30*, 14 (2011), 1667–1680.

[47] Diller, E., Zhuang, J., Zhan Lum, G., Edwards, M. R., and Sitti, M. Continuously distributed magnetization profile for millimeter-scale elastomeric undulatory swimming. *Applied Physics Letters 104*, 17 (2014), 174101.

[48] Dong, X., and Sitti, M. Planning spin-walking locomotion for automatic grasping of microobjects by an untethered magnetic microgripper. In *2017 IEEE International Conference on Robotics and Automation (ICRA)* (2017), pp. 6612–6618.

[49] Dong, X., and Sitti, M. Planning spin-walking locomotion for automatic grasping of microobjects by an untethered magnetic microgripper. In *2017 IEEE International Conference on Robotics and Automation (ICRA)* (2017), IEEE, pp. 6612–6618.

[50] Dong, X., and Sitti, M. Controlling two-dimensional collective formation and cooperative behavior of magnetic microrobot swarms. *The International Journal of Robotics Research* (2020), 0278364920903107.

[51] Ephanov, A., and Hurmuzlu, Y. Implementation of sensory feedback and trajectory tracking in active telemanipulation systems. *Journal of Dynamic Systems, Measurement, and Control 119* (1997), 447–454.

[52] Erkoc, P., Yasa, I. C., Ceylan, H., Yasa, O., Alapan, Y., and Sitti, M. Mobile microrobots for active therapeutic delivery. *Advanced Therapeutics 2*, 1 (2019), 1800064.

[53] Fukuoka, Y., Kimura, H., and Cohen, A. H. Adaptive dynamic walking of a quadruped robot on irregular terrain based on biological concepts. *The International Journal of Robotics Research 22*, 3-4 (2003), 187–202.

[54] Galla, M. E., Al Khatib, E. I., Hurmuzlu, Y., and Richer, E. Force and stiffness controller design for a pneumatic haptic glove for virtual palpation. In *ASME 2019 Dynamic Systems and Control Conference* (2019), American Society of Mechanical Engineers Digital Collection, pp. 1581–1586.

[55] Galla, M. E., Al Khatib, E. I., Hurmuzlu, Y., and Richer, E. Design and nonlinear control of a haptic glove for virtual palpation. In *Proceedings of the 2020 American Control Conference.* (2020), IEEE, pp. 1581–1586.

[56] Gao, W., Feng, X., Pei, A., Kane, C. R., Tam, R., Hennessy, C., and Wang, J. Bioinspired helical microswimmers based on vascular plants. *Nano Letters 14*, 1 (2014), 305–310.

[57] Gharib, M., Tavakoli, A., and Hurmuzlu, Y. Kinematics and dynamics of a sliding/bouncing two mass system. In *ASME 2011 International Design Engineering Technical Conferences and Computers and Information in Engineering Conference* (2011), ASME, pp. 237–246.

[58] Ginsberg, J. *Engineering dynamics*, vol. 10. Cambridge University Press, 2008.

[59] Grasser, F., D'arrigo, A., Colombi, S., and Rufer, A. C. Joe: a mobile, inverted pendulum. *IEEE Transactions on industrial electronics 49*, 1 (2002), 107–114.

[60] Guitron, S., Guha, A., Li, S., and Rus, D. Autonomous locomotion of a miniature, untethered origami robot using hall effect sensor-based magnetic localization. In *Robotics and Automation (ICRA), 2017 IEEE International Conference on* (2017), IEEE, pp. 4807–4813.

[61] Gutman, E., and Or, Y. Simple model of a planar undulating magnetic microswimmer. *Physical Review E 90*, 1 (2014), 013012.

[62] Haber, C., and Wirtz, D. Magnetic tweezers for dna micromanipulation. *Review of Scientific Instruments 71*, 12 (2000), 4561–4570.

[63] Hardarson, F. Locomotion for difficult terrain. *Dept. Mach. Des., Royal Inst. Technol., Stockholm, Sweden, Tech. Rep. TRITA-MMK 3* (1998), 1400–1179.

[64] Hayashi, R., and Tsujio, S. High-performance jumping movements by pendulum-type jumping machines. In *IEEE/RSJ International Conference on Intelligent Robots and Systems, 2001. Proceedings. 2001* (2001), vol. 2, IEEE, pp. 722–727.

[65] He, G.-P., Tan, X.-L., Zhang, X.-H., and Lu, Z. Modeling, motion planning, and control of one-legged hopping robot actuated by two arms. *Mechanism and Machine Theory 43*, 1 (2008), 33–49.

[66] Hirose, S., and Mori, M. Biologically inspired snake-like robots. In *Robotics and Biomimetics, 2004. ROBIO 2004. IEEE International Conference on* (2004), IEEE, pp. 1–7.

[67] Hollar, S., Flynn, A., Bellew, C., and Pister, K. Solar powered 10 mg silicon robot. In *The Sixteenth IEEE Annual International Conference on Micro Electro Mechanical Systems,Kyoto.* (2003), IEEE, pp. 706–711.

[68] Hong, Y.-D., and Kim, J.-H. 3-d command state-based modifiable walking of a humanoid robot on uneven terrain with different inclinations and heights. In *IEEE International Conference on Robotics and Biomimetics (ROBIO), 2011* (2011), IEEE, pp. 2223–2228.

[69] Hoover, A. M., Steltz, E., and Fearing, R. S. Roach: An autonomous 2.4 g crawling hexapod robot. In *2008 IEEE/RSJ International Conference on Intelligent Robots and Systems (IROS).* (2008), IEEE, pp. 26–33.

[70] Hou, M. T., Shen, H.-M., Jiang, G.-L., Lu, C.-N., Hsu, I.-J., and Yeh, J. A. A rolling locomotion method for untethered magnetic microrobots. *Applied Physics Letters 96*, 2 (2010), 024102.

[71] Hu, W., Lum, G. Z., Mastrangeli, M., and Sitti, M. Small-scale soft-bodied robot with multimodal locomotion. *Nature 554*, 7690 (2018), 81–85.

[72] Huang, J., Ri, S., Liu, L., Wang, Y., Kim, J., and Pak, G. Nonlinear disturbance observer-based dynamic surface control of mobile wheeled inverted pendulum. *IEEE Transactions on Control Systems Technology 23*, 6 (2015), 2400–2407.

[73] Hurmuzlu, Y., Ephanov, A., and Stoianovici, D. Effect of a pneumatically driven haptic interface on the perceptional capabilities of human operators. *Presence 7*, 3 (1998), 290–307.

[74] Hurmuzlu, Y., Genot, F., and Brogliato, B. Modeling, stability and control of biped robots—a general framework. *Automatica 40*, 10 (2004), 1647–1664.

[75] Hurmuzlu, Y., and Marghitu, D. B. Rigid body collisions of planar kinematic chains with multiple contact points. *The international journal of robotics research 13*, 1 (1994), 82–92.

[76] Hurmuzlu, Y., and Moskowitz, G. D. Bipedal locomotion stabilized by impact and switching: I. two-and three-dimensional, three-element models. *Dynamics and Stability of Systems 2*, 2 (1987), 73–96.

[77] Hurmuzlu, Y., and Moskowitz, G. D. Bipedal locomotion stabilized by impact and switching: Il. structural stability analysis of a four-element bipedal locomotion model. *Dyn. Stab. Syst 2*, 2 (1987), 97–112.

[78] Hurmuzulu, Y., and Marghitu, D. B. Coiiisions of planar kinematic chains with multiple contact points. *Advances in Robotics, Mechatronics and Haptic Interfaces 49* (1993), 271–280.

[79] Iida, F., Dravid, R., and Paul, C. Design and control of a pendulum driven hopping robot. In *IEEE/RSJ International Conference on Intelligent Robots and Systems, 2002.* (2002), vol. 3, IEEE, pp. 2141–2146.

[80] Ishiguro, Y., Takano, W., and Nakamura, Y. Bilateral remote teaching and autonomous task execution with task progress feedback. *Advanced Robotics 32*, 6 (2018), 311–324.

[81] J. Zoghzoghy, A. Alshorman, Y. H. Inertially actuated baton locomotor. In *ASME 2013 Dynamic Systems and Control Conference* (2013), American Society of Mechanical Engineers, p. DSCC2013SPA4012.

[82] Jammes, L., Kyodo, Y., Hiraki, M., and Ozono, S. Design concept and undulatory motion mode of a modular snake-like robot. In *Intelligent Robots and Systems, 1997. IROS'97., Proceedings of the 1997 IEEE/RSJ International Conference on* (1997), vol. 3, IEEE, pp. 1794–1800.

[83] Jang, B., Gutman, E., Stucki, N., Seitz, B. F., Wendel-García, P. D., Newton, T., Pokki, J., Ergeneman, O., Pané, S., Or, Y., et al. Undulatory locomotion of magnetic multilink nanoswimmers. *Nano letters 15*, 7 (2015), 4829–4833.

[84] Jiang, G.-L., Guu, Y.-H., Lu, C.-N., Li, P.-K., Shen, H.-M., Lee, L.-S., Yeh, J. A., and Hou, M. T.-K. Development of rolling magnetic microrobots. *Journal of Micromechanics and Microengineering 20*, 8 (2010), 085042.

[85] Jing, W., Pagano, N., and Cappelleri, D. J. A novel micro-scale magnetic tumbling microrobot. *Journal of Micro-Bio Robotics 8*, 1 (2013), 1–12.

[86] Kashki, M. *Dynamics and Control of Inertially Actuated Maneuvers and Locomotion of Robotic Systems*. PhD thesis, Southern Methodist University, 2016.

[87] Kashki, M., Ercan, S., and Hurmuzlu, Y. Pivot walking of an inertially actuated robot. *IEEE Transactions on Robotics 32*, 5 (2016), 1152–1162.

[88] Kashki, M., Ercan, S., and Hurmuzlu, Y. Pivot walking of an inertially actuated robot. *IEEE Transactions on Robotics 32*, 5 (2016), 1152–1162.

[89] Kashki, M., Zoghzoghy, J., and Hurmuzlu, Y. Adaptive control of inertially actuated bouncing robot. *IEEE/ASME Transactions on Mechatronics 22*, 5 (2017), 2196–2207.

[90] Kashki, M., Zoghzoghy, J., and Hurmuzlu, Y. Adaptive control of inertially actuated bouncing robot. *IEEE/ASME Transactions on Mechatronics 22*, 5 (2017), 2196–2207.

[91] Khalil, I. S., Pichel, M. P., Abelmann, L., and Misra, S. Closed-loop control of magnetotactic bacteria. *The International Journal of Robotics Research 32*, 6 (2013), 637–649.

[92] Kim, H., Ali, J., Cheang, U. K., Jeong, J., Kim, J. S., and Kim, M. J. Micro manipulation using magnetic microrobots. *Journal of Bionic Engineering 13*, 4 (2016), 515–524.

[93] Kim, S., Hashi, S., and Ishiyama, K. Magnetic actuation based snake-like mechanism and locomotion driven by rotating magnetic field. *IEEE Transactions on Magnetics 47*, 10 (2011), 3244–3247.

[94] Koh, J.-S., and Cho, K.-J. Omega-shaped inchworm-inspired crawling robot with large-index-and-pitch (lip) sma spring actuators. *IEEE/ASME Transactions On Mechatronics 18*, 2 (2013), 419–429.

[95] Kovac, M. Bioinspired jumping locomotion for miniature robotics. Tech. rep., Epfl, 2010.

[96] Kovac, M., Fuchs, M., Guignard, A., Zufferey, J.-C., and Floreano, D. A miniature 7g jumping robot. In *IEEE International Conference on Robotics and Automation ICRA 2008.* (2008), IEEE, pp. 373–378.

[97] Kuo, A. D., Donelan, J. M., and Ruina, A. Energetic consequences of walking like an inverted pendulum: step-to-step transitions. *Exercise and sport sciences reviews 33*, 2 (2005), 88–97.

[98] Lau, H., and Wai, L. Implementation of position–force and position–position teleoperator controllers with cable-driven mechanisms. *Robotics and Computer-Integrated Manufacturing 21*, 2 (2005), 145–152.

[99] Lee, J., Jin, M., and Ahn, K. K. Precise tracking control of shape memory alloy actuator systems using hyperbolic tangential sliding mode control with time delay estimation. *Mechatronics 23*, 3 (2013), 310–317.

[100] LEE, J. S., FEARING, R. S., and CHO, K.-J. Compound foot for increased millirobot jumping ability. In *Advances in Cooperative Robotics*. World Scientific, 2017, pp. 71–78.

[101] Lees, A., Vanrenterghem, J., and De Clercq, D. Understanding how an arm swing enhances performance in the vertical jump. *Journal of biomechanics 37*, 12 (2004), 1929–1940.

[102] levifoto. Stag beetle.

[103] Li, B., Deng, Q., and Liu, Z. A spherical hopping robot for exploration in complex environments. In *IEEE International Conference on Robotics and Biomimetics (ROBIO), 2009* (2009), IEEE, pp. 402–407.

[104] Libby, T., Johnson, A. M., Chang-Siu, E., Full, R. J., and Koditschek, D. E. Comparative design, scaling, and control of appendages for inertial reorientation. *IEEE Trans. Robotics 32*, 6 (2016), 1380–1398.

[105] Liljeback, P., Pettersen, K. Y., Stavdahl, O., and Gravdahl, J. T. Controllability and stability analysis of planar snake robot locomotion. *Automatic Control, IEEE Transactions on 56*, 6 (2011), 1365–1380.

[106] Liljebäck, P., Pettersen, K. Y., Stavdahl, Ø., and Gravdahl, J. T. A review on modelling, implementation, and control of snake robots. *Robotics and Autonomous Systems 60*, 1 (2012), 29–40.

[107] Ma, K. Y., Chirarattananon, P., Fuller, S. B., and Wood, R. J. Controlled flight of a biologically inspired, insect-scale robot. *Science 340*, 6132 (2013), 603–607.

[108] Mahoney, A. W., and Abbott, J. J. Managing magnetic force applied to a magnetic device by a rotating dipole field. *Applied Physics Letters 99*, 13 (2011), 134103.

[109] Mahoney, A. W., and Abbott, J. J. Control of untethered magnetically actuated tools with localization uncertainty using a rotating permanent magnet. In *Biomedical Robotics and Biomechatronics (BioRob), 2012 4th IEEE RAS & EMBS International Conference on* (2012), IEEE, pp. 1632–1637.

[110] Mahoney, A. W., and Abbott, J. J. 5-dof manipulation of an untethered magnetic device in fluid using a single permanent magnet. In *Robotics: Science and Systems* (2014), Citeseer.

[111] Mahoney, A. W., and Abbott, J. J. Generating rotating magnetic fields with a single permanent magnet for propulsion of untethered magnetic devices in a lumen. *IEEE Transactions on Robotics 30*, 2 (2014), 411–420.

[112] Mahoney, A. W., Cowan, D. L., Miller, K. M., and Abbott, J. J. Control of untethered magnetically actuated tools using a rotating permanent magnet in any position. In *2012 IEEE International Conference on Robotics and Automation (ICRA)* (2012), IEEE, pp. 3375–3380.

[113] Marhefka, D., Orin, D., Schmiedeler, J., and Waldron, K. Intelligent control of quadruped gallops. *Mechatronics, IEEE/ASME Transactions on 8*, 4 (2003), 446–456.

[114] Marhefka, D. W., Orin, D. E., Schmiedeler, J. P., and Waldron, K. J. Intelligent control of quadruped gallops. *IEEE/ASME Transactions On Mechatronics 8*, 4 (2003), 446–456.

[115] Matas, J., Galambos, C., and Kittler, J. Robust detection of lines using the progressive probabilistic hough transform. *Computer Vision and Image Understanding 78*, 1 (2000), 119–137.

[116] Meeker, D. C., Maslen, E. H., Ritter, R. C., and Creighton, F. M. Optimal realization of arbitrary forces in a magnetic stereotaxis system. *IEEE Transactions on Magnetics 32*, 2 (1996), 320–328.

[117] Mertz, L. Tiny conveyance: micro-and nanorobots prepare to advance medicine. *IEEE pulse 9*, 1 (2018), 19–23.

[118] Miyashita, S., Guitron, S., Ludersdorfer, M., Sung, C. R., and Rus, D. An untethered miniature origami robot that self-folds, walks, swims, and degrades. In *2015 IEEE International Conference on Robotics and Automation (ICRA)* (2015), IEEE, pp. 1490–1496.

[119] Miyashita, S., Guitron, S., Yoshida, K., Li, S., Damian, D. D., and Rus, D. Ingestible, controllable, and degradable origami robot for patching stomach wounds. In *2016 IEEE International Conference on Robotics and Automation (ICRA)* (2016), IEEE, pp. 909–916.

[120] Nam, J., Jeon, S., Kim, S., and Jang, G. Crawling microrobot actuated by a magnetic navigation system in tubular environments. *Sensors and Actuators A: Physical 209* (2014), 100–106.

[121] Nijmeijer, H., and Van der Schaft, A. *Nonlinear dynamical control systems*. Springer, 1990.

[122] Nijmeijer, H., and Van der Schaft, A. *Nonlinear dynamical control systems*. Springer, 1990.

[123] Nunez, V., Nadjar-Gauthier, N., Yokoi, K., Blazevic, P., and Stasse, O. Whole body posture controller based on inertial forces. In *Humanoid Robots, 2006 6th IEEE-RAS International Conference on* (2006), IEEE, pp. 188–193.

[124] Okubo, O., Nakano, E., and Handa, M. Design of a jumping machine using self-energizing spring. In *Proceedings of the 1996 IEEE/RSJ International Conference on Intelligent Robots and Systems' 96, IROS 96,* (1996), vol. 1, IEEE, pp. 186–191.

[125] Ousaid, A. M., Bolopion, A., Haliyo, S., Régnier, S., and Hayward, V. Stability and transparency analysis of a teleoperation chain for microscale interaction. In *2014 IEEE International Conference on Robotics and Automation (ICRA)* (2014), IEEE, pp. 5946–5951.

[126] Pacchierotti, C., Magdanz, V., Medina-Sánchez, M., Schmidt, O. G., Prattichizzo, D., and Misra, S. Intuitive control of self-propelled microjets with haptic feedback. *Journal of micro-bio robotics 10*, 1-4 (2015), 37–53.

[127] Pacchierotti, C., Scheggi, S., Prattichizzo, D., and Misra, S. Haptic feedback for microrobotics applications: A review. *Frontiers in Robotics and AI 3* (2016), 53.

[128] Palagi, S., and Fischer, P. Bioinspired microrobots. *Nature Reviews Materials 3*, 6 (2018), 113.

[129] Pathak, K., Franch, J., and Agrawal, S. K. Velocity and position control of a wheeled inverted pendulum by partial feedback linearization. *IEEE Transactions on robotics 21*, 3 (2005), 505–513.

[130] Paul, C., Dravid, R., and Iida, F. Control of lateral bounding for a pendulum driven hopping robot. In *Proc. of 5th International Conference on Climbing and Waffling Robots (CLAWAR 2002)* (2002), pp. 333–340.

[131] Pawashe, C., Floyd, S., and Sitti, M. Modeling and experimental characterization of an untethered magnetic micro-robot. *The International Journal of Robotics Research 28*, 8 (2009), 1077–1094.

[132] Pepe, A., Chiaravalli, D., and Melchiorri, C. A hybrid teleoperation control scheme for a single-arm mobile manipulator with omnidirectional wheels. In *IEEE/RSJ International Conference on Intelligent Robots and Systems (IROS)* (Oct 2016), pp. 1450–1455.

[133] Petruska, A. J., and Abbott, J. J. Omnimagnet: An omnidirectional electromagnet for controlled dipole-field generation. *IEEE Transactions on Magnetics 50*, 7 (2014), 8400810.

[134] Pierre, R. S., and Bergbreiter, S. Gait exploration of sub-2 g robots using magnetic actuation. *IEEE Robotics and Automation Letters 2*, 1 (2017), 34–40.

[135] Popek, K. M., Schmid, T., and Abbott, J. J. Six-degree-of-freedom localization of an untethered magnetic capsule using a single rotating magnetic dipole. *IEEE Robotics and Automation Letters 2*, 1 (2017), 305–312.

[136] Purcell, E. M. Life at low reynolds number. *American journal of physics 45*, 1 (1977), 3–11.

[137] Quirini, M., Webster, R. J., Menciassi, A., and Dario, P. Design of a pill-sized 12-legged endoscopic capsule robot. In *2007 IEEE International Conference on Robotics and Automation (ICRA)* (2007), IEEE, pp. 1856–1862.

[138] Raibert, M., Blankespoor, K., Nelson, G., Playter, R., et al. Bigdog, the rough-terrain quadruped robot. In *Proceedings of the 17th World Congress* (2008), pp. 10823–10825.

[139] Razzaghi, P., Al Khatib, E., Alluhydan, K., and Hurmuzlu, Y. $h_2 - h_\infty$ model reference adaptive control of tethered satellite system. In *2020 IEEE Aerospace Conference* (2020), IEEE.

[140] Razzaghi, P., Al Khatib, E., and Hurmuzlu, Y. Nonlinear dynamics and control of an inertially actuated jumper robot. *Nonlinear Dynamics 97*, 1 (2019), 161–176.

[141] Razzaghi, P., Alluhydan, K., and Hurmuzlu, Y. Planar impacts in hybrid chains of cylinders and balls. *Journal of Applied Mechanics 86*, 12 (2019).

[142] Razzaghi, P., and Assadian, N. Study of the triple-mass tethered satellite system under aerodynamic drag and j2 perturbations. *Advances in Space Research 56*, 10 (2015), 2141–2150.

[143] Saito, M., Fukaya, M., and Iwasaki, T. Modeling, analysis, and synthesis of serpentine locomotion with a multilink robotic snake. *IEEE Control Systems Magazine 22*, 1 (2002), 64–81.

[144] Scarfogliero, U., Stefanini, C., and Dario, P. Design and development of the long-jumping" grillo" mini robot. In *Robotics and Automation, 2007 IEEE International Conference on* (2007), IEEE, pp. 467–472.

[145] Schmid, A., Yechangunja, R., Thalhammer, S., and Srinivasan, M. A. Human-operated 3d micro-manipulator with haptic feedback. In *2012 IEEE Haptics Symposium (HAPTICS)* (2012), IEEE, pp. 517–522.

[146] Shahrokhi, S., and Becker, A. T. Object manipulation and position control using a swarm with global inputs. In *2016 IEEE International Conference on Automation Science and Engineering (CASE)* (2016), IEEE, pp. 561–566.

[147] Shahrokhi, S., Shi, J., Isichei, B., and Becker, A. T. Exploiting nonslip wall contacts to position two particles using the same control input. *IEEE Transactions on Robotics 35*, 3 (2019), 577–588.

[148] Shahsavan, H., Aghakhani, A., Zeng, H., Guo, Y., Davidson, Z. S., Priimagi, A., and Sitti, M. Bioinspired underwater locomotion of light-driven liquid crystal gels. *Proceedings of the National Academy of Sciences 117*, 10 (2020), 5125–5133.

[149] Shan, Y., and Koren, Y. Design and motion planning of a mechanical snake. *Systems, Man and Cybernetics, IEEE Transactions on 23*, 4 (1993), 1091–1100.

[150] Simi, M., Valdastri, P., Quaglia, C., Menciassi, A., and Dario, P. Design, fabrication, and testing of a capsule with hybrid locomotion for gastrointestinal tract exploration. *Mechatronics, IEEE/ASME Transactions on 15*, 2 (2010), 170–180.

[151] Sitti, M., Ceylan, H., Hu, W., Giltinan, J., Turan, M., Yim, S., and Diller, E. Biomedical applications of untethered mobile milli/microrobots. *Proceedings of the IEEE 103*, 2 (2015), 205–224.

[152] Son, D., Yim, S., and Sitti, M. A 5-d localization method for a magnetically manipulated untethered robot using a 2-d array of hall-effect sensors. *IEEE/ASME Transactions on Mechatronics 21*, 2 (2016), 708–716.

[153] Song, G., Yin, K., Zhou, Y., and Cheng, X. A surveillance robot with hopping capabilities for home security. *Consumer Electronics, IEEE Transactions on 55*, 4 (2009), 2034–2039.

[154] Spanos, P., Berka, R. B., and Tratskas, P. Multisegment large space robot: Concept and design. *Journal of Aerospace Engineering 13*, 4 (2000), 123–132.

[155] Sridhar, V., Park, B.-W., and Sitti, M. Light-driven janus hollow mesoporous tio2–au microswimmers. *Advanced Functional Materials 28*, 25 (2018), 1704902.

[156] Stoianovici, D. Achieving a massless haptic interface. *Proc. ASME Dynamic Systems and Control Division, 1997* (1997).

[157] Støy, K., Shen, W.-M., and Will, P. M. Using role-based control to produce locomotion in chain-type self-reconfigurable robots. *Mechatronics, IEEE/ASME Transactions on 7*, 4 (2002), 410–417.

[158] Tan, H. Z., Walker, L., Reifenberger, R., Mahadoo, S., Chiu, G., Raman, A., Helser, A., and Colilla, P. A haptic interface for human-in-the-loop manipulation at the nanoscale. In *First Joint Eurohaptics Conference and Symposium on Haptic Interfaces for Virtual Environment and Teleoperator Systems. World Haptics Conference* (2005), IEEE, pp. 271–276.

[159] Tavakoli, A., Gharib, M., and Hurmuzlu, Y. Collision of two mass baton with massive external surfaces. *Journal of Applied Mechanics 79*, 5 (2012), 051019.

[160] Tavakoli, A., and Hurmuzlu, Y. Gravity powered locomotion and active control of two simple systems. In *ASME 2009 Dynamic Systems and Control Conference* (2009), American Society of Mechanical Engineers, pp. 379–386.

[161] Tavakoli, A., and Hurmuzlu, Y. Robotic locomotion of three generations of a family tree of dynamical systems. part i: Passive gait patterns. *Nonlinear Dynamics 73*, 3 (2013), 1969–1989.

[162] Tavakoli, A., and Hurmuzlu, Y. Robotic locomotion of three generations of a family tree of dynamical systems. part i: Passive gait patterns. *Nonlinear Dynamics 73*, 3 (2013), 1969–1989.

[163] Tavakoli, A., and Hurmuzlu, Y. Robotic locomotion of three generations of a family tree of dynamical systems. part ii: Impulsive control of gait patterns. *Nonlinear Dynamics 73*, 3 (2013), 1991–2012.

[164] Tayefi, M., and Geng, Z. Self-balancing controlled lagrangian and geometric control of unmanned mobile robots. *Journal of Intelligent & Robotic Systems 90*, 1-2 (2018), 253–265.

[165] Tung, H.-W., Peyer, K. E., Sargent, D. F., and Nelson, B. J. Noncontact manipulation using a transversely magnetized rolling robot. *Applied Physics Letters 103*, 11 (2013), 114101.

[166] Vogtmann, D., Pierre, R. S., and Bergbreiter, S. A 25 mg magnetically actuated microrobot walking at¿ 5 body lengths/sec. In *2017 IEEE 30th International Conference on Micro Electro Mechanical Systems (MEMS)* (2017), IEEE, pp. 179–182.

[167] Wang, H., Luan, Y., Oetomo, D., and Wang, Z. Design, analysis and experimental evaluation of a gas-fuel-powered actuator for robotic hoppers. *Mechatronics, IEEE/ASME Transactions on 20*, 5 (2015), 2264–2275.

[168] Weiss, P. Hop... hop... hopbots!: designers of small, mobile robots take cues from grasshoppers and frogs. *Science News 159*, 6 (2001), 88–91.

[169] Westervelt, E. R., Grizzle, J. W., Chevallereau, C., Choi, J. H., and Morris, B. *Feedback control of dynamic bipedal robot locomotion*, vol. 28. CRC press, 2007.

[170] Worst, R., and Linnemann, R. Construction and operation of a snake-like robot. In *Intelligence and Systems, 1996., IEEE International Joint Symposia on* (1996), IEEE, pp. 164–169.

[171] Xu, T., Yu, J., Yan, X., Choi, H., and Zhang, L. Magnetic actuation based motion control for microrobots: An overview. *Micromachines 6*, 9 (2015), 1346–1364.

[172] Yang, K., Lu, C., Zhao, X., and Kawamura, R. From bead to rod: Comparison of theories by measuring translational drag coefficients of micron-sized magnetic bead-chains in stokes flow. *PloS One 12*, 11 (2017), e0188015.

[173] Yesin, K. B., Vollmers, K., and Nelson, B. J. Modeling and control of untethered biomicrorobots in a fluidic environment using electromagnetic fields. *The International Journal of Robotics Research 25*, 5-6 (2006), 527–536.

[174] Yilmaz, C., Gharib, M., and Hurmuzlu, Y. Solving frictionless rocking block problem with multiple impacts. In *Proceedings of the Royal Society of London A: Mathematical, Physical and Engineering Sciences* (2009), The Royal Society, p. rspa20090273.

[175] Yu, J., Yang, L., and Zhang, L. Pattern generation and motion control of a vortex-like paramagnetic nanoparticle swarm. *The International Journal of Robotics Research 37*, 8 (2018), 912–930.

[176] Zhang, J., and Diller, E. Untethered miniature soft robots: Modeling and design of a millimeter-scale swimming magnetic sheet. *Soft robotics 5*, 6 (2018), 761–776.

[177] Zhang, X., Kim, H., and Kim, M. J. Design, implementation, and analysis of a 3-d magnetic tweezer system with high magnetic field gradient. *IEEE Transactions on Instrumentation and Measurement 68*, 3 (March 2019), 680–687.

[178] Zhang, X., Kim, H., Rogowski, L. W., Sheckman, S., and Kim, M. J. Novel 3d magnetic tweezer system for microswimmer manipulations. In *2017 14th International Conference on Ubiquitous Robots and Ambient Intelligence (URAI)* (2017), IEEE, pp. 382–387.

[179] Zhang, X., Rogowski, L. W., and Kim, M. J. 3d micromanipulation of particle swarm using a hexapole magnetic tweezer. In *IEEE/RSJ International Conference on Intelligent Robots and Systems (IROS)* (2019), IEEE, pp. 1581–1586.

[180] Zhang, X., Rogowski, L. W., and Kim, M. J. Closed-loop control using high power hexapole magnetic tweezers for 3d micromanipulation. *Journal of Bionic Engineering 17*, 1 (2020), 113–122.

[181] Zhang, Z., Huang, K., and Menq, C.-H. Design, implementation, and force modeling of quadrupole magnetic tweezers. *IEEE/ASME Transactions on Mechatronics 15*, 5 (2009), 704–713.

[182] Zhao, J., Xu, J., Gao, B., Xi, N., Cintron, F. J., Mutka, M. W., and Xiao, L. Msu jumper: A single-motor-actuated miniature steerable jumping robot. *Robotics, IEEE Transactions on 29*, 3 (2013), 602–614.

[183] Zhao, J., Zhao, T., Xi, N., Mutka, M. W., and Xiao, L. Msu tailbot: Controlling aerial maneuver of a miniature-tailed jumping robot. *Mechatronics, IEEE/ASME Transactions on 20*, 6 (2015), 2903–2914.

[184] Zoghzoghy, J., and Hurmuzlu, Y. Dynamics, stability, and experimental results for a baton robot with double-action inertial actuation. *International Journal of Dynamics and Control* (2017), 1–19.

[185] Zoghzoghy, J., Zhao, J., and Hurmuzlu, Y. Modeling, design, and implementation of a baton robot with double-action inertial actuation. *Mechatronics 29* (2015), 1–12.

[186] Zoghzoghy, J., Zhao, J., and Hurmuzlu, Y. Modeling, design, and implementation of a baton robot with double-action inertial actuation. *Mechatronics 29* (2015), 1–12.